

Detector Control System for CMS Endcap RPCs
and
Cross Section Measurement of $t\bar{t}$ dileptonic channel with
the CMS Detector at $\sqrt{s} = 8 \text{ TeV}$



by
Taimoor Khurshid

SUBMITTED IN PARTIAL FULFILLMENT OF THE
REQUIREMENTS FOR THE DEGREE OF
DOCTOR OF PHILOSOPHY
AT
QUAID-I-AZAM UNIVERSITY
ISLAMABAD, PAKISTAN
JAN 2015

CERN-THESIS-2015-335
15/09/2015



CERTIFICATE

The undersigned hereby certify that the research work presented in this thesis titled “**Detector Control System for CMS Endcap RPCs and Cross Section Measurement of $t\bar{t}$ dileptonic channel with the CMS Detector at $\sqrt{s} = 8$ TeV**” by **Taimoor Khurshid** is carried out under my supervision in partial fulfillment of the requirements for the degree of **Doctor of Philosophy**.

Supervisor:

Prof. Hafeez R. Hoorani
Director General
National Center For Physics
Quaid-i-Azam University Campus
Islamabad, Pakistan

Submitted Through:

Prof. Arshad Majeed Mirza
Chairman
Department of Physics
Quaid-i-Azam University
Islamabad, Pakistan

Dedicated to my Ammi, Abbu and Wife

Abstract

The Resistive Plate Chamber Endcap(RE) system consists of 432 double-gap chambers equipped with about 1296 front-end boards. Safe and correct operation of RE system requires a sophisticated and complex online Detector Control System(DCS), which should be able to control and monitor 2×10^3 hardware devices spanned on an area of about 2000 m^2 . DCS of RE system monitors, acquires and stores about 10^3 parameters obtained from the detector, electronics, power system, gas, and cooling systems. The RE DCS system and its performance during the 2007 and 2008 CMS cosmic runs, will be discussed in this thesis.

The $t\bar{t}$ pair production cross section is measured in 2012 proton-proton collisions at $\sqrt{s} = 8 \text{ TeV}$ using 19.7 fb^{-1} of integrated luminosity data sample of the CMS experiment. The measurement is done by using events in which we have two high p_T leptons (muons or electrons), missing transverse energy and atleast one jet identified as b -quark, in the final state. The cross section was value

$$\sigma_{t\bar{t}} = 248.530 \pm 1.028(\text{stat.}) \pm 8.202(\text{syst.})\text{pb}$$

is in agreement with theoretical predictions, also individual cross section for each dilepton channel are provided.

Acknowledgement

First and the foremost, I want to express my deepest gratitude to my venerable teacher and supervisor, Professor Hafeez R. Hoorani, for his worthy kindness and invaluable favours. He guided my work with infinite patience, enthusiasm and a great amount of tolerance. With all my ventures, I always could rely on his remarkable ability to quickly distill any problem to its essence.

My gratitude also goes to Giovanni Polese who along with Hassan Shahzad provided the early direction that I needed to begin the long process of development of RPC End-cap Detector Control System.

I would like to thank many people from the Top cross-section group have helped me along the way. Particularly, I would like to thank Andreas Meyer and Mara Senghi Soares, who gave me guidance and suggestions for the improvement of cross-section analysis and also Drell-Yan background studies. I am also thankful to Akram Khan, Carmen Diez, Sadia Khalil and Mohsen Naseri, who gave me suggestions and input that was very important to get a clear understanding of the Top cross-section analysis. It was a great experience working with all the members of the Top cross-section analysis at CMS.

I am thankful to Chairman, Department of Physics, Quaid-i-Azam University for allowing me to do research in National Center for Physics (NCP).

Mind is like a parachute. It works only when open and my teachers taught me how to open it. I extend my gratitude to all my teachers in the Physics department, specially I would like to express my immense gratitude to Dr. Khalid Khan and Dr. Shafiq for their nice and jolly company. My most profound thanks go to my colleagues Adeel Bhai and Fawad bhai, for their help which they impart to me during various stages of my research work.

I am immensely grateful to my worthy group-mates at NCP, for many fruitful discussions and ready cooperation. I highly value the helping attitude of Irfan Asghar, Muhammad Ahmad, Wajid Ali Khan, Jamila Bashir Butt, M Jamil Aslam, Asif Siddique and Ishtiaq Ahmed who always encouraged me when the load was heavy. My cordial thanks to my friends Asghar, Rizwan, Shehzad, Kamran, Atif, sajjad, Naveed,

and Salman. Their warm companionship make the life at campus beautiful and unforgettable.

I can never thank enough my parents for everything they have done for me. Even then, I wish to record my deepest obligations to my father who always loves me and my mother for her endless contribution to make me stay on the track. No one tolerates me more than they do. I am forever indebted to the love and caring of my brothers and sisters. Thanks are due to my wife for being such a terrific person through the years. She never failed to show concern when things got stressful. A great thanks to my family for their unconditional support, belief in me and for keeping me grounded.

Taimoor Khurshid

Table of Contents

Abstract	iv
Acknowledgement	v
Table of Contents	vii
List of Tables	x
List of Figures	xii
1 Introduction	1
2 Experimental Setup	3
2.1 The Large Hadron Collider	3
2.1.1 The experiments at the LHC	4
2.1.2 The LHC run periods	5
2.2 Compact Muon Solenoid	7
2.2.1 Tracking System	8
2.2.2 Calorimeter System	10
2.2.3 Magnet System	11
2.2.4 Muon System	11
2.2.5 Trigger System	11
2.2.6 CMS Data taking during the 2011 and 2012 LHC runs	12
3 The Endcap RPC Detector Control System	14
3.1 Resistive Plate Chambers	14
3.1.1 Layout and Geometry of End-Cap RPCs	17
3.1.2 Modes of Operation	18
3.1.3 RPC Performance Parameters	19
3.2 RPC Endcap Control System	20
3.2.1 Software Framework	21
3.2.2 The Power Supply for RE System	25
3.2.3 The Environmental Control System	32
3.2.4 External Control System	35
3.2.5 Supervisor	36
3.3 CMS data taking and Role of Endcap DCS	45
3.3.1 Performance of RE DCS	47
3.4 Conclusion	51

4	The Top Quark : The"King" of Fermions	54
4.1	Top Quark in the Standard Model	54
4.2	Top Quark Production	55
4.2.1	Top Quark Production via the Strong Interaction	56
4.2.2	Top Quark Production via Weak Interaction	57
4.3	Top Quark Decay	58
4.4	Signature of $t\bar{t}$ in dilepton channel	60
4.5	Background Processes for $t\bar{t}$ Dileptonic Channel	60
4.5.1	Drell Yan: $Z/\gamma^* \rightarrow l^+l^-$	61
4.5.2	Dibosons: WW, WZ, ZZ	61
4.5.3	Single Top	62
4.5.4	$W + \text{jets}$	62
5	Event Reconstruction	64
5.1	Particle flow	64
5.2	Muons	65
5.2.1	Signal Muon Selection	66
5.3	Electrons	67
5.3.1	Signal Electron Selection	68
5.4	Jets	68
5.4.1	The anti- k_T algorithm	69
5.4.2	Jet Calibration	69
5.4.3	Jet Selection	70
5.5	b -Jet Identification	71
5.6	Neutrinos	73
5.7	Pile-up removal	74
5.7.1	Top projections	74
5.8	Corrections Applied to the Simulated Events	76
5.8.1	Pile-up Reweighting	76
5.8.2	Lepton Isolation, Identification and Trigger Reweighting	77
5.8.3	B -tag Efficiency Reweighting	77
6	Data Samples and Event Selection	81
6.1	Collision Data Sample	81
6.2	Monte Carlo Signal and Background Modeling	82
6.3	Event cleaning	84
6.3.1	Beam Scraping	84
6.3.2	Primary Vertex	84
6.3.3	HCAL Noise	84
6.4	Trigger	85
6.5	Event Selection	86
6.5.1	Signal Signatures and Backgrounds	86
6.5.2	Dilepton Selection	87
6.5.3	Data MonteCarlo Comparison	89
6.5.4	Event Yield and Selection Summary	95

7	Background Determination and Systematic Uncertainties	97
7.1	Drell-Yan	97
7.1.1	Scale factors at different selection steps	98
7.2	Systematic uncertainties	100
7.2.1	Luminosity	100
7.2.2	Pile-up	100
7.2.3	Trigger	100
7.2.4	Lepton	101
7.2.5	Jet Energy Resolution	101
7.2.6	Backgrounds	101
7.2.7	Top Quark Mass	101
7.2.8	Hard Scattering Q^2 Scale	102
7.2.9	Matching Scale	102
7.2.10	ISR and FSR	102
7.2.11	Summary	102
8	Cross-section	103
8.1	Combination of results	105
8.2	Conclusion	105
	Bibliography	106

List of Tables

2.1	Some important parameters of LHC comparing achieved values from 2012 with design values. Values taken from [10].	5
3.1	Dimensions of RPC installed in Ring2 and Ring3.	18
3.2	Hardware used in High Voltage System	27
3.3	Hardware used in Low Voltage System.	28
3.4	Required parameters for Endcap RPC's High Voltage and Low Voltage System.	30
3.5	Details of environmental sensors and their physical distributions.	33
3.6	Endcap RPC's environmental network requirements.	33
3.7	Deadbands used to store the values in the online database for the most important parameters.	43
4.1	Leptons and quarks - the building blocks of the matter (according to the Standard Model). Weak isopin (I_3), hypercharge (Y) and electric charge assignments are respectively shown in the fourth, fifth and sixth columns. The last column lists the masses of the fermions according to [37].	55
4.2	Most precise measurements of the $t\bar{t}$ pair production cross section at the Tevatron [42] and at the LHC [43, 44] compared with the NNLO+NNLL theoretical calculations [40, 41]. The measurement assume a top quark mass of 172.5 GeV	57
4.3	At born level, branching ratios for all decay modes of the W^+ Boson. The BR values for the decays modes of the W^- are the same [49].	58
4.4	$t\bar{t}$ Decay Channels and their BRs.	59
5.1	Overview of the muon identification criteria used in the 8 TeV datasets[61].	67
5.2	Overview of the electron identification criteria used in the 8 TeV datasets [66].	69
5.3	Jet selection criteria[76].	71
5.4	The lepton identification and isolation efficiency scale factors taken from [87].	77
5.5	Scale factors for CSVL tagger.	78
6.1	All data samples used in the analysis.	82
6.2	All data samples used in the analysis.	83
6.3	Summary of all cuts applied.	95

6.4	Event selection yields in the different channels after each selection cut. The expected number of events in simulation corresponds to the luminosity of the data, and correction factors have been applied.	96
7.1	Data-driven Drell-Yan background estimation in the $\mu\mu$ and ee channels after the missing transverse energy cut.	98
7.2	Drell-Yan scale factors after different selection steps, both for ee and $\mu\mu$ channels.	99
7.3	Summary of the systematic uncertainties for the measurement of the inclusive $t\bar{t}$ cross section. The contribution from non- Z +jets backgrounds is referred to as background (other).	102
8.1	Expected signal and background contributions compared to the number of events observed in data passing full signal selection with at least one b-tagged jet required.	104
8.2	Summary of $t\bar{t}$ signal production cross section measured in separate event selection channels. The number of events observed in data, the total background expectations, the total signal acceptance (includes geometric detector acceptance and event selection efficiency) with systematic uncertainties, and the cross section measurements are shown separately. The uncertainties on the cross section include statistical only.	104

List of Figures

2.1	Schematic diagram of CERN accelerator [9].	4
2.2	Schematic view of the LHC accelerator and location of it's experiments. . .	6
2.3	Integrated luminosity and peak luminosity as a function of time during 2011 operation of the LHC at $\sqrt{s} = 7 TeV$ [17].	6
2.4	Integrated luminosity and peak luminosity as a function of time during 2011 operation of the LHC at $\sqrt{s} = 8 TeV$ [17].	7
2.5	Integrated luminosity and peak luminosity as a function of time during 2011 operation of the LHC at $\sqrt{s} = 8 TeV$ [17].	8
2.6	Overview of the CMS detector [11].	9
2.7	The r-z view of quarter part of CMS tracker. The modules indicated by open (blue) lines are stereo modules. Figure taken from [19] and modified.	9
2.8	The r-z view of quarter part of CMS muon system [7].	12
2.9	Integrated luminosity as a function of time during the 2011 and 2012 proton-proton running of the LHC at $\sqrt{s} = 7$ and $8 TeV$ [20]. The luminosity delivered by LHC is compared to the luminosity recorded by CMS. The validated luminosity depicts the data that is certified for physics analysis.	13
3.1	View of a quadrant of CMS in rz-plane where MB and ME are the Barrel and EndCap Muon system layout.	15
3.2	RPC Detector Endcap schematic layout, left figure shows RE2 RPC disc's r- ϕ layout, which is at the back side of the first endcap yoke, while right figure shows layout of the entire CMS endcap muon system[22].	16
3.3	A complete EndCap RPC Disk of CMS. The RPCs are installed in Ring2 and Ring3 where Ring1 is empty.	16
3.4	Geometry of a Resistive Plate Chamber where, R_0 and R_i are radii from beam line at low and high eta respectively.	17
3.5	Geometry of a Resistive Plate Chamber	18
3.6	The RE DCS software schema. All sub components are summarised and can be controlled from a single module, the Supervisor. Finally the Supervisor will uplink to the so called Central DCS, where all sub detector controls and status summaries are united.	21
3.7	CTRL script editor.	22
3.8	PARA database editor - datapoint type " <i>ExampleDP_Float</i> " with datapoint " <i>ExampleDP_Arg1</i> ".	23

3.9	The manager communication structure of a typical PVSS project.	24
3.10	JCOP Framework component installer. This component manages the installation, reinstallation and deletion of components. It is provided with a DB connection to automate the installation according to a template of the current machine.	25
3.11	Device Editor Navigator(left), Real Hardware View(right)	26
3.12	HV distribution box	27
3.13	Schematic overview of the CAEN EASY Power Supply System.	29
3.14	The CAEN mainframe communicates with the DCS via OPC and allows us to operate each power channel independently. The detector control system monitors the status of the and sends appropriate commands to the Mainframe.	31
3.15	In the endcap region, all the stations (green) are equipped with temperature sensors.	32
3.16	GUI for the monitoring of the environmental sensors located at detector region.	34
3.17	FEB temperature data flow block diagram. XDAQ application fetch information the LBs which is then sent to the PVSS application via PSX.	34
3.18	CMS cooling system. Cooling of RPC chambers is done by different lines, in order to avoid heat exchange from the other subsystems, in this way the chamber electronics temperature is kept stable.	35
3.19	The Supervisor Panel	38
3.20	The CMS Endcap RPC detector control system layout	39
3.21	RECS hierarchy tree can be seen. As shown commands propagate downwards in the hierarchy, while error messages and other informations are propagated upwards.	40
3.22	For HV channels, device state model is shown.	41
3.23	Typical layout of the Supervisor system. Left image shows Endcap's main Supervisor panel. All the objects are coloured according the status of the chamber. Right image shows an Endcap Disk panel. By clicking on each chamber, it is possible to obtain more information about the status of services and their behaviour over time.	42
3.24	The DBS setup provided for the whole CMS experiment.	43
3.25	Communication structure of the DCS authentication framework.	44
3.26	PVSS Alarm handling panel. Here one defines different thresholds and the alarm message.	45
3.27	Event display of a nice beam halo event from CMS(26-Nov-2009).	46
3.28	Plot shows the effect on time spent, to set different parameters, due to the increment in the number of CAEN channels. This configuration shows the maximum loads that can be configured per SY1527 in our configuration.	48
3.29	Global Monitoring panel, showing chamber currents(left plot) and temperatures(right plot).	49
3.30	current vs time history plots for 18 chambers.	50

3.31	FEB temperature depends upon coolant temperature results from some installed chambers. In the region I water temperature is at $20^{\circ}C$ which is stable working condition. In region II water temperature was decreased to $19^{\circ}C$. In region III no cooling.	51
3.32	Disc temperature and humidity panel	52
4.1	The $t\bar{t}$ pair production mechanisms.	56
4.2	Feynman diagrams of single top quark production: (a) t-channel, (b) associated production (c) s-channel. By interchanging anti-quarks and quarks, the diagrams for single anti-top quark production can be obtained.	57
4.3	Decay channels of $t\bar{t}$ pairs and their corresponding BR, according to theoretical predictions at tree level.	59
4.4	Example of Feynman diagram of $t\bar{t}$ decay in the dilepton channel at tree level.	60
4.5	Example of a Feynman diagram for the Z +jets process	61
4.6	Example of a Feynman diagram for the WW process	62
4.7	Example of a Feynman diagram of single top tW-channel production	62
4.8	Example of a Feynman diagram for the W+jets and multijets production	63
5.1	Illustration of the particle-flow concept to reconstruct every individual muon, electron, photon, charged and neutral hadron from a maximum of detector information[55].	66
5.2	Illustration of the factorized approach of Jet Energy Calibration in CMS.	70
5.3	Impact parameter between primary vertex and track.	72
5.4	Efficiency of b-jet tagging CSV algorithm. the lower panel shows scale factors SF_b [80].	72
5.5	Event display of an event with 29 vertices [84].	74
5.6	Reconstruction of particles in an event. From all seven reconstructed particles (top) the two leptons on the right are projected out as isolated leptons. The remaining five particles (left) then form a jet[83].	75
5.7	The distribution of the number of vertices in the $e\mu$ channel. Left without pile-up reweighting, right with pile-up reweighting.	76
5.8	Global SF as a function of (η, p_T) of the lepton, for muons (left) and electrons (right)	77
5.9	b-tagging efficiency of individual b -jets (left) and mistag rate for c -jets (middle) and l -jets (right) as function of jet p_T and η for e^+e^- (top), $\mu^{\pm}e^{\mp}$ (center) and $\mu^+\mu^-$ (bottom) channels, determined from the simulation.	79
6.1	Distribution of the number of primary vertices in the $\mu^+\mu^-$, e^+e^- and $e^{\pm}\mu^{\mp}$ channels before and after pile-up reweighting. The plot is created after the selection of one isolated muon and one isolated electron with only an invariant mass requirement of $20 GeV$	90

6.2	Transverse momentum p_T distributions of isolated leading lepton (left figures) and second leading (right figures) candidates for the $\mu^+\mu^-$, e^+e^- and $e^\pm\mu^\mp$ samples. For the $\mu^+\mu^-$ and e^+e^- channels, the events with $76 < m_{ll} < 106 \text{ GeV}$ and $\cancel{E}_T < 40 \text{ GeV}$ are rejected. The simulated samples are normalised to an integrated luminosity of 19.7 fb^{-1} . Scale factors for trigger selection are used.	91
6.3	Dilepton mass for $\mu^+\mu^-$, e^+e^- and $e^\pm\mu^\mp$ channels. The Z +jets sample (blue area), for the $\mu^+\mu^-$ and e^+e^- channel, after all selection cuts, including $\cancel{E}_T > 40 \text{ GeV}$. For $e^\pm\mu^\mp$ channel no \cancel{E}_T cut is applied.	92
6.4	Number of b -tagged jets (CSVJ) for the $\mu^+\mu^-$, e^+e^- and $e^\pm\mu^\mp$ isolated dilepton dijet samples after requiring at least one b -tagged jet. For the $\mu^+\mu^-$ and e^+e^- channels, the events with $76 < m_{ll} < 106 \text{ GeV}$ or $\cancel{E}_T < 40 \text{ GeV}$ are rejected. The simulated samples are normalised to an integrated luminosity of 19.7 fb^{-1} . Scale factors for trigger, lepton selection and b -tagging are used.	93
6.5	Transverse momentum p_T of b -jets for the $\mu^+\mu^-$, e^+e^- and $e^\pm\mu^\mp$ isolated dilepton dijet samples. For the $\mu^+\mu^-$ and e^+e^- channels, the events with $76 < m_{ll} < 106 \text{ GeV}$ and $\cancel{E}_T < 40 \text{ GeV}$ are rejected. The simulated samples are normalised to an integrated luminosity of 19.7 fb^{-1} . Scale factors for trigger and lepton selection are used.	94

Chapter 1

Introduction

Standard Model explains all the fundamental particles and their interactions. It comprises leptons and quarks which build up matter, and gauge bosons, which mediate the exchange forces between them. Quarks and leptons are half integral spin particles (fermions), while bosons have integer spin. In the Parton picture, combinations of two or three quarks, held together by gluons, create hadrons, thereby defining their mass and quantum numbers. Baryons are made up of three quarks, while pairs of quark and antiquark constitute mesons.

The Large Hadron Collider (LHC) is a pp collider designed to discover new particles and shed light on processes that occur in an energy regime not accessible before. Particles emerging from the collisions are detected by experiments, which are located at the interaction points of the collider. Compact Muon Solenoid (CMS) is one of these experiments. It is a general-purpose detector to study electroweak symmetry breaking mechanism for which the Higgs mechanism is considered to be responsible, to look for evidence of physics beyond the Standard Model, to study aspects of heavy ion collisions and to explore high energy physics at the TeV scale involving particles with high masses.

At this point a detector control system has to be put in charge for the overall steering, monitoring and visualisation of the technical data. The detector control system of CMS experiment is very complicated to create and maintain. Since the system is computer based it may be sensitive to programming errors but it can also crash due to other disruptive factors like hardware failures, logical design errors and communication failures. To compensate this caveat a second layer of safety, the detector safety system, is introduced. It surveys the critical boundary condition of detector elements via hard wired probes. In case of an emergency it can override the detector control system and shut down the whole detector immediately by a hard power cut. This action does not require human

interaction. To create an easy to maintain and scalable software framework the different sub-detectors provided stand alone controlling and monitoring modules, which were developed independently by sub-detector experts. These modules were then connected in a hierarchical way to form a tree structure with a single point of control and monitoring at the top level. This enables the control and monitoring of the CMS sub-detectors by limited number of people.

The top quark, is studied in this thesis, which is the heaviest known elementary particle till today. It is the only quark that gives the possibility to study bare quark properties and to constrain the Standard Model parameters, like the Higgs mass. The top-pair production cross section is measured at the LHC with sufficient precision, the uncertainty of the measurement being limited by the systematics. With increasing luminosity at the LHC, additional systematic studies can be performed to minimise uncertainties, such that, luminosity uncertainty will become a dominant contribution.

The present thesis focuses on the implementation of Endcap Resistive Plate Chamber's control system for CMS experiment, as well as on the measurements of the top-quark pair production cross sections at a center of mass energy of 8 TeV with the CMS experiment. The work is organised as follows: The Standard Model is introduced in Chapter 1. In Chapter 2, the LHC machine and the CMS detector are described. An overview of the RPC system such as it's layout, geometry, modes of operation and performance parameters are discussed in chapter 3, followed by the general layered and modular architecture of Supervisory Control and Data Acquisition (SCADA) systems, description of the common framework developed at CERN to integrate control-specific tasks with HEP-related features, minimise the duplication of work and ensure the homogeneity of the developments are discussed. Also in chapter 5, event reconstruction and the corrections made to the simulated samples are discussed. The Data and Monte Carlo samples used for this analysis, their theoretical cross-sections, and the High Level Trigger paths can be found in chapter 6. In Chapter 7, Background estimation and systematic uncertainties needed for the statistical analysis are being discussed. Chapter 8, handles the usage of cut and count method analysis for the estimation of the $t\bar{t}$ production cross-section.

Chapter 2

Experimental Setup

2.1 The Large Hadron Collider

The LHC [1] is located at the site of the European Organization for Nuclear Research (CERN) near Geneva, Switzerland. In the LHC, two beams of protons are accelerated to an energy of up to 4 TeV . Later, the energy of the beams is supposed to be increased to the design value of 7 TeV . Each of the two beams consists of up to 2808 bunches of protons with up to 1.7×10^{11} particles per bunch. The two beams are flying opposite to each other and are collided at four locations around LHC. At each interaction point, there is an experiment, namely ALICE [2, 3], ATLAS [4, 5], CMS [6, 6], and LHCb [8], are located. The CMS experiment will be explained in abit detail in the coming sections.

The LHC is a 27 km circumferenced superconducting collider. The trajectory of the proton beams has to be bended on this ring. To achieve this trajectory of the proton beams of an energy of up to 7 TeV , the magnets are operated at a temperature of 1.9 K , cooled by 37 million kilograms of superfluid helium, to achieve superconductivity for the Niobium-Titanium windings of the magnets.

Before collisions may start at the interaction points in the LHC, the protons have to undergo several steps of acceleration. At the beginning, hydrogen gas is extracted from a gas bottle, the electrons are stripped off and the two atoms are split. Via a grid with constant negative charge, the protons are accelerated to the LINAC 2, where protons attain energy of 50 MeV . Before injecting these proton beams into the LHC tunnel, the beams are further accelerated via the BOOSTER, PS, and SPS synchrotrons to an energy of 450 GeV . Finally in LHC tunnel, the beams are then accelerated to 4 TeV , which gives rise to 8 TeV centre-of-mass (c.m) energy. Schematic diagram LHC accelerator complex can be found in figure 2.1. As LHC provides a unique performance in terms of beam and collision energy, beam intensity and event rate, several new effects appear, which did not

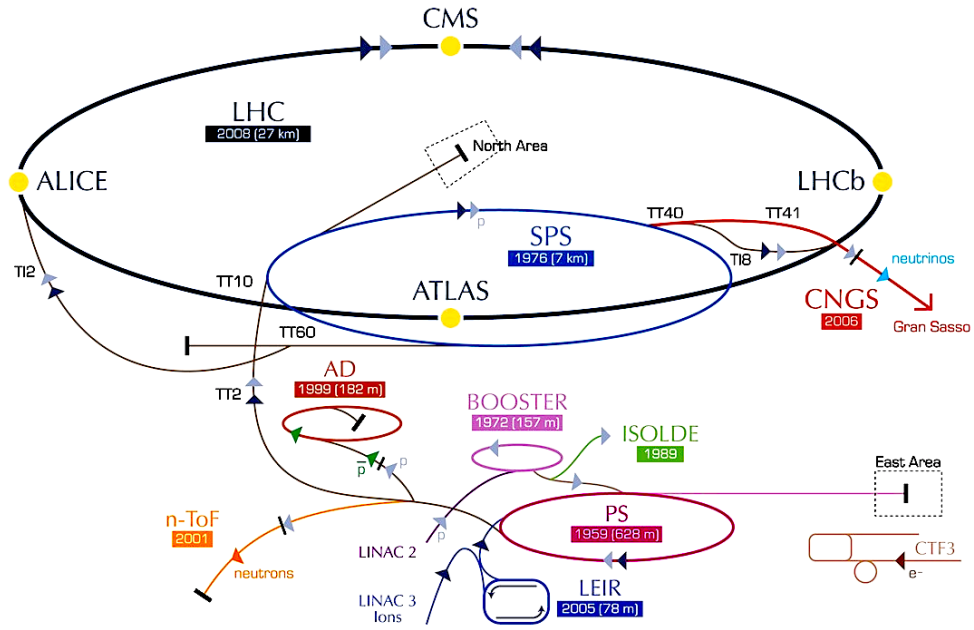


Figure 2.1: Schematic diagram of CERN accelerator [9].

play an important role ever before. The high beam energy requires a very strong magnetic field for the bending magnets to keep the beams on track. This leads to the fact, that the LHC is the first hadron collider where the energy loss due to synchrotron radiation of the protons plays an important role. In addition, the very high beam intensities lead to multiple pp interactions per bunch crossing, so-called pileup. These experiments had to find ways to identify and account for these additional interaction. The high bunch crossing rate leads to an enormous amount of data, which the experiments must deal with by selecting the most interesting processes. A summary of LHC's most important parameters can be found in table 2.1.

2.1.1 The experiments at the LHC

Along LHC, four interaction regions have been implemented. In these interaction regions, the curved shape of the accelerator is changed to a straight section where the protons of both beams are put on a collision course. Around the four interaction points, large particle detectors have been constructed as shown in figure 2.2. Out of these detectors, the CMS [11] and the ATLAS [12] are general purpose experiments, since their physics program is very wide. These detectors are designed for new searches like, phenomena beyond the Standard Model, as well as to conduct very precise measurements of already discovered particles like top quark.

Parameter	achieved in 2012	design value
proton energy	4 <i>TeV</i>	7 <i>TeV</i>
number of bunches	1374	2808
particles per bunch	1.7 x 10 ¹¹	1.15 x 10 ¹¹
bunch spacing	50 <i>ns</i>	25 <i>ns</i>
peak luminosity [<i>cm</i> ⁻² <i>s</i> ⁻¹]	7.7 x 10 ³³	1 x 10 ³⁴
bunch crossing rate	20 <i>MHz</i>	40 <i>MHz</i>
maximum of mean events per crossing	40	19
energy loss per turn	715 <i>eV</i>	6.71 <i>keV</i>
maximum field of bending magnets	4.76 <i>T</i>	8.33 <i>T</i>

Table 2.1: Some important parameters of LHC comparing achieved values from 2012 with design values. Values taken from [10].

In addition to these very huge general purpose detectors, two smaller and very specific experiments were installed. The first is the ALICE experiment [13]. This experiment mainly focuses on the study of quark-gluon plasma through analysis of heavy-ion collisions that are delivered by the LHC in between proton run-periods. The second is the LHCb experiment [14] which is designed to perform precision measurements in the *b*-quark sector.

Next to these four experiments installed around the interaction points, a detector named TOTEM [15] is installed close to the CMS interaction region. It is there to measure elastic proton scattering and total cross section of proton-proton collision. Finally, an experiment called LHCf [16] measures the particles created in the very forward region of the proton-proton collisions attempting to improve the understanding of ultra-high energetic cosmic rays.

2.1.2 The LHC run periods

The first collisions at 7 *TeV* centre-of-mass measurement were delivered by the LHC in March 2010 after a long commissioning period starting from September 2008 when a technical failure in the accelerator severely damaged a number of magnets. During the 2010 run, the LHC produced a data sample of 45 *pb*⁻¹ with a peak luminosity of around $2 \times 10^{32} \text{ cm}^{-2} \text{ s}^{-1}$. Although the peak luminosity is a factor 50 smaller than the design specification, the collisions were the most energetic ever opening the energy frontier at the LHC. During the first long run in 2011, the machine provided 7 *TeV* centre-of-mass energy at a peak luminosity of $4 \times 10^{33} \text{ cm}^{-2} \text{ s}^{-1}$ as shown in the right canvas of Figure

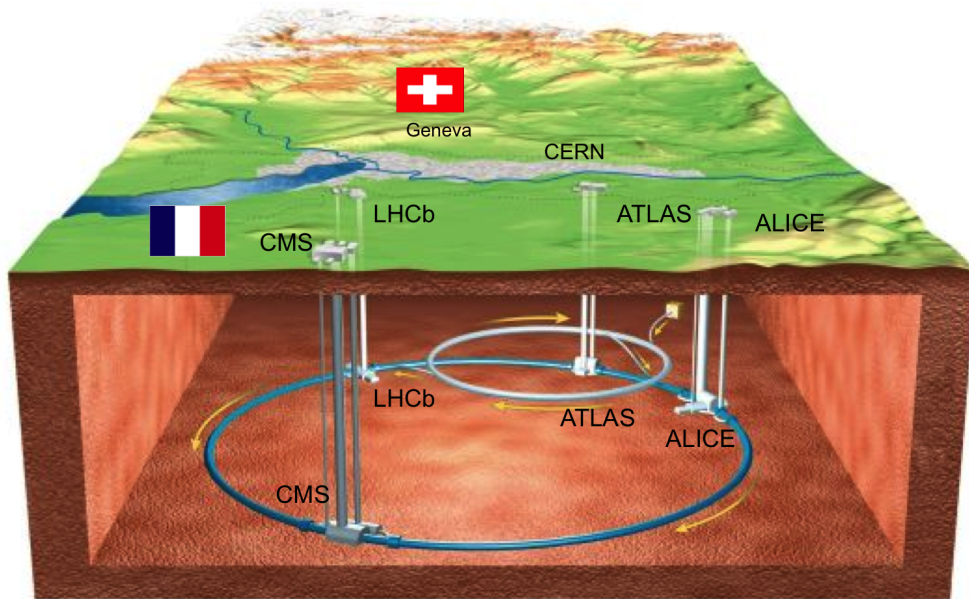


Figure 2.2: Schematic view of the LHC accelerator and location of its experiments.

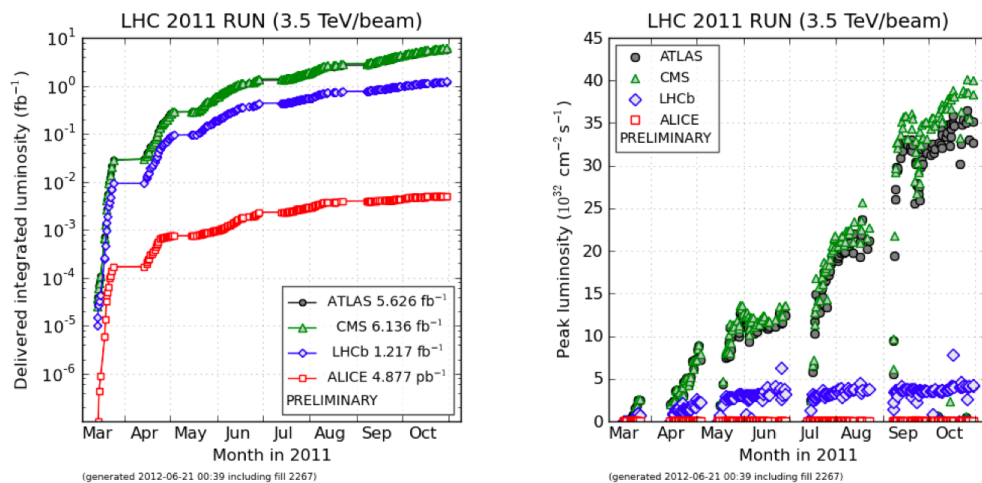


Figure 2.3: Integrated luminosity and peak luminosity as a function of time during 2011 operation of the LHC at $\sqrt{s} = 7 \text{ TeV}$ [17].

2.3. This provided a total integrated luminosity delivered to the experiments of 6.136 fb^{-1} which is $O(10^2)$ larger than during the 2010 run. Also the peak luminosity increased by a factor 20. This was up to that point in time the highest reached peak luminosity for a particle collider.

In 2012, the LHC beam energy was increased from 3.5 TeV per beam to 4 TeV resulting in 8 TeV centre-of-mass collisions. Continuing to build on the successful 2011 run, the peak luminosity delivered to the experiments increased again by a factor of almost 2 with respect to the 2011 run to little under $8 \times 10^{33} \text{ cm}^{-2}\text{s}^{-1}$ which comes very close to the design luminosity. During this run period, the LHC delivered a dataset of 23.269 fb^{-1} proton-proton collisions at 8 TeV , details are in figure 2.4. Currently, LHC is going through its first 2-year shutdown period gearing up for 13 TeV operation in 2015. The data sample generated during the 2012 runs will be studied in this work. High

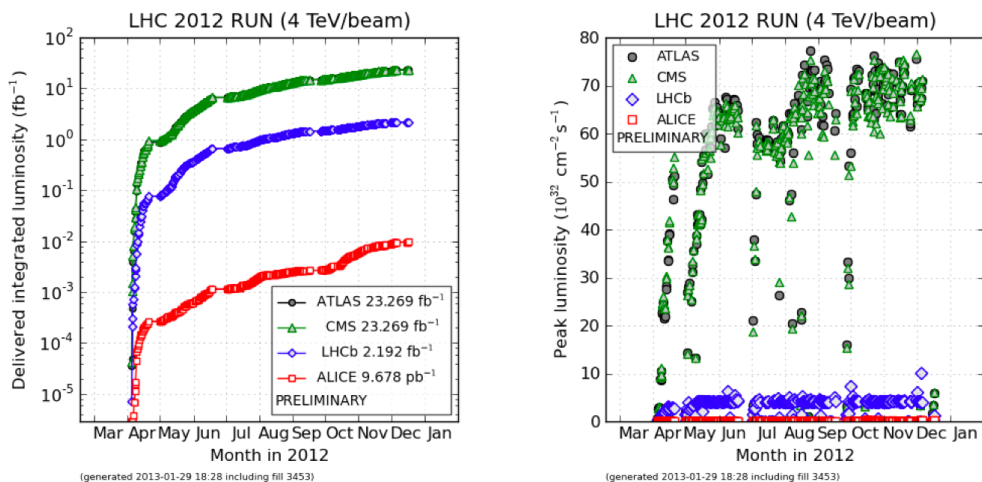


Figure 2.4: Integrated luminosity and peak luminosity as a function of time during 2011 operation of the LHC at $\sqrt{s} = 8 \text{ TeV}$ [17].

luminosity and large number of protons in each bunch, produce additional interactions in the experiment next to the central hard interaction, called pileup interactions. On the average 21 interactions interactions per bunch crossing are observed [18] as shown in figure 2.5. In this high-pileup environment it is difficult to determine which particle comes from which pp collision.

2.2 Compact Muon Solenoid

The Compact Muon Solenoid (CMS) experiment [6, 7] is one of the four experiments of LHC. An overview of detector and it's most important components are shown in

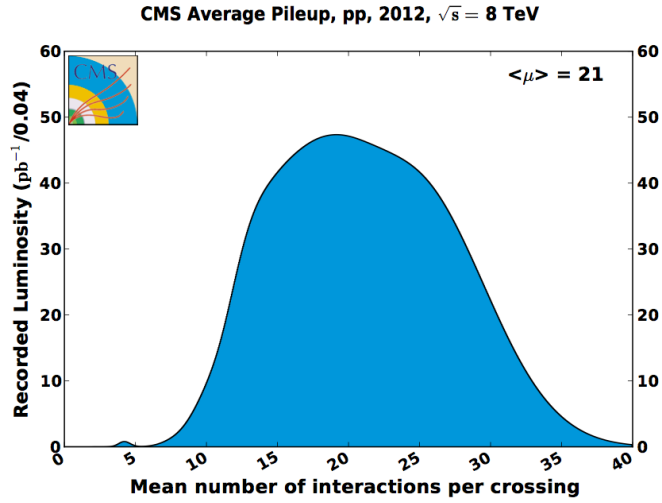


Figure 2.5: Integrated luminosity and peak luminosity as a function of time during 2011 operation of the LHC at $\sqrt{s} = 8 \text{ TeV}$ [17].

figure 2.7. In total, CMS weighs 14 000 t and it's length and diameter are 28.7 m and 15.0 m , respectively. The inner-most layers of CMS experiment consists of pixel sensors followed by the strip tracker, both being silicon sensors. The following two layers are the calorimeters, first the electromagnetic scintillating crystal calorimeter and second the hadronic brass-plastic sampling calorimeter. The calorimeters are succeeded by the superconducting solenoid coil magnet and the muon systems, which are crisscrossed by the return yoke made up of steel for it's large magnet.

Interaction point of CMS experiment is the origin of the right-handed coordinate system. The x , y , and z axes are pointing to the center of LHC ring, upwards, and along the beam direction (anticlockwise), respectively. From the positive z axis, the polar angle θ and azimuthal angle ϕ is measured in x - y plane. The pseudorapidity is a function of θ as is defined by $\eta = -\ln(\tan(\frac{\theta}{2}))$. Transverse momenta p_T is calculated from x and y components of momentum. Transverse energies E_T are energies scaled by the ratio of $\frac{p_T}{p}$.

2.2.1 Tracking System

In barrel region, the pixel detector have 53 cm long three layers along z -axis having radii 4.4 cm , 7.3 cm , and 10.2 cm and in end cap region, two pairs of discs reaching from a radius of 6 cm to 15 cm at $|z| = 34.5 \text{ cm}$ and 46.5 cm , respectively. So in each unit of size $100 \times 150 \mu m^2$, we have 66 million pixels, yielding an active area of 1 m^2 with the resolution of about 20 μm in z and 10 μm in r - ϕ .

CMS Detector

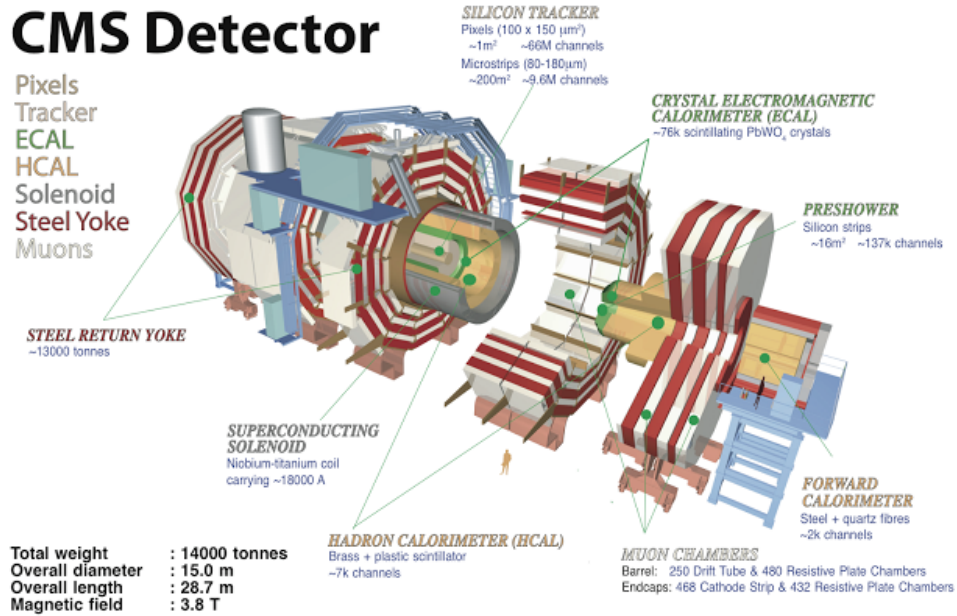


Figure 2.6: Overview of the CMS detector [11].

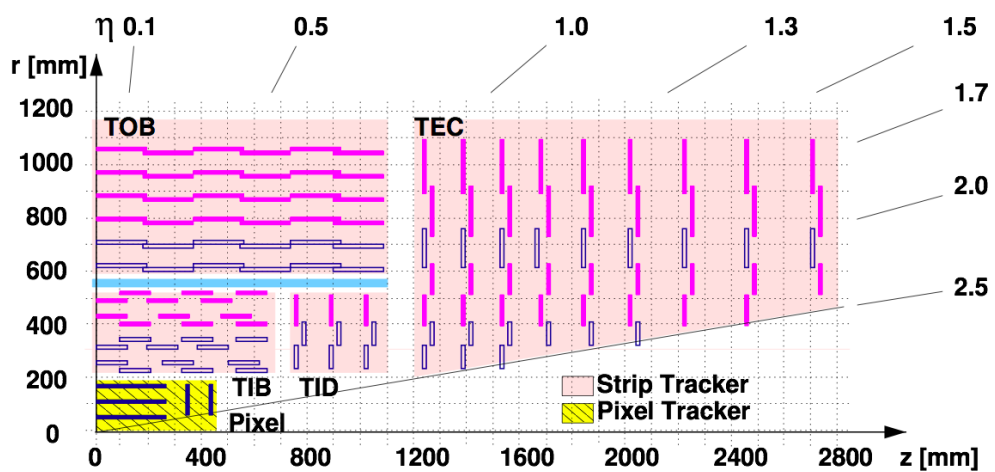


Figure 2.7: The r - z view of quarter part of CMS tracker. The modules indicated by open (blue) lines are stereo modules. Figure taken from [19] and modified.

The silicon strip detector contains ten barrel and twelve disc layers. Barrel part of strip detector consists of two regions, namely Tracker Inner Barrel (TIB) which further consists of 4 layers with $|z| < 65$ cm and Tracker Outer Barrel (TOB) which also further consists of 6 layers of length 2.2 m. The inner two layers of both barrel parts are stereo modules, each consists of back-to-back mounted two layers at an angle of 100 mrad, in order to provide hit position measurement along the direction of strip. Like barrel layers, endcaps are also divided into two parts, the Tracker Endcap (TEC) with nine discs ranging from 120 cm to 280 cm in $|z|$ and the Tracker Inner Discs (TID) with three discs filling the space between TIB, TOB, and TEC. Combining all modules, the strip detector provides 9.6 million channels and covers an area of 200 m².

The tracking system is contained in a temperature controlled support tube, held by a carbon-fibre structure.

2.2.2 Calorimeter System

The electromagnetic calorimeter (ECAL) is a homogeneous crystal calorimeter, built from 75,848 lead tungstate ($PbWO_4$) crystals. This has the advantage of low Moliere radius RM of 2.2 cm, fast response (80% of light emitted within 25 ns), short radiation length X_0 of 0.89 cm and it is radiation hard. The barrel part (EB) is built from 61 200 crystals, covering range of $|\eta| < 1.479$ and it has a thickness of 25.8 X_0 . The crystals are quasi-projective, meaning that they are tilted by 3° in ϕ and η w.r.t the nominal interaction point. Two endcap parts (EE) are built from 7324 crystals each, covering $1.479 < |\eta| < 3.0$ and 24.7 X_0 in thickness. The energy resolution σ of the electromagnetic calorimeter for photon or an electron of energy E is:

$$\left(\frac{\sigma}{E}\right)^2 = \left(\frac{2.83\%\sqrt{MeV}}{\sqrt{E}}\right)^2 + \left(\frac{124MeV}{E}\right)^2 + (0.26\%)^2 \quad (2.1)$$

The terms are describing stochastic effects in the showers, noise effects, non-uniformities and non-linearity's in the detector response, respectively.

The hadronic calorimeter (HCAL) is built up of brass and plastic scintillator. Brass being an absorber and plastic scintillator being an active material are connected to read-out with photodiodes via wavelength-shifting fiber. Three main parts are the forward (HF), endcap (HE) and barrel (HB) calorimeters covering $3.0 < |\eta| < 5.0$, $1.3 < |\eta| < 3.0$ and $0 < |\eta| < 1.4$ and these parts consists of 2 x 900, 2 x 1152 and 2304 towers, respectively. The energy resolution was simulated for a particle with a transverse energy

E_{MC}^T :

$$\left(\frac{\sigma\left(\frac{E_T^{rec}}{E_T^{MC}}\right)}{\left\langle \frac{E_T^{rec}}{E_T^{MC}} \right\rangle} \right) = \frac{5.6 GeV}{E_T^{MC}} + \frac{1.25\sqrt{GeV}}{\sqrt{E_T^{MC}}} + 0.033 \quad (2.2)$$

2.2.3 Magnet System

The prerequisite of an unambiguous muon charge determination up to a momentum of 1 TeV dictates the requirements for the magnet system. At CMS, a superconducting solenoid of 5.9 m in diameter and 12.9 m long was chosen. A current of 18 kA generates a magnetic field of 3.8 T in the superconducting coil with 2168 windings. The Niobium-Titanium cable has a total length of 53 km and an overall conductor cross section of $64 \times 22 \text{ mm}^2$. The magnetic field stores an energy of 2 GJ and the loop stress of the conductor is 64 atm .

2.2.4 Muon System

Muon system of CMS detector facilitates the identification of muons, as almost all charged particles passing through the calorimeters are muons. In addition, the momentum resolution for large momenta is improved w.r.t the inner tracker due to larger lever arm. The CMS muon system is based on resistive plate chambers, cathode strip chambers and drift tubes covering $0 < |\eta| < 2.1$, $0.9 < |\eta| < 2.4$ and $0 < |\eta| < 1.2$ respectively.

The 70 drift tubes make up four barrel layers at radii of 7.0 m , 5.9 m , 4.9 m , and 4.0 m and have a single point precision of about 200 μm . The two inner layers of drift tubes are covered on the inside and outside with resistive plate chambers, whereas the outer two layers are equipped with only one resistive plate chamber on the inside.

Each endcap consists of 234 cathode strip chambers grouped in four discs, providing both a faster and more precise signal. The spacial precision is about 200 μm . The inner three layers are covered with 384 resistive plate chambers on the outside up to $|\eta| = 1.6$.

2.2.5 Trigger System

The LHC ran with bunch crossing rates of up to 20 MHz , the maximum design value is 40 MHz . The data of only a few hundred bunch crossings may be saved per second. This necessitates an online rejection factor of several tens of thousands. The CMS trigger system does this in two steps. First, a very fast Level-1 trigger (L1T) keeps only about

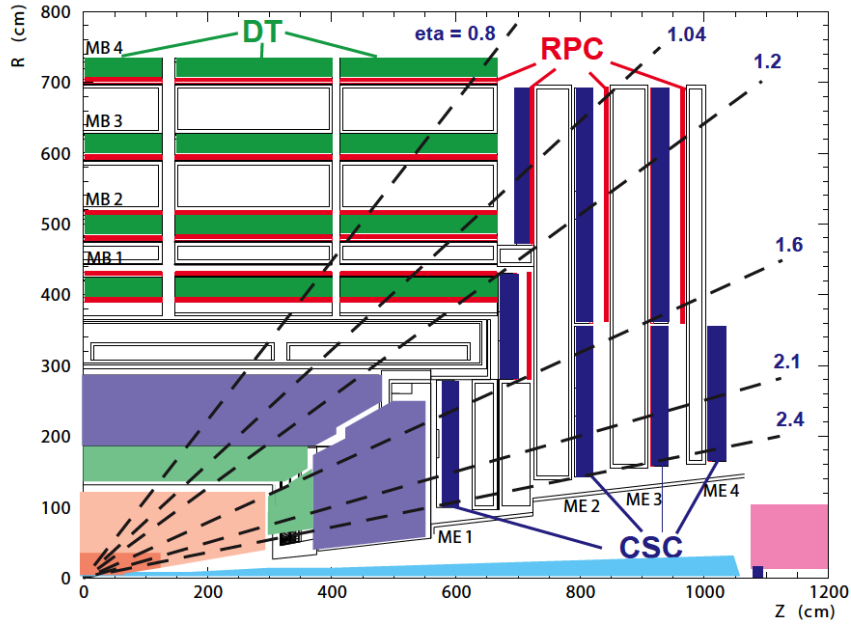


Figure 2.8: The r-z view of quarter part of CMS muon system [7].

one out of one thousand events. Then, the High-Level trigger (HLT) reduces the rate to only a few hundred events per second.

Custom hardware processors make up the Level-1 trigger. They reconstruct very coarse, primitive objects and keep only events where these simple objects basic transverse energy or momentum thresholds. The time to take the decision of keeping or rejecting the event is $3.2 \mu s$, which is equal to the time needed for data to be transmitted from detector electronics to trigger logic and back.

All events going through L1T are further processed by HLT, a huge processor farm. The High-Level trigger code may also contain very sophisticated algorithms for the object reconstruction and identification. The strategy is to discard an event as early as possible in order to save processing time. Thus, a partial reconstruction is done first for interesting regions marked by the Level-1 trigger. Later, additional information from muon and calorimeter systems is utilised. In the end, information from the strip and pixel detectors is added. All events which pass through HLT are written to the mass storage for analysis.

2.2.6 CMS Data taking during the 2011 and 2012 LHC runs

When the LHC machine is filled with two counter rotating proton beams and they are set to collide, the LHC experiments start recording the collisions. It is clear from the previous that an experiment like the CMS detector is very complex. Hence, recording

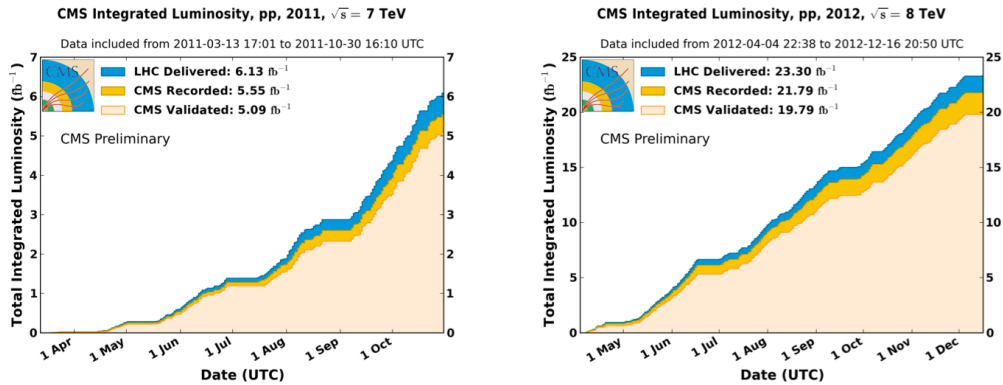


Figure 2.9: Integrated luminosity as a function of time during the 2011 and 2012 proton-proton running of the LHC at $\sqrt{s} = 7$ and 8 TeV [20]. The luminosity delivered by LHC is compared to the luminosity recorded by CMS. The validated luminosity depicts the data that is certified for physics analysis.

data with the CMS detector does not happen by flipping the "on/off"-switch. Conversely, operating the CMS experiment requires a 5-person shift crew to continuously steer and monitor the apparatus around the clock. In the control room, a person is in charge of the data acquisition (DAQ) system accompanied by another person that monitors the trigger. Furthermore, the integrity of the data is checked by a Data Quality Monitoring shifter and finally the operation is overseen by the shift leader. Last but not least, the Detector Control System shifter is assigned to oversee the hardware from cooling to high-voltage power and needs to respond quickly in the event of failure of any system.

Even with this continuous monitoring of the experiment, it sometimes happens that while the LHC is providing collisions, CMS is unable to record them. This could happen because the run is stopped by a malfunction of one of the subdetectors. The data recording is then resumed when the issue is fixed. This means that overall CMS is recording a little less integrated luminosity than the LHC is providing as is shown in Figure 2.9, where the recording efficiency of CMS is 90.5% in 2011 and 93.5% during 2012 operation.

Chapter 3

The Endcap RPC Detector Control System

3.1 Resistive Plate Chambers

The Resistive Plate Chamber are made up of two parallel plates, which are of Bakelite material whose bulk resistivity is around $10^9 - 10^{10} \Omega cm$, they are separated by a gap of $2 mm$ which contains gas mixture[21]. The outer surface of resistive material is painted with conducting graphite, to make them act like high voltage and ground electrodes. Copper strips which are used to perform readout of the chambers, are separated from the graphite coating by using insulating Polyethylene (PET) film. At LHC, the beam crossing time of $25 ns$, so RPCs should have an excellent time resolution. These are the dedicated chambers used for the first level muon trigger. The good performance of RPC is very essential in assigning the muon to the right bunch crossing. The event rate at LHC is expected to be extremely high due to the large total pp cross-section at $\sqrt{s} = 14 TeV$. The expected event rate is $40 MHz$ which is unmanageable, Level-1 (L1) trigger is applied to reduce this size to $100 KHz$. This rate at the output of L1 is too high to be stored, therefore the high level trigger is applied and the final event rate is brought down to the $100 Hz$. At L1 trigger the available time for the detector is $25 ns$, which implies fast trigger system. Resistive Plate Chambers (RPCs) are good candidates for fast triggering, where the spatial resolution is not important but fast timing information is more important. The cross-sectional view of the CMS is shown in figure 3.1. RPCs are installed on CMS in barrel region as well as in endcap region. There are three disks of endcap RPCs on each side of CMS i.e $RE\pm 1$, $RE\pm 2$ and $RE\pm 3$. The each disk constitute of three rings, the outer one is named as $RE^*/3$, middle one is named $RE^*/2$ while inner one is named $RE^*/1$ and each ring contains 36 RPC.

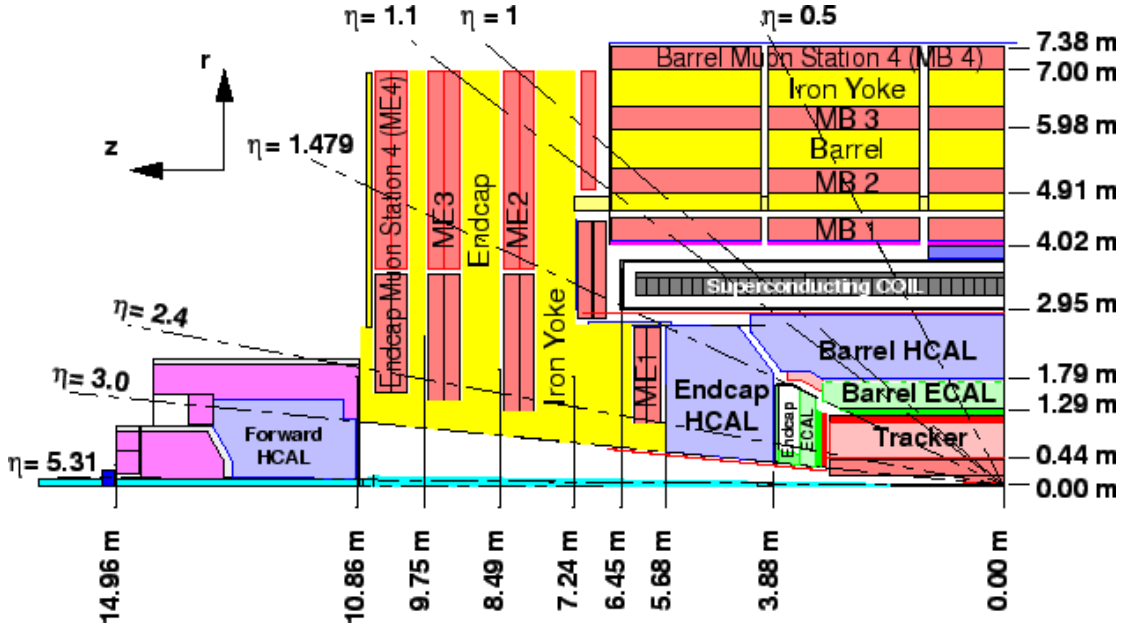


Figure 3.1: View of a quadrant of CMS in rz -plane where MB and ME are the Barrel and EndCap Muon system layout.

Each Endcap RPC station consists of double-gap trapezoidal shaped chambers which are arranged in three concentric rings, see figure 3.2(left). In station one, innermost ring of the chambers span 20° in ϕ direction, and all other chambers overlap in ϕ direction in order to avoid dead space at chamber edges and they span 10° ϕ direction. Station one is mounted underneath the CSC chambers of ME1, on the interaction point (IP) side of the first Endcap disk (called YE1), see figure 3.2(right). Each RPC can be represented by $RE\pm D/R-N$, where D and R represent the Disk number and Ring number respectively while N represent the number of RPC in each Disk. The size of RPCs increases from inner to outer rings, also known as layers. The chambers on $RE^*/2$ and $RE^*/3$ can be seen in figure 3.3. A major part for assembling and commissioning of endcap RPCs has been contributed by Pakistan for CMS. The four complete disks $RE\pm 2$ and $RE\pm 3$ were assembled and tested in Pakistan.

No chambers of type $RE^*/1$ were built at the time of commissioning in 2008. The chambers for $RE^*/2$ and $RE^*/3$ rings of disk 2 and disk3 are assembled and tested in NCP, Pakistan while same rings for disk1 were contributed by China. The endcap RPCs disks $RE\pm 1$, $RE\pm 2$ and $RE\pm 3$ are commissioned by the Pakistani team at CMS during 2008-09.

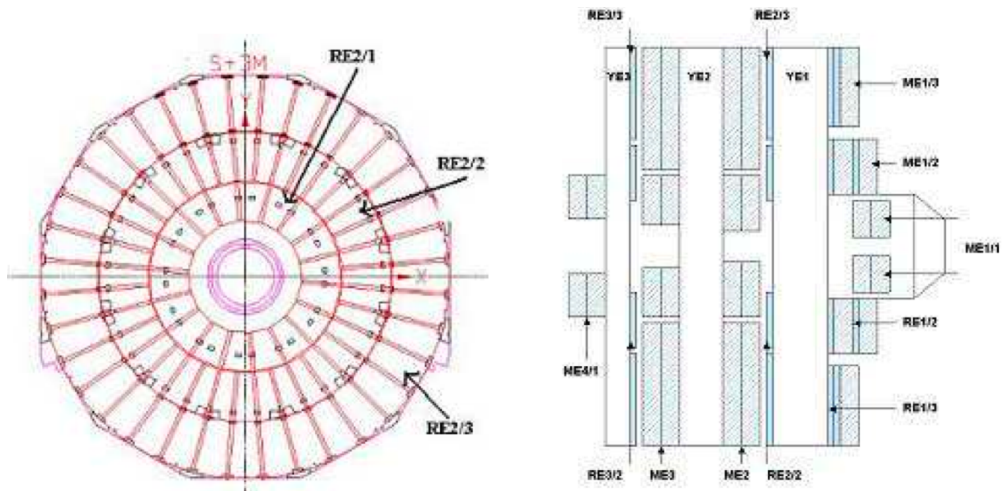


Figure 3.2: RPC Detector Endcap schematic layout, left figure shows RE2 RPC disc's $r-\phi$ layout, which is at the back side of the first endcap yoke, while right figure shows layout of the entire CMS endcap muon system[22].

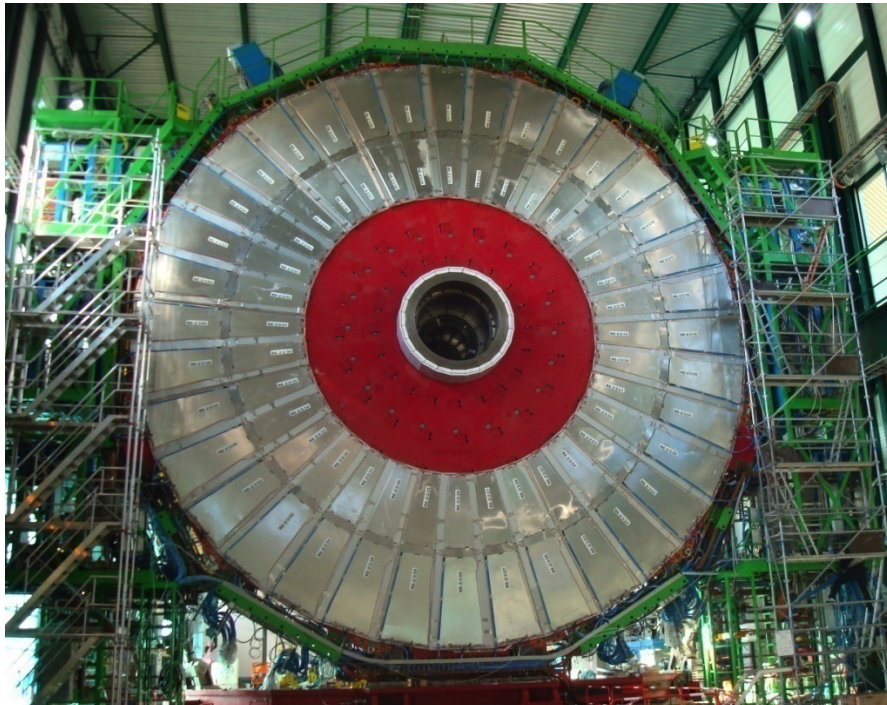


Figure 3.3: A complete EndCap RPC Disk of CMS. The RPCs are installed in Ring2 and Ring3 where Ring1 is empty.

3.1.1 Layout and Geometry of End-Cap RPCs

Layout

A schematic representation of a trigger RPC is shown in figure 3.4. From top to bottom the following layers can be seen: an insulating PET film, a graphite layer to make the high voltage(HV) contact(painted on the electrode), a resistive(Bakelite) electrode, a gas gap, a resistive(Bakelite) electrode, a graphite layer to make the ground contact(painted on the electrode), an insulating PET film and the readout strips. There are other types

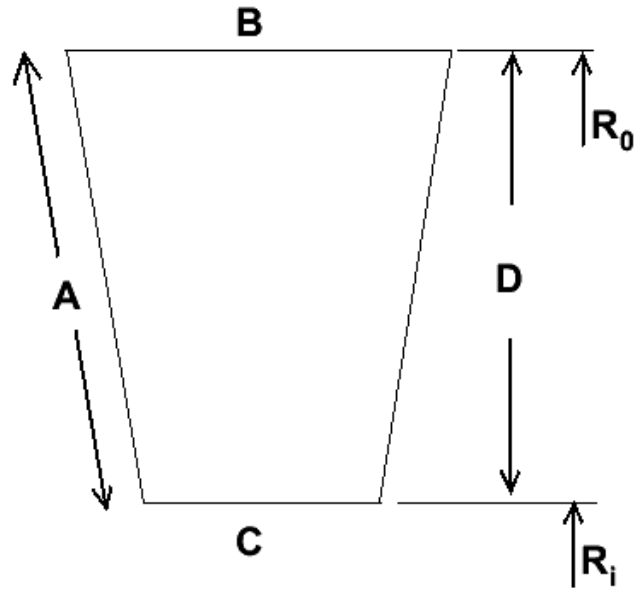


Figure 3.4: Geometry of a Resistor Plate Chamber where, R_0 and R_i are radii from beam line at low and high eta respectively.

of RPCs than trigger RPCs. They differ in materials, dimensions or even configuration. The basic working principle is always same, but characteristics such as the magnitude of the induced charge or the timing performance can differ.

Geometry

The Endcap RPCs cover 10 degrees in ϕ due to its trapezoidal shape, also its strips have the same shape. The RPC Endcap chambers have double gap symmetry along with 96 readout strips which are perpendicular to the beam line in ϕ direction. Table 3.1 shows the geometrical details of RPCs and corresponding parameters are displayed in figure 3.5.

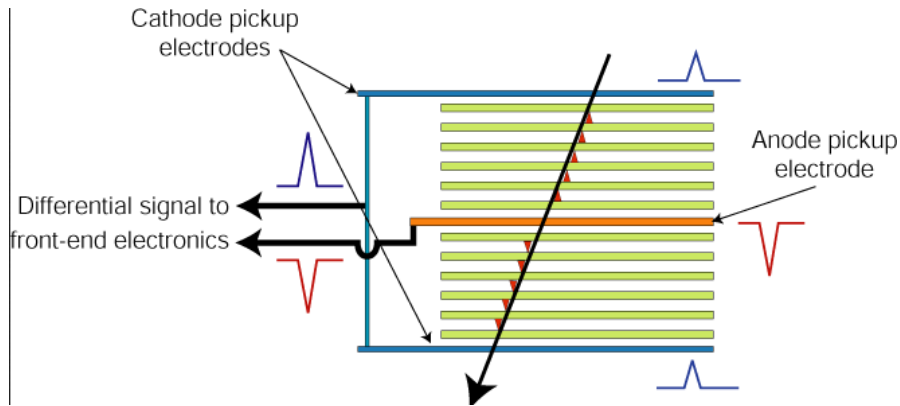


Figure 3.5: Geometry of a Resistive Plate Chamber

Station	R_i	Chambers	A(mm)	B(mm)	C(mm)	D(mm)	Area(m ²)
RE 2/2	3299	72	1693	979	684	1687	1.403
RE 2/3	5001	72	1961	1323	981	1954	1.917
RE 3/2	3299	72	1693	979	684	1687	1.403
RE 3/3	5001	72	1961	1323	981	1954	1.917
Total	-	288	-	-	-	-	513.2

Table 3.1: Dimensions of RPC installed in Ring2 and Ring3.

3.1.2 Modes of Operation

Original RPCs were single gap counters, operating in steamer mode. After that double gap structure of RPCs was introduced which were operated in avalanche mode, in order to improve the detection efficiency, which extends its counting rate capabilities.

Streamer Mode: In streamer mode the electric field inside the gap is kept intense enough to generate the limited discharges localised near the crossing of ionising particle. The resulting signal size is large but the rate capability obtained in such operational conditions is limited (100 Hz/cm²) which is not suitable for LHC. The rate capability is low because the time to recharge resistive plates and to be ready for next signal is long. The drop in the efficiency is due to the streamer mode discharge, which cause a serious drop of E field of the gas gap. High resistivity of the chamber plate prevents rapid transmission of electric charge through them. In order to improve the chamber efficiency at higher rates one should operate it in the proportional mode, where the charge in a single avalanche is much smaller than in the case of streamer. This mode of operation at high gain may be reached by using gases containing high percentage of freon, which limit the formation of streamer discharges.

Avalanche Mode: In avalanche mode no streamer is formed and the signal results only from gas amplification during the avalanche process caused by secondary ionisation. The resulting signal is significantly lower than that in the streamer mode whereas the rate capability is greatly improved. Originally, RPCs were used only in streamer mode because it was difficult to carry out stable operation of RPCs due to streamer sparks in the single gap RPCs. Today, double-gap or multi-gap RPCs are suitable for avalanche mode. These detectors can be operated at high rates, which are required for the muon trigger, also the efficiency increases by a factor of 10. That is why Avalanche mode RPCs are being used in ATLAS, LHCb and CMS experiments at CERN.

3.1.3 RPC Performance Parameters

Performance of RPC is determined from its behavior which can be determined by different parameters. These parameters are occupancy, efficiency, cluster size, time resolution, dead time and rate capability. Their details are given below.

Occupancy: It gives region of RPC, which can detect a muon, or a region which is alive. This number depends on the number of strips in that region and efficiency of RPCs.

Efficiency: It is the ratio of working strips to total strips in an RPC. For an ideal detector efficiency should be 100%. But in real life a good detector will have efficiency above 95%.

Efficiency plateau: When efficiency of RPC is measured vs voltage applied across gaps then the resulting curve behaves like an error function i.e it starts from low values, quickly increases to highest value and stays constant for a certain range of voltage. The part where efficiency is highest and constant is called the efficiency plateau.

Cluster sizer: It is number of consecutive strips which collect signal (charge) due to a muon passing through gaps. We can have a muon for which all charge is collected by one strip or if it passes through junction of two strips then charge is collected by two strips. Thus avalanche size at the end of 2 mm gap should not be wider than two strips. Experimentally this value lies close to 2.

Dark current: It is a current which is detected in electronics when there is no voltage applied across gas gap. The sources of dark current could be leakage current, loose electronics etc.

Dead Time: It is period of time during which a detector can not detect a particle passing through it. The reason of dead time is a muon which has already ionized the gas molecules and lowered the voltage across gaps. We can not make dead time zero as

ionized gas takes some time to get neutral again.

Time Resolution: It is time during which signal is collected by RPC.

Rate Capability: It gives number of charged particles which can be detected in unit area in unit time. This number depends on the granularity of a detector as well as on its dead time and time resolution.

For best performance assembled RPC has to fulfill the following conditions before installation at the CMS detector:

- Cluster Size < 3 .
- efficiency $> 97\%$
- Operation Efficiency plateau $> 400\text{ V}$.
- Time resolution $< 3\text{ ns}$.
- Dead time around 3 ns .
- Rate Capability $> 1\text{ KHz/cm}^2$.

3.2 RPC Endcap Control System

The RPC End-Cap Control System (RECS) consists of several standalone modules for each sub system. The organisation and relationship of these components can be found in figure 3.6. In this section we will have a brief overview of the RECS and we will focus in detail on the modules of High Voltage, Low Voltage, Cooling and Humidity, which have been contributed to the CMS collaboration during this thesis. The statistical display shows the overall condition and change behaviour of the parameters by using histograms. The result is a gaussian distribution, or a sharp peak in case of changes. The following list provides an overview of all major modules that form the complete CMS End-Cap DCS:

1. HV Control
2. LV Control
3. Gas Control
4. Temperature and Humidity Monitoring

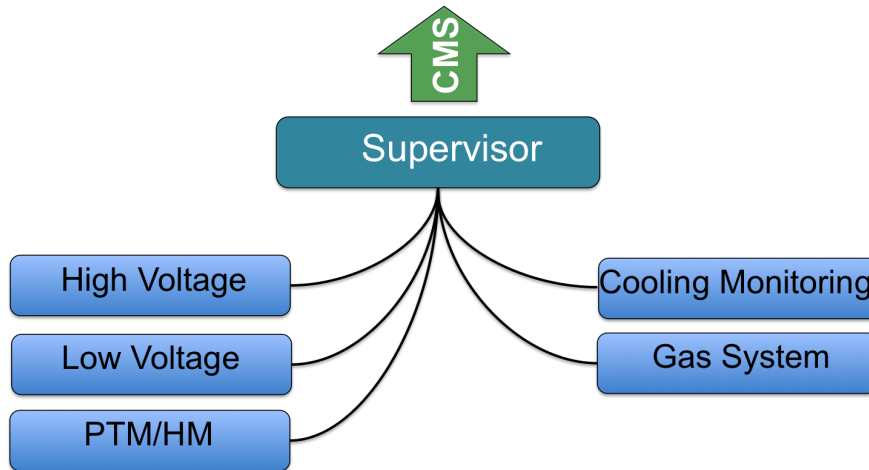


Figure 3.6: The RE DCS software schema. All sub components are summarised and can be controlled from a single module, the Supervisor. Finally the Supervisor will uplink to the so called Central DCS, where all sub detector controls and status summaries are united.

All End-Cap DCS modules can operate independently as standalone applications, but they provide interfaces to a higher instance; the Supervisor (see Section 3.2.5). The Supervisor summarises the status of all connected sub components and it displays important parameters to the operator. The RPC (Endcap and Barrel) Supervisor itself links up to a higher instance; the Central DCS. The Central DCS is summarising the status of all sub detector components to one screen, which enables a single operator to stay informed of the status of the CMS detector and grants him basic control commands for the whole detector. The Current End-Cap DCS setup is located in one of the experimental service caverns at P5.

3.2.1 Software Framework

The Endcap DCS is developed on base of the software framework Process Visualisation and Steering System (PVSS)[23]. PVSS is a "Supervisory Control and Data Acquisition" (SCADA) system [24], a software which manages automatically very complex systems, such as plants and factories, from few or even only one computer. Such software gathers information from all components of the system and acts automatically to operate the system. Usually, a finite-state machine[25], implemented in the SCADA software, defines, what actions have to be taken under which conditions. The idea of a finite-state machine is shortly introduced in later subsection. Normally, the SCADA software displays information about the system and allows intervention by human through a graphical user

interface. The following subsection introduces the overall hierarchy of the Endcap RPC SCADA system.

The screenshot shows a script editor window titled 'Script Editor (System1 - SvnPluginDev, #1)'. The window contains a list of functions on the left and a main code area on the right. The code is written in a C-like language and includes functions for SVN operations such as `getSvnLog` and `getSvnDiff`. The `getSvnLog` function (lines 516-528) takes a file path and a synchronized flag as input, resolves the local path, and uses `SVN_command` to execute a log command. The `getSvnDiff` function (lines 532-536) also takes a file path and a synchronized flag as input and uses `SVN_command` to execute a diff command. The code includes comments and uses `returnValue` to store and return data.

Figure 3.7: CTRL script editor.

PVSS

PVSS(Process Visualisation and Steering System) is a SCADA(Supervisory Control and Data Acquisition) software from ETM[26], which is itself owned by SIEMENS. It runs on Microsoft Windows and Linux machines and is designed to work as a distributed system. This means multiple interconnected projects can be spread over several PCs, which is providing good scaling capabilities.

The PVSS software provides an Integrated Development Environment (IDE), that can be used to design the panels by drag and drop. Single elements of the panel can be configured using scripts in a C like language (see figure 3.7). Possible entry points for these scripts can be `OnClick`, `OnDoubleClick`, `OnInitilise` and others. The information and configuration of the PVSS projects is stored in Data Points (DPs), an example of which is shown in figure 3.8. First one has to define the DP type, which acts as a template for later DP instances. The DP type can have an arbitrary substructure of

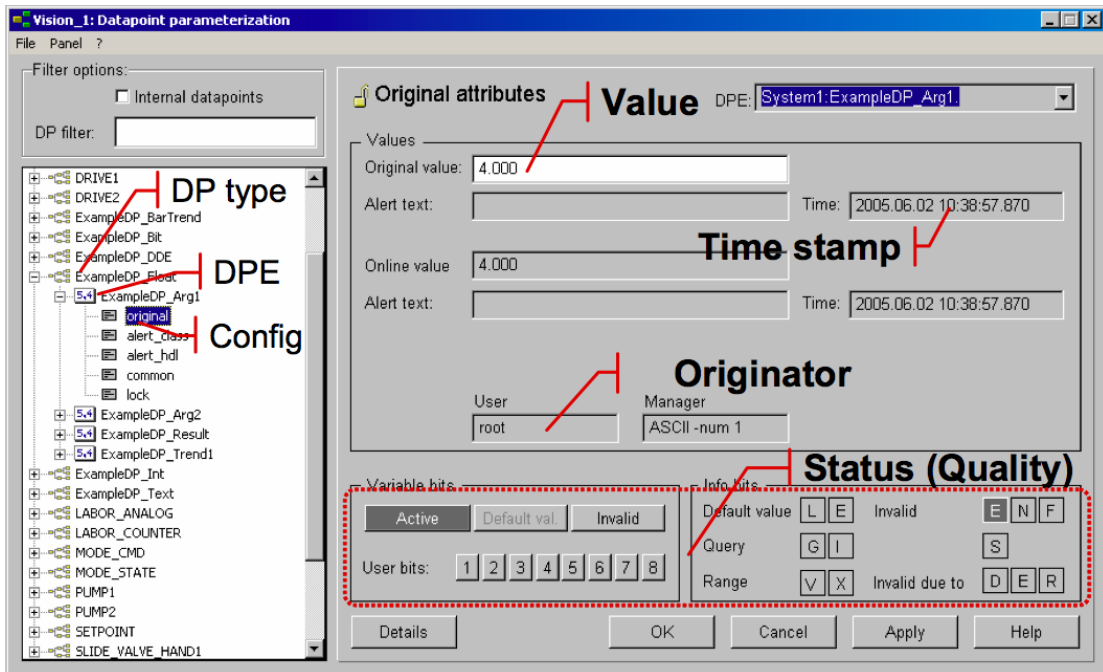


Figure 3.8: PARA database editor - datapoint type "*ExampleDP_Float*" with datapoint "*ExampleDP_Arg1*".

values and sub folders, for grouping values that are interrelated. When the desired DP type has been designed, one can create as many instances as needed. Any instance is automatically provided with a unique identifier.

Scaling

A running PVSS project consists of several individual processes, called Managers, which handle a specific task each. These managers form a client/server infrastructure (see figure 3.9). This fact enables a project to run dedicated parts of the FSM(Finite State Machine) (the partitions) on several computers. The possibility to spread an application over an arbitrary number of computers allows the construction of arbitrarily complex FSM systems. PVSS also provides special managers for running custom scripts and UI(User Interface) elements. The communication between managers of a specific application is done via TCP/IP(Transmission Control Protocol / Internet Protocol), which makes ethernet sufficient for interconnecting several computers over arbitrary distances.

JCOP Framework

JCOP(Joint Controls Project) is a collaboration between CERN and the LHC experiments to provide common context solutions to be used in the experiment's DCS. The

PVSS Manager Communication

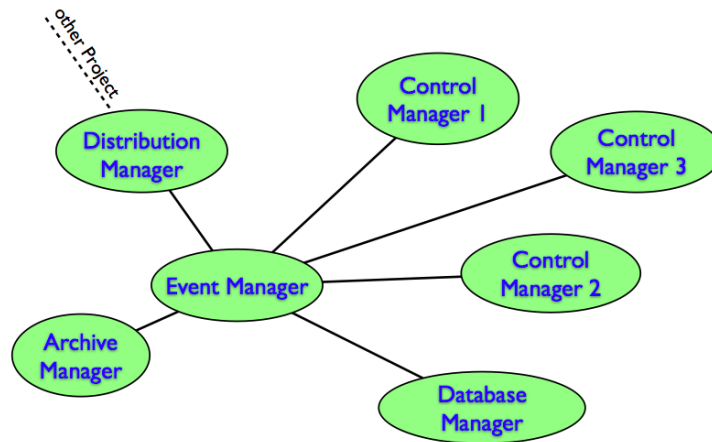


Figure 3.9: The manager communication structure of a typical PVSS project.

software guidelines and tools provide a level of abstraction on top of PVSS to allow easy configuration of archiving, user authentication, alarm handling, plotting, FSM, component installation, database access and so on. The JCOP framework also provides complete standalone tools such as the installation tool. This component manages the installation, reinstallation and deletion of components. It is provided with a DB(Database) connection to automate the installation according to a template of the current machine (see figure 3.10). Another tool provided by the framework is the Device Editor Navigator (see figure 3.11(a)). The Device Editor Navigator displays and edits the installed real or virtual hardware on the corresponding machine. In case of the HV system it lists the power supplies (see Section 3.2.2), which are real hardware. On the second tab it provides a logical view, which is useful to group hardware in a functional way as also shown in figure 3.11(a). The tab also provides the user with an integrated editor to manipulate the view. On the contrary, the hardware view provides a view of the system that is based on direct dependencies between the hardware as shown in figure 3.11(b). The third tab provides the FSM view and editor (see section 3.2.2).

Most of the configuration of the system can be done within the provided GUI based editors of the various components. For large and complex systems it is more efficient to script the creation and configuration of a project by using the APIs provided by the components themselves. Once the component is fully set up, its structure and configuration can be saved to the Configuration DB, from where it can be reinstalled and reconfigured whenever needed. In case of a script based component creation, as is done

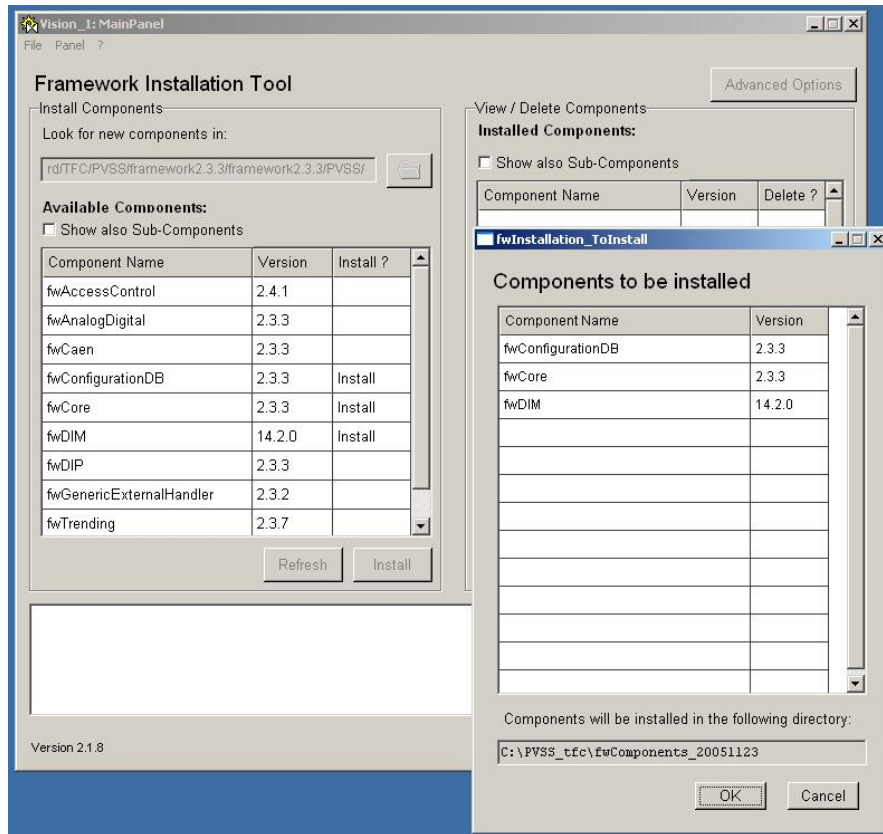


Figure 3.10: JCOP Framework component installer. This component manages the installation, reinstallation and deletion of components. It is provided with a DB connection to automate the installation according to a template of the current machine.

for Temperature Monitoring, these creation scripts can be run anytime to recreate and install the component. In addition a specific configuration for the data points could be retrieved from the Configuration DB.

3.2.2 The Power Supply for RE System

The RE Power Supply System is responsible to control and distribute the voltages to each and every chamber and all the equipment's which are involved in the operation of RE chambers. The high granularity and the complexity of the RE system require challenging constraints while developing power distribution system, specially when we have to operate them in the hostile environment.

High Voltage System

For RE muon system, major portion of the power supply system is situated very close to the detector i.e. inside the balcony racks located at both sides the endcap disks. It is

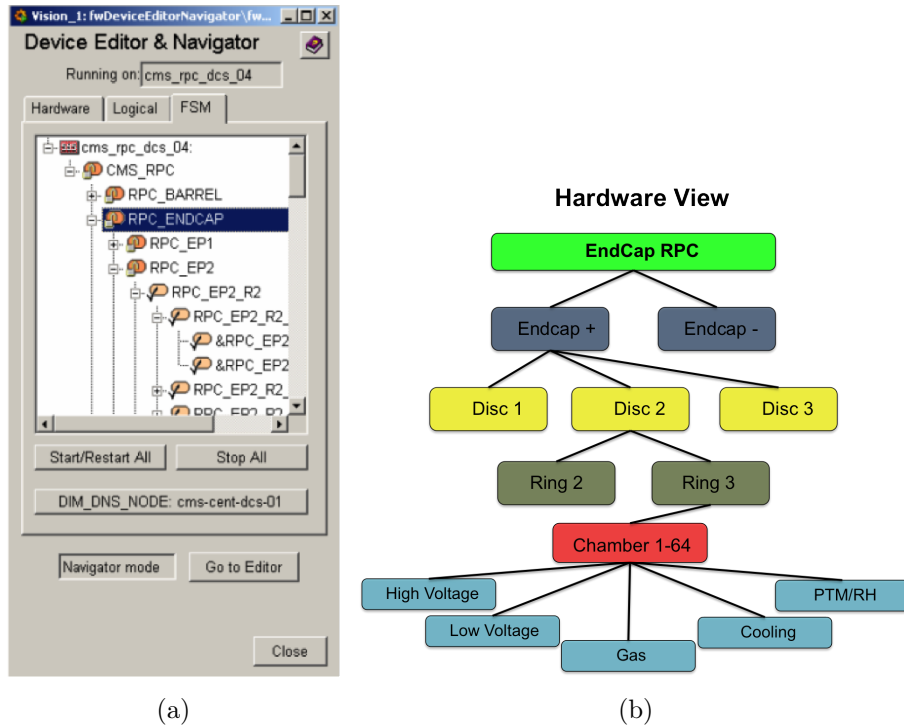


Figure 3.11: Device Editor Navigator(left), Real Hardware View(right)

the area where the magnetic field can attain value up to 6×10^{-2} Tesla, as well as the radiation can be up to 107 proton/cm^2 and $5 \times 10^{10} \text{ neutron/cm}^2$ [27]. The RE power system was designed in a way that the environmental requirements are fulfilled, also to minimised the probability of having inefficient or dead areas due to the failure of some RE power channels.

Each RE chamber needs two independent floating HV channels (one-per-layer) to operate. In side the gas gap electric field is generated due to these HV lines, so operating voltage for RPCs is 9.2 kV , limit of dark current is $10 \mu\text{A}$ per chamber, and trip time is 10 sec, There are three RPC stations on each side of CMS namely RE+1, RE+2, RE+3, RE-1, RE-2 and RE-3. Each station has 72 RPCs installed on Disk-2 and Disk-3. Therefore it counts to 432 chambers on six stations. As we have a double gap symmetry, HV is supplied to top and bottom gaps separately, which makes a total count of 864 channels, which are needed to be controlled with HV control system. Hardware used for HV system is shown in table 3.2. The names are listed by top down hierarchy. High voltage modules are very expensive. So In order to minimise the cost by a factor of 4, high voltage distribution boxes are used to distribute the power. The high voltage distributor actually converts a single input voltage into four output voltages as can be seen in figure 3.12, two each for bottom and top gaps. The boxes were prepared at ISR.

No.	Model	Name	Quantity
1	SY1527	HV Mainframe	1
2	A3485N	3-phase AC/DCs Converter (MAO)	1
3	A1676N	Branch Controller	3
4	EASY 3000	Easy Crates	8
5	A34FU	Fan Units for Easy Crates	8
6	A3512N	High Voltage Modules	36
7	Home Made	HV Distribution Boxes	24

Table 3.2: Hardware used in High Voltage System

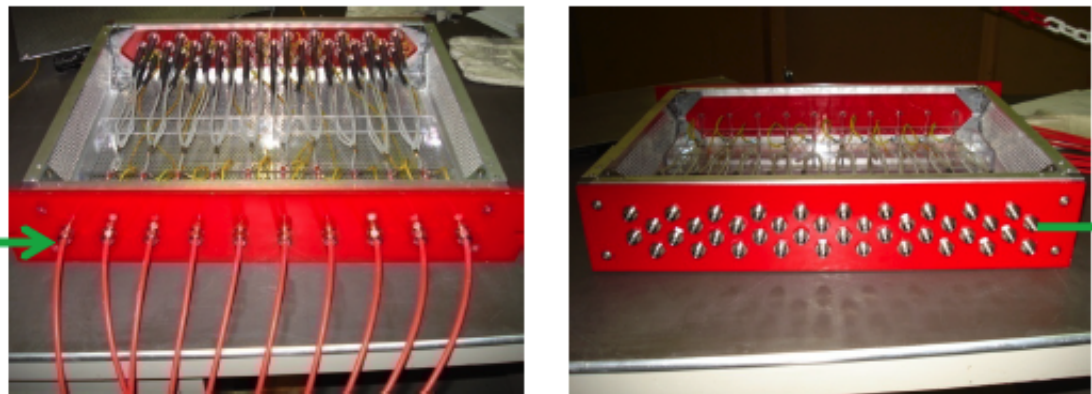


Figure 3.12: HV distribution box

Low Voltage System

In addition to high voltage, each RE chamber requires to operate 2 independent low voltage channels to power up the Front End Boards (FEBs), we require the analogue and the digital voltages for each FEB chip's operation. Also for Link Boards which are located at the balcony racks, close to the detector, in the experimental cavern, we need additional low voltage channels to operate them.

The RE Low voltage System is used to power up Front End Boards (FEB) of the 432 chambers and their corresponding Link Board Boxes (LBB) located in the LV-Racks. One FEB can read 32 read-out strips, each chamber has 96 charge collecting strips, therefore we have 3 FEBs mounted on each chamber. The FEBs are first in the readout chain to get the signal from readout strips of RPCs. This signal is then sent to the Link Boards (LBs) present inside Link Board Boxes (LBBs). The LBs send data to control room via optical fibers. Therefore the entire RE LV power system consists of:

- 432 LV channels for FEBs located on the chambers,
- 144 LV channels for LBBs.

Hardware used for LV system is listed in table 3.3.

No.	Model	Name	Quantity
1	SY1527	LV Mainframe	1
2	A3485S	3-phase AC/DCs Converter (MAO)	12
3	A1676N	Branch Controller	4
4	EASY 3000S	Easy Crates	24
5	A34FU	Fan Units for Easy Crates	24
6	A3009	LV FEB Modules	36
7	A3016	LV LBB Modules	24

Table 3.3: Hardware used in Low Voltage System.

CAEN EASY SYSTEM and RE DCS

The RPC collaboration has chosen a solution for the power supply system, which is based on the CAEN EASY [28] (Embedded Assembly SYstem) project, which consists of magnetic field and radiation tolerant electronic components, and it is also based on master-slave architecture. Control part which is made up of such components which are not-radiation hard could be separated from those which can operate in the presence

radiations, like supply modules. The Power Supply System has a modular based approach in which controllers and crates are common. So we select power supply modules as per our need.

The control part of RE DCS is accomplished by SY1527 Mainframe controller which is based on CAEN EASY technology. CAEN Mainframe by means of branch controllers, communicates and controls crates via CAN bus which are located faraway (several meters). This master part should to be located in an accessible and safe area like electronics room. Two possible configurations could be adopted, in the first configuration we can place the entire power supply system in electronics rooms, a place where we have safe environment, in the second configuration we can separate power modules from the control unit, place the control unit in the counting room, while power modules in the cavern area close to the detector, as power modules are radiation tolerant. Both configurations are being used for our power system, as shown in the figure 3.13. We have used the first configuration for High Voltage system, as the current required in this case is $\approx O(6)$ less than Low Voltage, so that one can easily locate and fix problems regarding distribution and connection of the High Voltage system. Second option is being used for the Low Voltage system, where we are using 200m long cables, so we need high current also we need to avoid the consequential high large voltage drop.

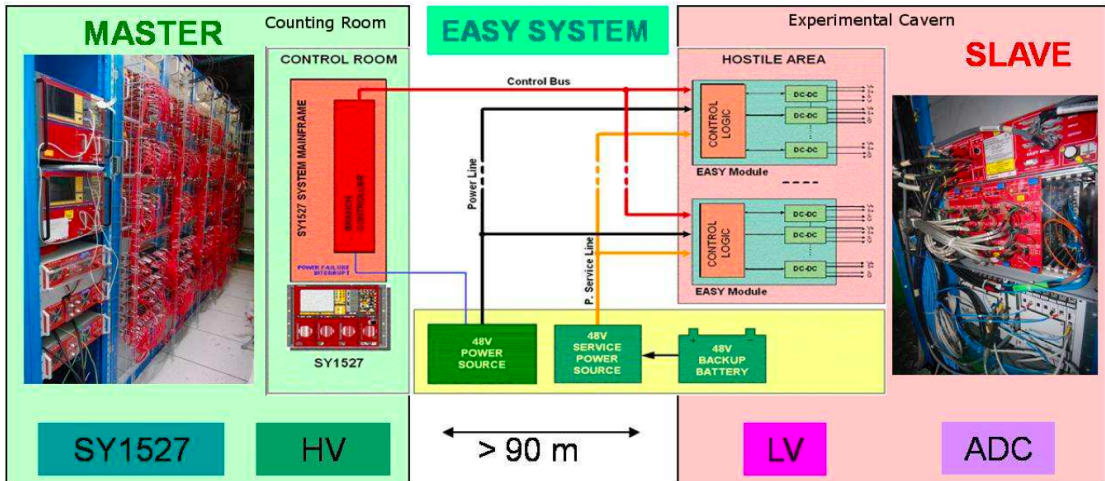


Figure 3.13: Schematic overview of the CAEN EASY Power Supply System.

The Endcap RPC detector power system requirements are summarised in table 3.4. During three years time i.e from 2006 to 2009, CAEN prepared different prototypes of EASY power supply boards and were tested at CERN in building 904 facilities. RPC community together with CAEN engineers, after testing and optimisation, we achieved

a board operation which was satisfactory in term of reliability, operational stability and read-out precision, according to the RPC community requirements. The Endcap RPC power supply system configuration consists of 36 EASY CAEN A3009 Low Voltage boards to power up the FEB electronics, in addition to FEBs it contains 24 EASY CAEN A3016 Low Voltage boards to power up the LBBs, whereas the system of High Voltage instead consists of 36 EASY CAEN A3512N boards [28]. The High Voltage boards are designed for an output voltage which can be monitored and programmed within the range of 0-12 kV with the resolution of 1 V and also it can monitor current resolution of 0.1 μA .

Power Supply	HV	LV for FEB	LV for LBB
Hostile Environment	Yes	Yes	Yes
Voltage	12 kV	7 V	4 V
Current	1 mA	3 A	14 A
Programmable Voltage	0-12 kV	0-9 V	0-5 V
Current precision	0.1 μA	100 mA	100 mA
Voltage Precision	< 10 V	100 mV	100 mV
Trip settings	0-100 s	0-10 s	0-10 s

Table 3.4: Required parameters for Endcap RPC's High Voltage and Low Voltage System.

The RECS of the Power System

The RECS power control operation is performed repeatedly through different levels. At the board level (i.e Hardware Level) first safety mechanisms are implemented, to assure safe and fast performance of the hardware. There are some parameters, which are programmable, these are programmed to our needs and then are made to act promptly for each channel in case of a major problem and bring the detector back to safety, for example absolute protection for "over current" and "over-voltage" is available for each HV channel, which makes a particular channel to trip automatically, if in case these parameters exceed their allowed limit, so usually it's value is set such that it is lower than the hardware's protection level. Hardware protection is also available for each LV channel, in this case system contains protection for both digital and analog currents and voltages of LV modules, in this case tripping of the channel depends upon the alarm condition, which gets triggered according to the selected programmable trip time. All other controls are implemented at software level for which backend applications are used.

The Mainframe SY1527 communicates with the CAEN power system via OPC protocol, where OPC stands for "OLE(Object Linking and Embedding) for Process Control", more about OPC can be found at [29], which follows the schema shown in figure 3.14. The PVSS software based applications are distributed over two servers in order to balance or distribute load and to optimise the resources. An event-driven approach is used for the acquisition such that parameters which are of significant importance are handled within a 2s refresh time. In order to enhance the protection for our hardware, software part

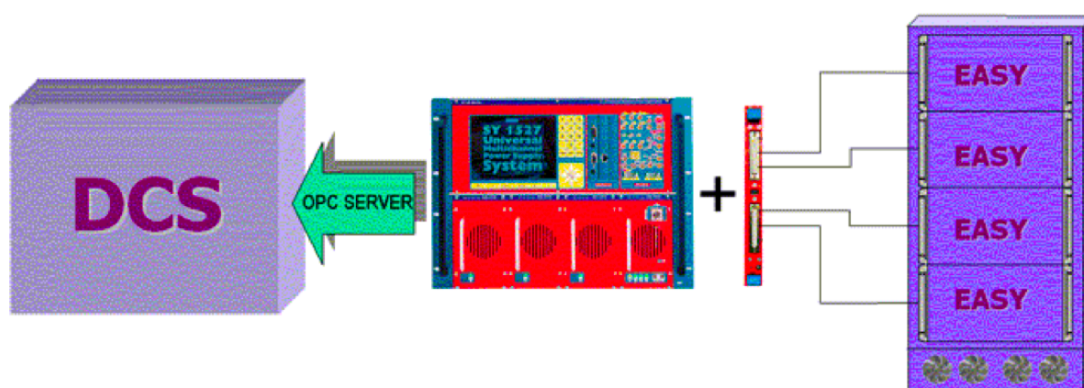


Figure 3.14: The CAEN mainframe communicates with the DCS via OPC and allows us to operate each power channel independently. The detector control system monitors the status of the and sends appropriate commands to the Mainframe.

of control system does the job by means of several safety checks for each HV and LV channel, also to operate the system efficiently it provides a robust and easy interface. Additionally to prevent the hardware from harmful situations, controls are available where we can set the values for alarm conditions and view the status of our equipment. Actions are foreseen to gently ramp down the voltages or to switch off the boards of Low and High Voltage systems to the status conditions which are safe, in case when temperatures rise to high values or when backup system fails. It can handle multiple commands issued by the supervisory DCS application, which are then translated into a right sequence of a single command to ensure safe and correct the detector operation. The RECS also provide an interface between power supply channels and higher level operations of the control system. In addition, a specific GUI is provided to the user, which is a simple interface to monitor the most important parameters like alert status and the behaviour of single channels which are being updated over time 3.11s.

3.2.3 The Environmental Control System

The RPC detector physics parameters such as dark current and noise rate are temperature and humidity sensitive, so performance of RE chambers is related is dependent on the operative humidity and temperature values [30]. In order to maintain the stability and quality of RPC's data taking during the entire lifetime of CMS, an essential requirement is to have network of sensors which are highly granular, robust and homogeneous, also it should be able to provide a complete overview of the RPC's environmental system. In RE system, there are many quantities which should be monitored, like the temperature of the air inside the detector volume, humidity and temperature of gas, cooling pipe's temperature here the sensors place at the exhausts of the pipe, FEB's temperature, and relative humidity of the environment. The type and quantity of the sensors which are installed in RE system is given in table 3.5. Location diagram of temperature sensors installed is shown in figure 3.15. In order to get a complete picture of detector's thermic map, additional temperature probes are also installed at the endcap cooling pipe, at some crucial locations. The relative humidity sensors are installed on some reference RE chambers and also at the gas distribution racks for each disk's input and output. The purpose of these sensors is give early warnings about high humidity conditions, which may potentially lead to the condensation of water inside the detector.

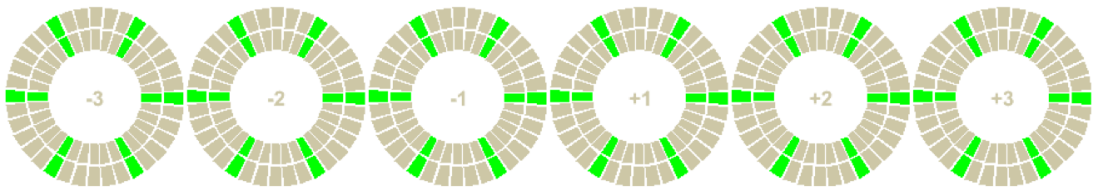


Figure 3.15: In the endcap region, all the stations (green) are equipped with temperature sensors.

The sensors AD592BN and HIH4000 are used to measure temperature and relative humidity respectively. These sensors are magnetic field and radiation tolerant and are bound to assure the reliability, robustness and precision measurement required, details are in table 3.6. We have used CAEN ADC (A3801A) boards to read and power up these sensors it has 128 channels i.e. 128 sensors could be operated by one board, and it's operational voltage is 12 V. All ADC boards required to power up these sensors are located in the same EASY3000 crates which are already being used for Low Voltage

Region	Air Temp.	Env. RH	FEB Temp.	Gas Temp
Endcap Disk +3	12	4	378	4
Endcap Disk +2	12	4	378	4
Endcap Disk +1	12	4	378	4
Endcap Disk -1	12	4	378	4
Endcap Disk -2	12	4	378	4
Endcap Disk -3	12	4	378	4
Endcap Total	72	24	2268	24

Table 3.5: Details of environmental sensors and their physical distributions.

Environmental sensor	Temperature	Humidity
Hostile Environment	Yes	Yes
Input range	$-10^{\circ}C + 6^{\circ}C$	$0 - 100\%RH$
Accuracy	$0.1^{\circ}C$	$\pm 2.5\%RH$

Table 3.6: Endcap RPC's environmental network requirements.

system. Now for the electronics boards inside the chamber, additional sensors were installed to look after the working temperatures and assure the effectiveness and safety of the working condition. The Endcap RPCs are equipped with about 1296 FEBs and on each FEB we have installed one or two temperature sensors (AD7417) whose nominal accuracy is of the order of $0.25^{\circ}C/LSB$.

The DCS of the Environmental Control System

The control and monitoring of the environmental data is read out with a 10s refresh rate via ADCs which are installed in the EASY crates through OPC server in PVSS. Each and every data point is continuously monitored and appropriate actions are promptly taken if temperature value exceed 24 degree and in case of humidity more then 70%, which is beyond the respective safety ranges. Now to monitor and correlate the environmental parameters evolution over time with the other detector operation parameters, the environmental data is also made available in several panels of the GUI (figure 3.16).

The Link Boards are used to read the data from FEBs, using CCU ring through an application called XDAQ, which is then sent via soap messages to PSX/PVSS, as shown in the figure 3.17. A dedicated application of PVSS is responsible to control, gather, and to correlate it and to take necessary actions against each and every information, for example in case of any harmful situation, it turns off the power of the problematic FEB.

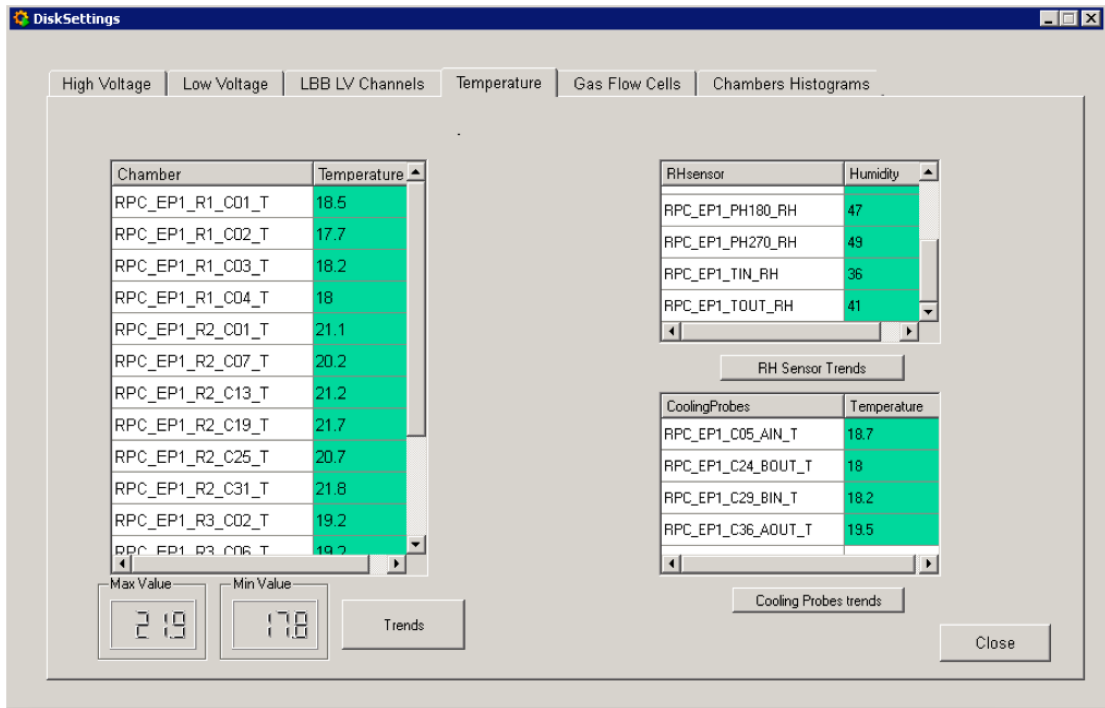


Figure 3.16: GUI for the monitoring of the environmental sensors located at detector region.

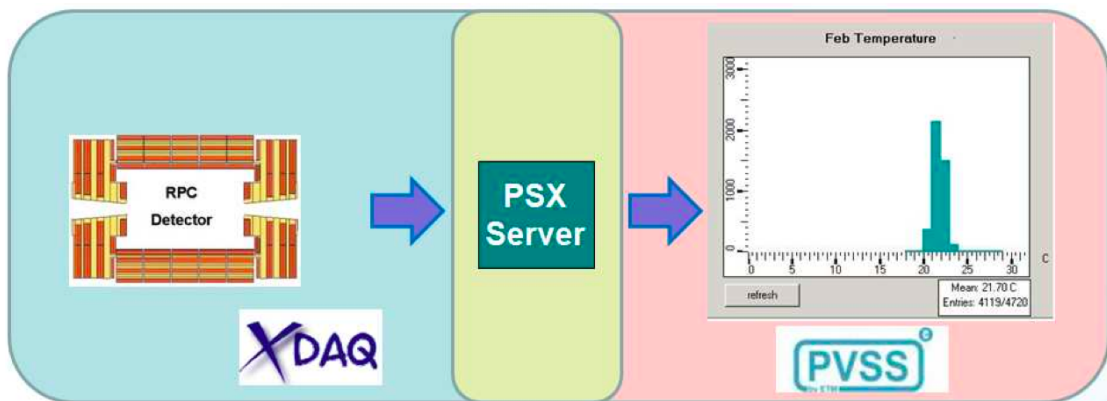


Figure 3.17: FEB temperature data flow block diagram. XDAQ application fetch information the LBs which is then sent to the PVSS application via PSX.

3.2.4 External Control System

There are other control systems which are managed and controlled independently are referred as External Control System, to whom RECS has to interact. These system are designed in a way that they should react if there is a problem, but their status must be notified to the RECS as they may have effect the hardware and DCS may be required to take automatic corrective actions. Such external system are detector safety and cooling systems which will be described next, as they are deeply involved in the RECS operation.

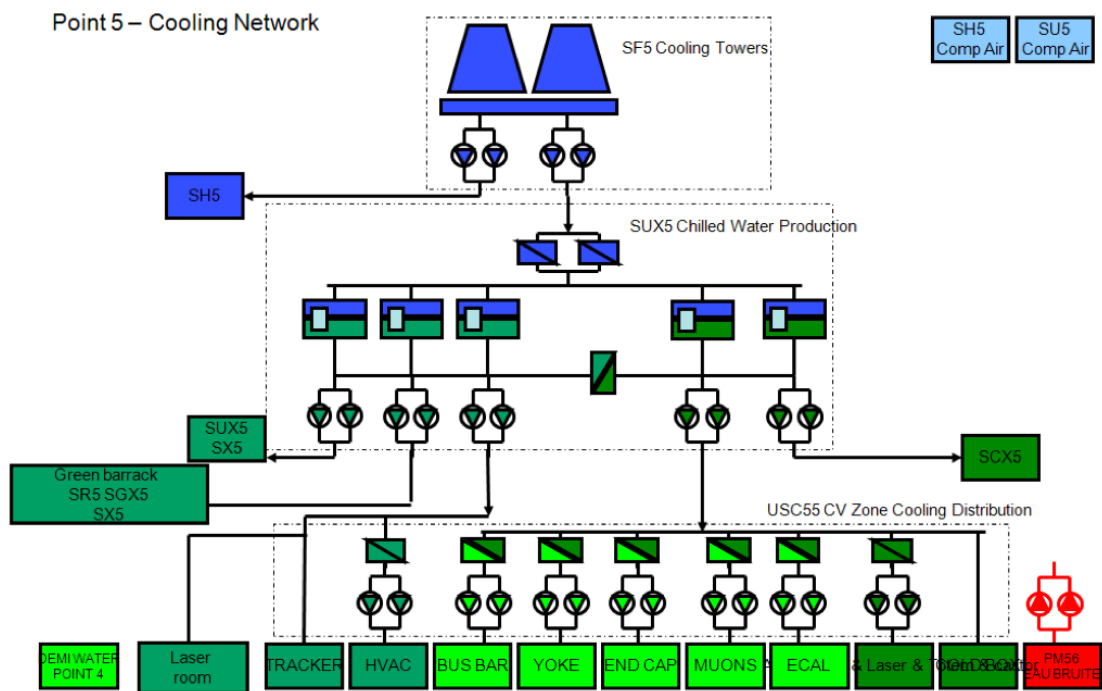


Figure 3.18: CMS cooling system. Cooling of RPC chambers is done by different lines, in order to avoid heat exchange from the other subsystems, in this way the chamber electronics temperature is kept stable.

Cooling

Ventilation and cooling is an infrastructure service provided by CERN for all the LHC experiments, because an efficient cooling system is very important requirement for any detector for it's healthy and efficient operation. As temperature effects the safety, lifetime of electronics, stability of the mechanical structure and the the response of the detecting elements of the detector.

When all the sub detectors of CMS are in operation, about 800 kW heat is dissipated

in the CMS experimental cavern. This heat is felt with the interception of C_6F_{14} coolant for tracking detectors and water at $18^\circ C$ is used as coolant for Muon and Calorimeter detectors. CMS cooling plan is described in figure 3.18. Also cooling system should maintain safe temperatures for equipments like DAQ server network and rack system. In addition, at several point of the distribution chain, the Detector Safety System monitors very important parameters such as dew point, temperature, flow rate and loss of coolant. This detailed overview or information is used by RECS in order to take proactive and automatic actions on hardware involved in case of problems.

Detector Safety System

As described above the Detector Safety System (DSS) [31] works in cooperation with the RECS to ensure the safety of the experimental area. They together take care of the experimental equipment in case of major hazards, like fire, smoke, oxygen deficiency etc. RECS alone cannot ensure protection against this kind of harmful conditions, of its high granularity and complexity. The Detector Safety System is specially designed for these tasks, it is reliable and consequently its actions are very fast and quite coarse, for example if smoke is detected, the power of the entire cavern is switched off immediately, this action will thus disrupt the data taking process of the detectors, but will prevent the severe damage of experimental equipments, also time required to repair the equipments will be saved. The DSS sends all alarms RECS which are used to execute predefined control procedures. In some harmful conditions where RPCs are needed to be shut down, fast action is not required as fast shutdown is harmful for the RPCs, DSS action is executed with a few minutes delay to allow RPCs to shutdown gently before the DSS switches off all the equipments. The front-end consists of an array of two PLCs which interpret the signals according to a programmable alarm action matrix coming from the sensors. The PLCs are there to scan all input channels, process the alarm-action matrix and modify the state of the outputs according to the situation. This cycle takes about 500 ms to complete, so DSS reacts to any hazardous situation in less than one second, which the response time of DSS.

3.2.5 Supervisor

All the control subsystem i.e High Voltage, Low Voltage, Gas etc. operate as standalone component of RECS and participate in complete RE system operation, thus each component performs it's particular task. Supervisor application is the master application

of the RECS. It collects the head nodes of the RE subsystem applications and organises them within its own FSM tree. This enables a single person using the supervisor panel (see figure 3.19) to have an excellent overview of the state and important variables of the RE system. A single person also can perform simple actions with a few mouse clicks to bring the endcap RPC into the desired state. The Supervisor also implements methods for automatic actions, such as soft shutdowns to protect the detector and to avoid the need for safety actions. Soft means that the RE system is smoothly ramped down instead of a hard power cut. Automatic shutdowns were implemented to help the operators in critical situations and it also eliminates the need for many hard shutdowns, which protects the hardware. RECS is based on JCOP+PVSS software, i.e it uses the functions and facilities provided by the JCOP+PVSS software, such as alarm handler, GUI, FSM and ORACLE database. The ORACLE database allows us to load hardware hierarchical configuration from the configuration database of CMS, also archived data can be stored in CMS online database.

The End-Cap RPC Supervisor is connected to a RPC Supervisor, The RPC Supervisor is connected to a higher instance, the so called Central DCS. The Supervisor reports the state of its top FSM node and accepts basic control commands like ON, OFF and STANDBY.

RECS Architecture

System being highly granular and plenty of components under the RECS control, demands the description in a hierarchical way. So the architecture of RECS is based on hierarchical tree structure. The hardware distribution tree as well as its geographical location can be seen in figure 3.20. RECS tree gives useful information of the system from two different point of views. The geographical tree view, gives the location of the each sub detector and its components. While the hardware tree view, gives the status of each hardware component involved in the operation, which is very useful to figure out and address the problems which occur in a particular component of hardware. This particular subdivision enfolds the geometry of the RE system, i.e. discs and rings of the RE system, which allows a close correlation with readout data. Given structure can easily be implemented by using PVSS and JCOP framework. This framework with the help of Logical and Control Unit, both objects have different privileges so they perform different tasks, such that they take care of the behaviour of hardware equipments and subsystems which they control and hence describe every tree node. So these units can

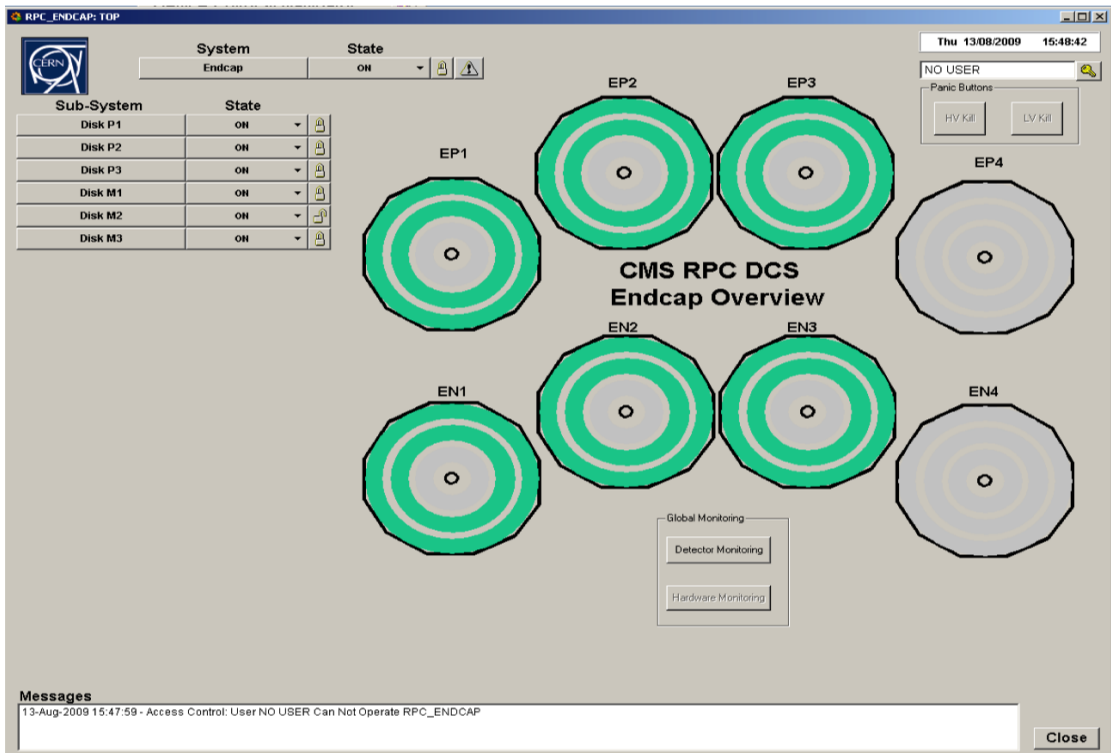


Figure 3.19: The Supervisor Panel

in-fact they can control, configure and monitor all the child nodes and can rescue them from error state. Thus scalability and partitionability of the system is assured, which makes the management of the system powerful and robust. Like leaves of the trees, we have different logical groups which describe our hardware devices like Low Voltage front-end, Low Voltage Link Board, Low Voltage power supply, High Voltage power supply, environmental systems etc. These electronic channels called tree nodes in PVSS, are represented by Device Units (DUs). There are many DUs in RE system, where each DU provides an interface to the hardware component, it received and translates commands, understands the states of the device and if required it generates eventual alarms. Through dedicated channels, EASY crates, power supplies, high and low voltage channels are separately managed. The top node of the RPC DCS which consists of both BARREL and ENDCAP DCS, is directly connected to the central DCS of CMS experiment, to establish communication with each other and exchange commands, actions and states. The central DCS commands are sent via RPC Endcap FSM tree, downwards to the devices, these commands are interpreted as hardware commands. Only vertical data flow is allowed in the hierarchical tree structure, commands propagate downwards, while change in state status and alarms move upwards (figure 3.21).

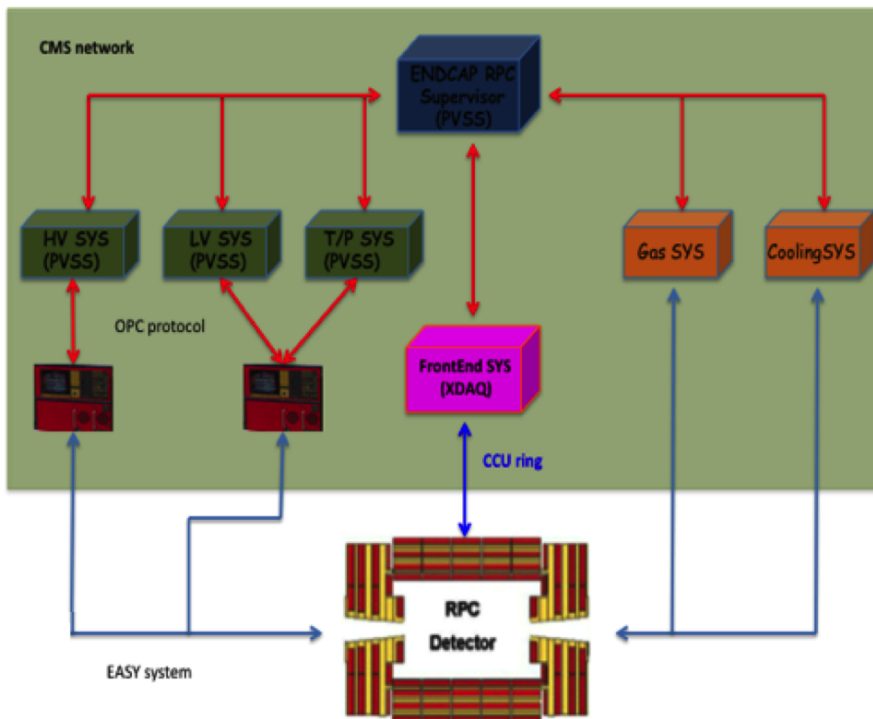


Figure 3.20: The CMS Endcap RPC detector control system layout

FSM

All RECS nodes are put into action via Final State Machine (FSM), in order to reduce repetitive action, human errors, attain automatic control of the processes and optimise recovery procedures in case of unwanted states. The FSM is a collection of logical RE system high-level objects, which can be organised in a tree structure. The components are called nodes. Nodes can be connected to other nodes or to a so called device unit, which represents real hardware. Each node has a state, which is determined by pre-defined rules. The parent nodes summarise the states of all their children. The safe, easy and powerful way to get full control of the detector, is attained through FSM by defining a finite number of states, their transitions, and corresponding actions. The FSM toolkit in PVSS is provided by the JCOP framework and is based on SMI++ [32]. So complete hardware hierarchy can be mapped to the FSM nodes and object-oriented approach is used to correctly operate them, also the programmable behaviour of the FSM units are defined in FSM object types. One can separate Individual SMI domains the control hierarchy If there is a need to operate different detector parts independently. If there is a need not to propagate state or receive commands, device-oriented FSM objects can be detached from the tree ("Disabled"). The FSM also has a detector oriented hierarchy

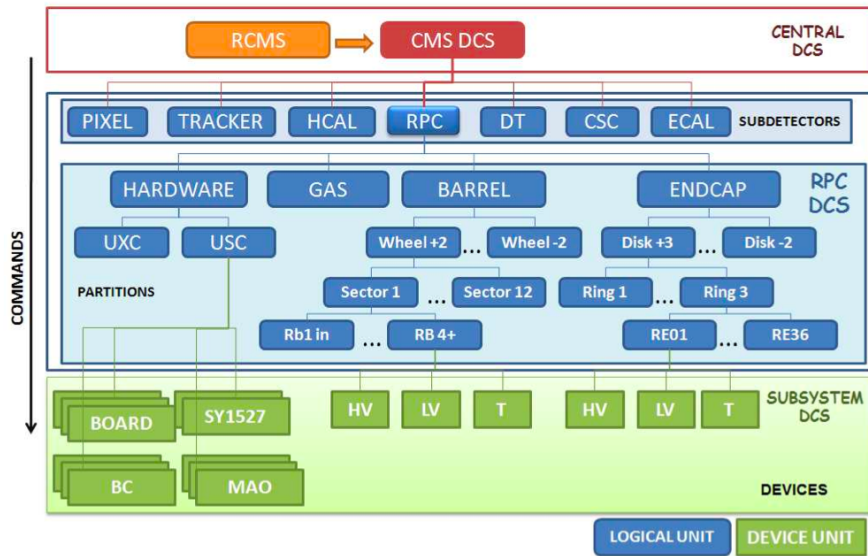


Figure 3.21: RECS hierarchy tree can be seen. As shown commands propagate downwards in the hierarchy, while error messages and other informations are propagated upwards.

which can host more than 2000 FSM elements interlinked, thus ensuring a safe and automatic detector operation.

In order to maintain a uniform structure, CMS has chosen the commands and states setup for top and conjunction nodes. These states are, ERROR, STANDBY, OFF and ON and the commands are, STANDBY, OFF and ON. The compatibility and uniformity is maintained with the central DCS through these particular commands and states, hence permitting adequate transitions between the states. A device state model defined for a HV channel is shown in figure 3.22, all possible configurations of each channel are expressed as states and there are predefined set of instructions which assure reliability and correctness of operations like transition from one state to another. FSM pick data point values and alarm settings from database. Instructions from central DCS are translated in meaningful states for RE system, like a transitional state which is called RAMPING is added to the set of states described earlier. RAMPING is a situation when high voltage of one or more chambers is raised up or down slowly, whereas STANDBY is a state, in which the low voltage channels are ON, while the high voltages are at some intermediate value which is considered safe. During calibration and test runs, in which we have magnet ramping conditions and unstable beam, RE system is kept in STANDBY state to ensure safety.

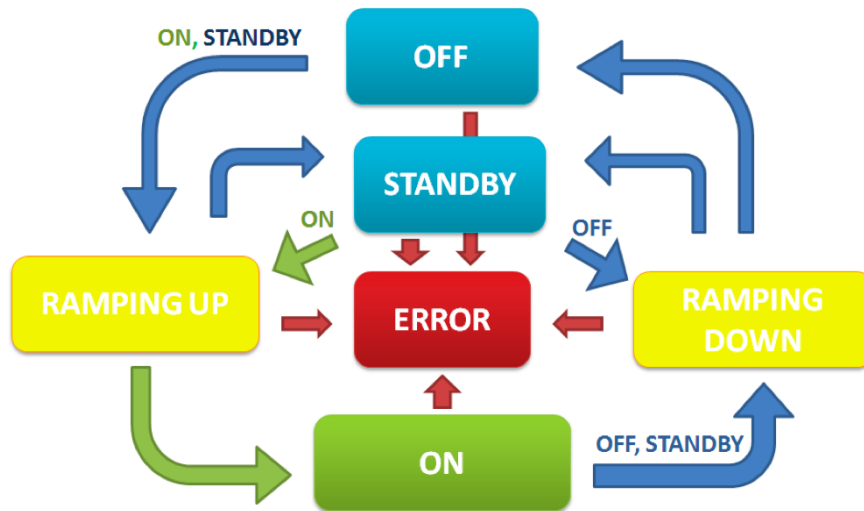


Figure 3.22: For HV channels, device state model is shown.

The Graphical User Interface (GUI)

For control and monitoring of any detector Graphical User Interface proved to be an intuitive tool, as it is easy to use for non-experts and it helps and guides the user to protect the system from dangerous situations. GUI is a collection of PVSS panels, which has the following functionalities:

- easy navigation throughout the entire system structure, thanks to a combination of text, graphical objects and synoptic diagrams
- visualisation and setting of any process variable
- global parameter setting, thus speeding operations and reducing human errors
- plots, diagrams, histograms, and tables for a first online analysis of the detector behaviour
- complete visualisation of the alarm condition on all critical elements.

RPC Barrel group designed approximately 40 panels in a tree structure for the entire RPC DCS which consists of Barrel and Endcap RPC system. The colour codes and name conventions were proposed and decided centrally by the CMS DCS group. RECS panels as an example are shown in figure 3.23. GUI provides us colour-coded states for different data sources and the values of the different parameters are displayed in the panels. The GUI gives us a privilege to set different access levels to prevent the system

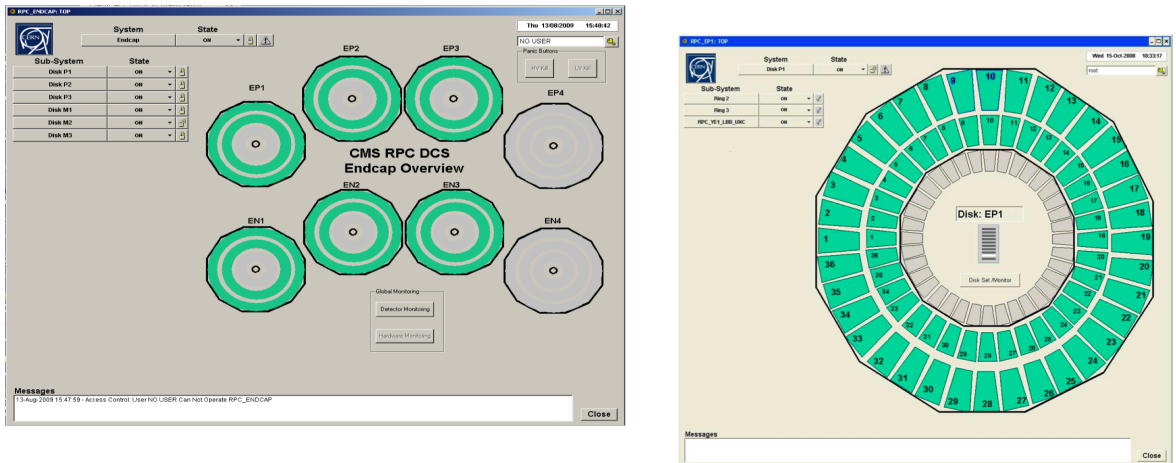


Figure 3.23: Typical layout of the Supervisor system. Left image shows Endcap’s main Supervisor panel. All the objects are coloured according the status of the chamber. Right image shows an Endcap Disk panel. By clicking on each chamber, it is possible to obtain more information about the status of services and their behaviour over time.

from human error, hence provides a complete control upon the entire RE system. Within RECS, Access Control restricts the access of control interfaces only to the authorised users, also access of some actions is restricted to the normal user which require expert supervision to avoid unsafe operation of RECS on the system. The access levels of RECS controls privilege is divided into self-explanatory groups: RPC user, RPC expert and PVSS expert, these groups have been successfully tested during our pilot runs.

Archiving

Archiving is one of the key features of PVSS. It handles archiving to files in its own custom format or to a DBS(Database System) via ODBC(Open Database Connectivity). The DBS chosen for CMS and RPC is the ORACLE DBS. PVSS provides different archiving methods. Two of them are archive on time and archive on change. The first one filters according to a fixed time interval and writes the next incoming value to the DB, while the second method writes the data on every change. The latter may not be a good solution, when the values are changing very quickly. Like this the load on the DB and the growth rate of the DB will be too high. To avoid this, one can define a relative or absolute dead-band on the values. These "deadband" for all relevant parameters are given in table 3.7.

In the case of a network interruption PVSS is able to cache the data to be archived and then write it out to the DB when the connection is back. The DBS of CMS is hosted on a distributed cluster which is shown in detail on figure 3.24. The setup as a

Parameters	DeadBand
Dark current	$5 \mu A$
HV	$10 V$
LV	$0.1 A$
LV current	$0.2 A$
$T_{chamber}$	$0.3 ^\circ C$
$T_{cooling}$	$0.3 ^\circ C$
Chamber Lines gas Flow	$0.5 l/h$
Relative humidity	5%

Table 3.7: Deadbands used to store the values in the online database for the most important parameters.

cluster enables the DBS to scale with increasing performance and storage space needs. It also utilises redundancy to minimise possible downtimes due to hardware and software failures.

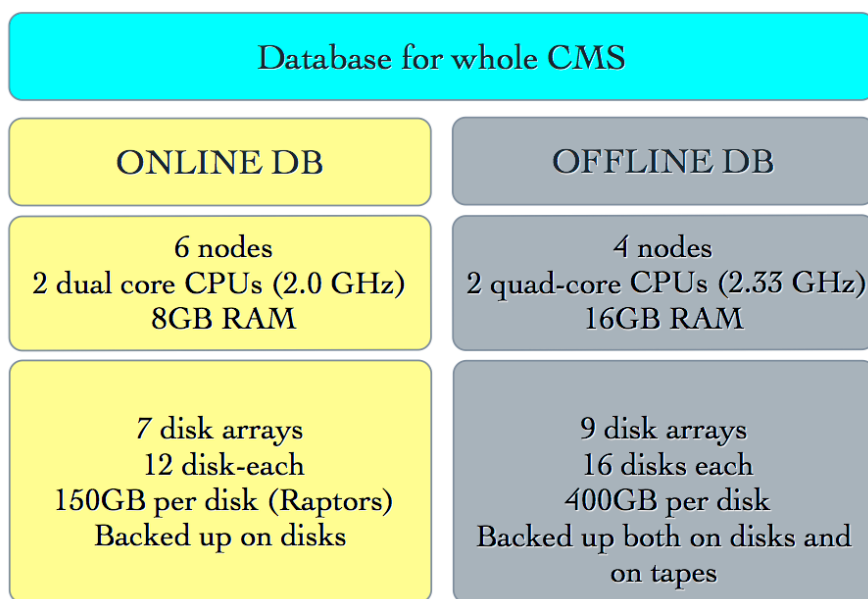


Figure 3.24: The DBS setup provided for the whole CMS experiment.

Authentication and Authorization

The authentication component has been developed and is maintained as part of JCOP. Authentication is embedded in all FSM panels by default in the upper right corner (see figure 3.23). It can be configured to communicate with a central access control server, which runs a PVSS project with the Access Control component. The used authorisation

system is role based. A role is a group and access privileges are granted according to the users group memberships. The definition of roles, groups as well as the group memberships is defined on the Access Control server. One has to take care on the application side to protect certain feature sets by defining the required access privileges. While the Access Control server takes care of the user authentication, the final check if the logged in user has sufficient privileges to see and interact with certain User Interface elements is done inside the User Interface. It is possible to define separate roles for panels and FSM actions. The Access Control server is synchronised with the CERN directory server, which hosts CERN user credentials. Accordingly the user doesn't need to take care of another account, and the administration of user accounts can be done in a central place. The overall communication structure of DCS authentication system is outlined in figure 3.25. The application requires the user to authenticate him, to provide certain features. The set of features provided is role based. Roles are granted to users depending on their group memberships. The access rights organisation is done on the Access Control server, which has been developed by JCOP. Users don't need an additional password for their Access Control account, because their credentials are synchronised with the central CERN authentication services.

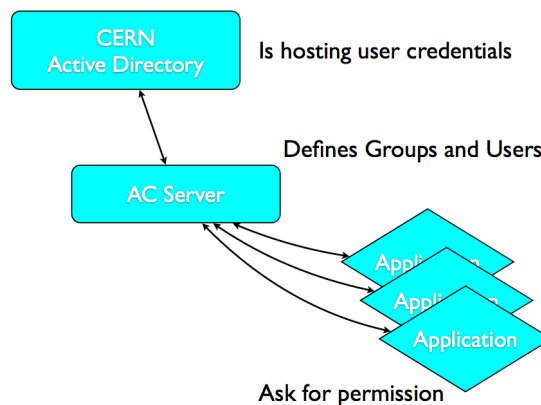


Figure 3.25: Communication structure of the DCS authentication framework.

Alarm Handling

Proper alarm handling in CMS DCS is a must to maintain the detector. On the lowest level one can define alerts on values inside a Data Point, which will further be monitored by the PVSS alarm handling system. Before an alarm on this value can be triggered one has to define the alarm thresholds and the alarm messages (see figure 3.26). Alarms that are triggered and not caught for further processing will be visible in the alert screen.

This method could generate a lot of redundant alarms i.e. in case of a cooling failure the alert screen will be flooded with alarm messages from all SMs and other systems. The overview on the alert screen would no longer be given, which would render it useless. To avoid this situation one can catch alarms and group them in so called summary alarms, which will then be displayed as one line on the alert screen instead of several dozen lines. In addition to that one can also map the low level alerts to a second CMS specific alert processing module, which is able to generate emails and SMS.

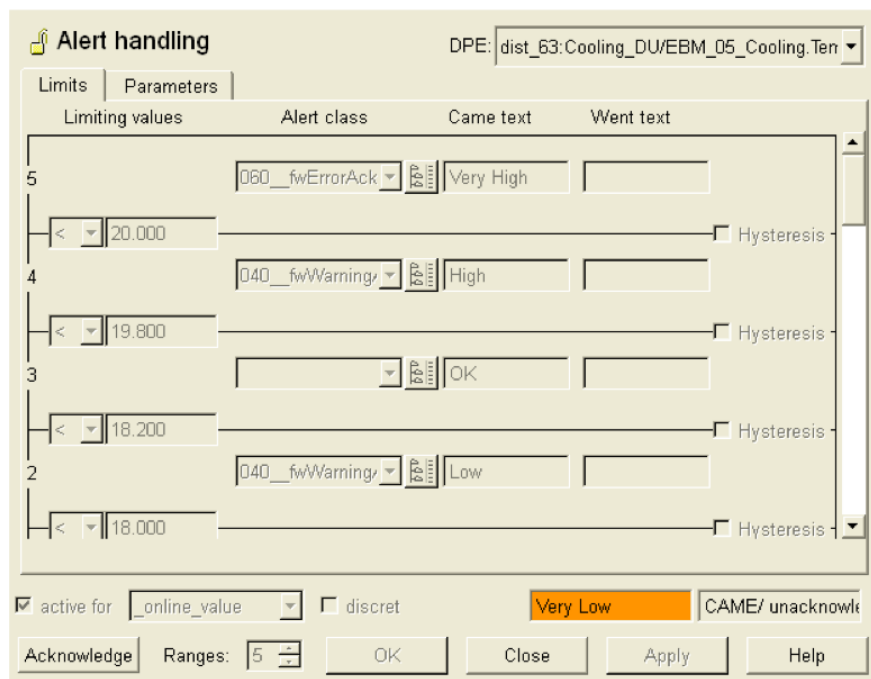


Figure 3.26: PVSS Alarm handling panel. Here one defines different thresholds and the alarm message.

3.3 CMS data taking and Role of Endcap DCS

For CMS to become a reliable, unique and highly efficient machine, several milestones were reached during the development of RECS. Since summer 2006, with and without all the sub detectors, many campaigns of global data taking took place. Integration of RE system was done, while learning the ways, as how to operate simultaneously with all CMS sub detectors, DAQ chains and trigger system as a unique system. At the end of the day it turned out to be a very useful period for the commissioning of all sub detectors as well as for the data analysis structure. Also commissioning and integration of trigger and data acquisition systems, data quality monitoring and detector control system was

performed. In addition testing of the full data handling was also performed.

During August-November 2006, in the surface hall of Point 5, the first global commissioning was performed. The entire experiment was placed at the surface assembly building during a campaign, called the MTCC (Magnet Test and Cosmic Challenge) [33]. The solenoid magnet was fully tested along with a vertical slice of most important detector components i.e barrel and endcap muon chambers, HCAL, ECAL and silicon tracking system, were operated at the same time, and with and with-out the magnetic field, cosmic data was recorded as a signal. After MTCC, CMS was defended part by part into the experimental cavern. After that data taking efforts started in a row, which was named as "Global Runs" and local commissioning activities were completed by individual detector groups. During 2007, with the partially opened detector, more than 300

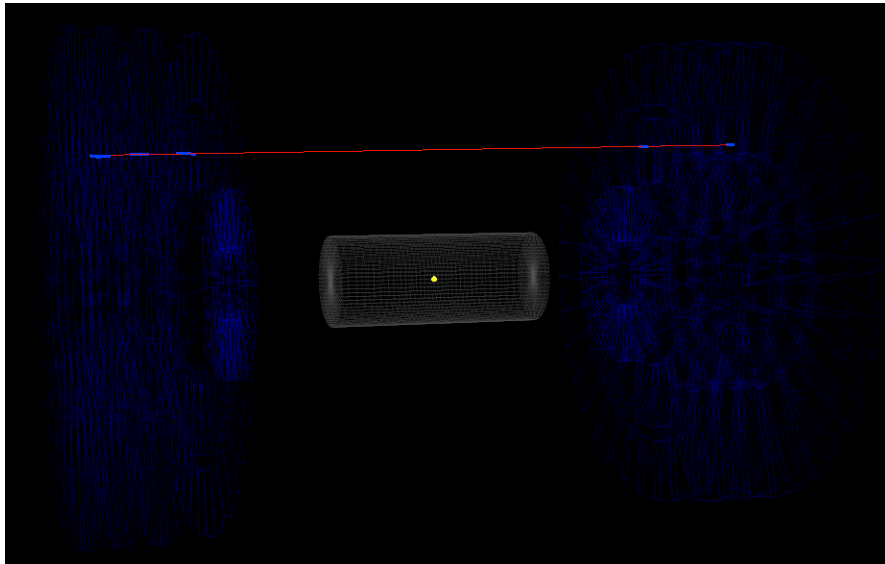


Figure 3.27: Event display of a nice beam halo event from CMS(26-Nov-2009).

million cosmic ray events without magnetic field were recorded. Then in 2008 August, the machine was ready to take data and protons started to circulate in LHC tunnel in September of the same year. So during first beam days, many types of events got collected such as "beam halo" and "beam splashes". Beam halo events consists mostly of muons travelling parallel to the axis of proton beam, useful for the commissioning of forward detectors and in beam splashes, a single beam of 2×10^9 protons are dumped into the closed collimators, 150 meters upstream, hence delivering large energy deposits in the calorimeters. On September 19th, LHC's beam pipe accident took place due to which, real data was not available. Then at nominal magnetic field long cosmic run was

taken, which was named as "CRAFT" (Cosmic Run At Four Tesla). So at magnetic field of 3.8 T, 290 million events were recorded during CRAFT, out of which 3% events had muon tracks with tracker hits, 30000 events had pixel hits and 87% events with muon track in the muon chambers. An event display of a nice beam halo event going through entire endcap RPC system is shown in Figure 3.27.

3.3.1 Performance of RE DCS

The RECS was tested extensively during the periods of global data taking as well during hardware installation phase. We had a short debug phase, after that RECS worked without any problems during entire testing period and it showed that the architecture of the RECS met the requirements all the requirements like scalability, speed and configurability. The RE DCS was proved to be a most reliable tool for correct and safe operation of the RE detectors. Trained RPC shifters safely and easily operated the detector. In case of any interruption which can occur due to communication problem with the power supplies and power failures RECS proved to be the best in tackling such interruptions, and kept the RE detector safe. Also the with the help of developed FSM RECS properly monitored the detector's behaviour and it never lost control of hardware connected to it.

The RE power control and communication performances can be described in terms of its properties like percentage of commands transmitted and lost, and switching on/off speed. From the software's perspective, the entire RE system consists of more than 10000 parameters. These parameters are acquired from RE hardware at the rate of 100 Mb/hour. The OPC protocol [29] communicates with the CAEN power system, to optimise the resources. Now in order to balance the load, software applications are distributed over two servers. The "CAEN OPC server", version 3.0, serves the purpose, while an event-driven approach is used for the acquisition. For several different settings and refresh speeds, extensive studies have been performed to improve the performance of RECS in term of powering of the system and manage network load. As a result we managed to identify the bottlenecks in the system, so the work load was distributed smartly among different groups of OPC Client, such that average load per pc was left about 5000 items. Most significant parameters were handled with a refresh time of 2s. Extensive studies were done on timing performance, using this OPC server/client configuration and with increased number of hardware channels, which gave an effective and reasonable results in setting and switching of the states of the system (figure. 3.28).

So due to the detector mode operation, the time elapsed to switch on the detector was calculated to be 470 s. Now for database performances, the communication with

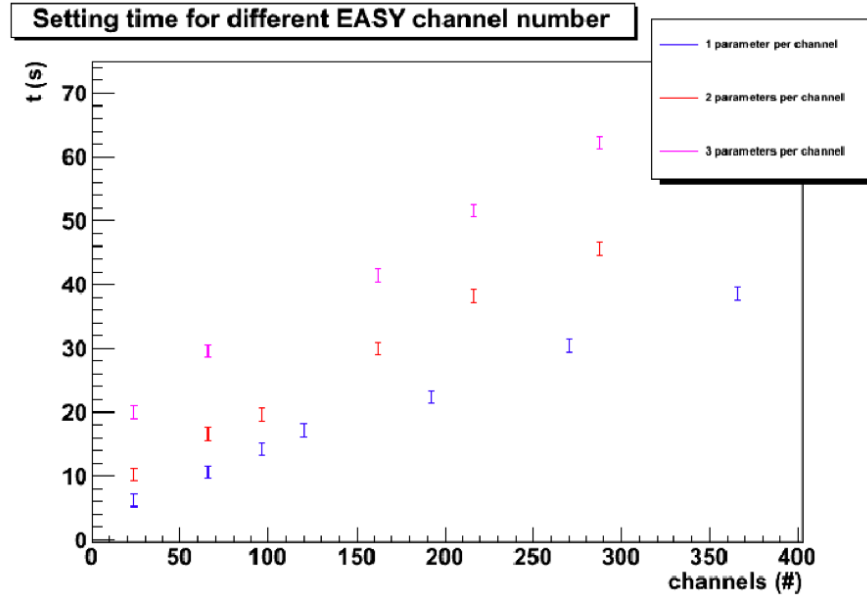


Figure 3.28: Plot shows the effect on time spent, to set different parameters, due to the increment in the number of CAEN channels. This configuration shows the maximum loads that can be configured per SY1527 in our configuration.

databases stood reliable and stable throughout. In about 70 seconds, configuration data from database is acquired and transmitted to the hardware, depending on the database load. With optimised deadband, less than 0.3% of data lost in one year, therefore the communication with the condition database stood stable with high efficiency storage. The condition data of about 4 *GBytes* was collected and stored in the CMS condition database at the rate of 30 *Mbytes/day*, hence for optimised deadband, a pre-scale factor of about 400 respect to data was acquired.

Performance of Power System

The power system behaviour is a key requirement to understand the detector response. All the components were individually tested during the development phase of RECS, to optimise the performance of each element of power distribution network, for example, cables, power supplies and connectors. The said exercise was performed to stabilise the response of dark current and effects from external sources. As far as power supply is concerned, during the commissioning phase many actions were taken to improve read-out, power distribution network-grounding schema and stability of the power supplies. After

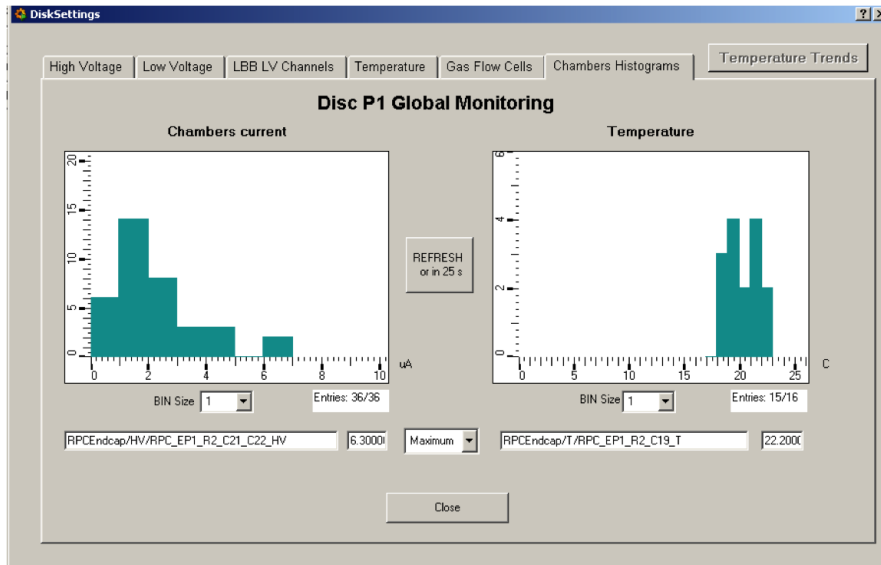


Figure 3.29: Global Monitoring panel, showing chamber currents(left plot) and temperatures(right plot).

a long and tiring testing and optimisation phase, stable version of high voltage board was obtained due to the efforts of CAEN engineers along with my colleague Giovanni Polese, which then met requirements of RPCs in term of reliability, accuracy and offset stability in multiple operative conditions. As discussed previously, measured current only depends upon the chamber's behaviour, also environmental condition's variation have a direct affect chambers current. During global runs the detector response in terms of dark current matched the requirements of CMS experiment. In the panel shown in figure 3.29, left plot is dark current summary of 36 end cap chambers at 9.2 kV, and average current value vs time is shown in the panel of figure 3.30 for 18 chambers, As can be seen the average remained almost stable i.e. around $1.5 \mu A$, value exceeded $3 \mu A$ for very few chambers. There was no special correlation with the variation of temperature in the range which was explored, at least on the mean values. Stability of low voltage stability was achieved, with a quite acceptable ripple level of about 50-100 mV, due to which safe operation of FEBs was ensured and external noise was minimised. Since summer 2007, power system of RE system is working in it's final configuration without any interruption, with less then 5% failure rate and all the repares were done without any delay in the operation of entire system.

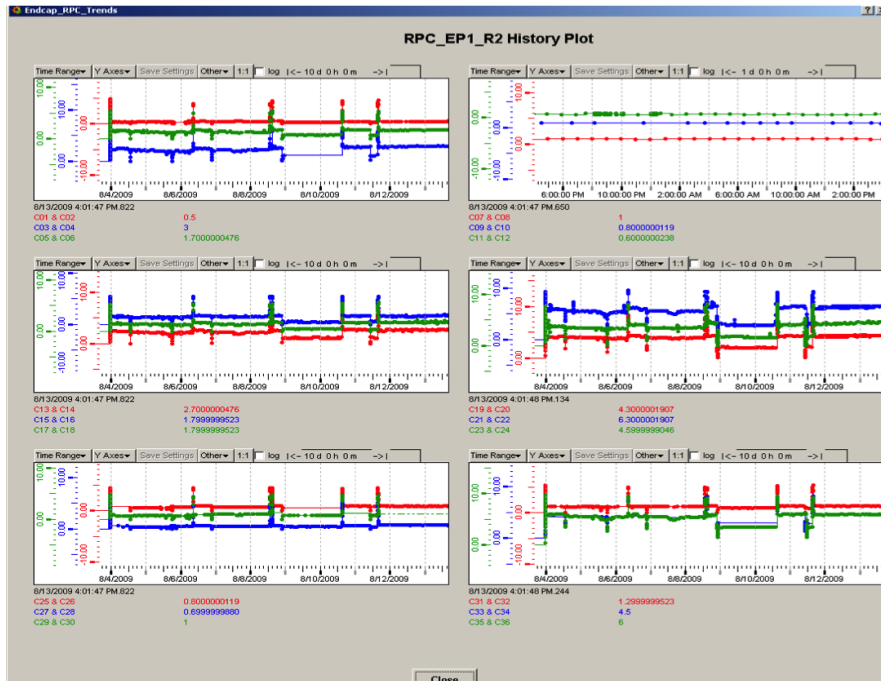


Figure 3.30: current vs time history plots for 18 chambers.

Performance of Temperature System

The temperature variations strongly effect the stability and performance of detector's mechanical structure, the safety and lifetime of electronics and safety as well as response of the detecting elements. There is a correlation between the cooling system stability and efficiency, and global chamber operational temperature. To check the effect of environmental conditions on all the subsystems, several tests on the thermal environmental map were performed during the commissioning phase and we managed to spot hottest regions due to specific hardware configurations. A good general operation stability was found on evaluation of cooling system. In order to increase the cooling circuit capability, special efforts were done during the shut down period, hence obtained satisfactory and stable working situation where all the chambers were kept below safety detector-working threshold. The dependence of chamber's electronics temperature verses cooling temperature on a reference chamber is shown in figure 3.31. Also relative humidity of a disk and temperature distribution of the same disk during long period of data taking is represented in figure 3.32. The system temperature remained stable but clear variation is seen when all the electronics of CMS detector was switched on or off.

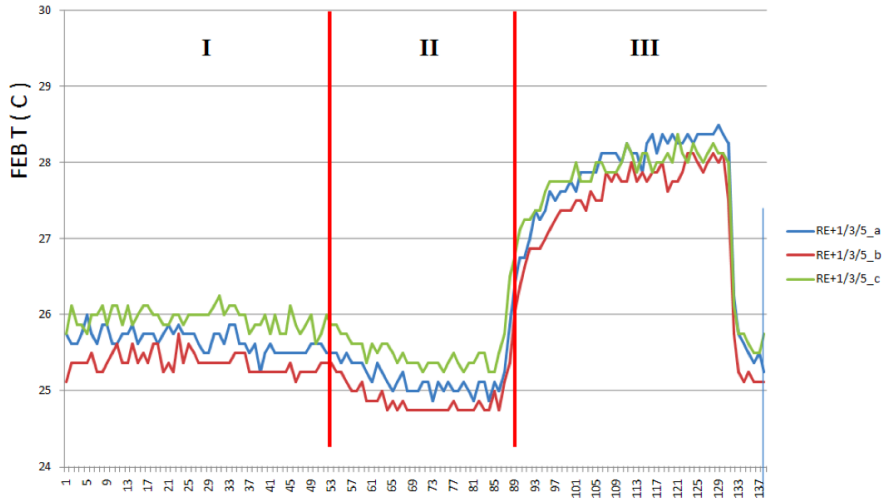


Figure 3.31: FEB temperature depends upon coolant temperature results from some installed chambers. In the region I water temperature is at 20°C which is stable working condition. In region II water temperature was decreased to 19°C . In region III no cooling.

3.4 Conclusion

This part of the thesis focuses on control and monitoring of power and environmental systems, which are actively involved in the operation of Endcap RPC detector. The development requires deep knowledge of RPC detector and its different subsystems such as front end electronic, readout, environmental conditions and detector itself, and understanding of their behaviour during the different working phases of operation. Different technologies, middleware and solutions has been studied and adopted to develop different components. Of course, big challenge was to integration these parts which are different from each other and in the general CMS control system and data acquisition framework. I have been following this project since November 2008, as responsible for the CMS ENDCAP RPC Group, during operative phases and now a stable version of the system is operative and being used by the RPC collaboration.

The aim of RPC Endcap DCS (RECS) is to assure a continuous monitoring and control of the detector, the trigger and all the assisting sub-systems which are low voltage, high voltage, gas, cooling and environmental system, which is very essential to gain operational reliability and stability of a very big and complex detector and its trigger system. It also takes appropriate corrective actions to maintain the detector stability and ensure high quality data, it also provides user interfaces in the form of panels, which are equally useful for experts, as well as for shifters. The working environment at the same

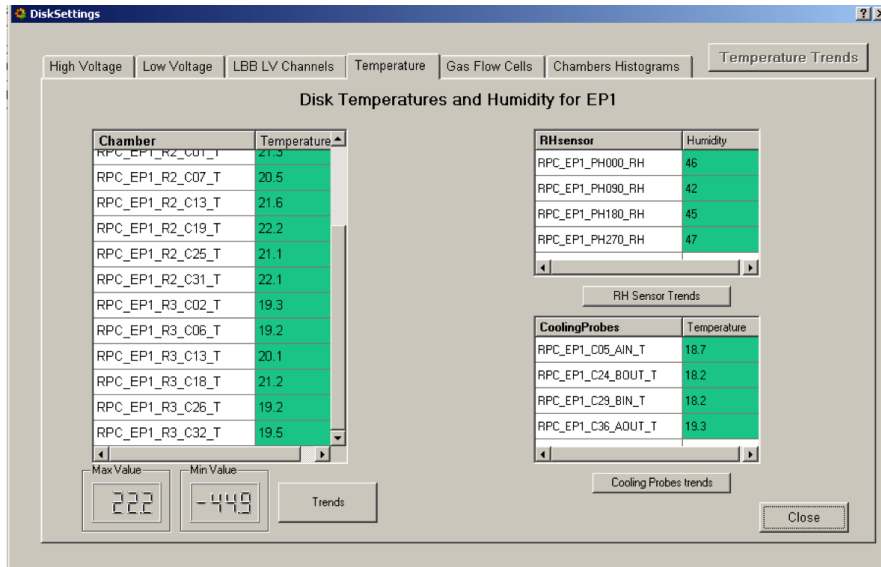


Figure 3.32: Disc temperature and humidity panel

time create challenging situation for the control system because of high magnetic fields and high-radiation environment. Therefore, the control system must be fault-tolerant and allow remote diagnostics. As plenty of functions of the RECS are needed at all time, so such solutions and technologies were adopted which must ensure 24/7 functioning of the system for the entire life of the experiment. The RECS is operative since summer 2007 and running on a small farm of 2 PCs inside building 40, later it was successfully integrated in the central CMS DCS during the winter of 2008/2009. The entire project proved to respect all the CMS DCS guidelines.

The commissioning run was also used as system benchmarks and the DCS performance matched the challenging requirements as reported. The calibration procedures were tested in the CMS environment and the performances fulfilled the requirements. The behaviour of RECS been studied and analysed during running in phase, under normal stable operational conditions as well as under abnormal and critical phases such as magnet ramping, start-up, power outage, beam filling etc. to identify bottlenecks or weak parts of the system. Furthermore, in order to obtain the best detector response, the RECS allowed us to study the detector performance and to adjust the detector operation parameters. In this part of the thesis I have tried to explain of the RECS for CMS experiment, because of the complexity of the experiment and the large diversity of components was utilised. The commissioning and validation of the RPC detector control system are now finished and it is currently running in the operational phase. The

work presented here has contributed to the commissioning of the RPC detector and its calibration.

Chapter 4

The Top Quark : The "King" of Fermions

Among all particles of Standard Model, top quark is by far the most massive with a current world average mass of $173.20 \pm 0.87 \text{ GeV}$ [34]. To produce a heavy quark like the top quark, a hadron collider needs to reach a multi-TeV centre-of-mass energy. The first collider that was able to produce them is the Tevatron $p\bar{p}$ collider located at Fermilab nearby Chicago. At this collider, the top quark was discovered in 1995 by the CDF [35] and $D\bar{0}$ [36] collaborations more than 20 years after the discovery of the bottom quark. Hence, the Large Hadron Collider is the second machine that can produce this heavy quark and the first that will do so in large numbers. This opens a wide area of top quark research at LHC.

4.1 Top Quark in the Standard Model

The basic building blocks of matter, the fermions in the Standard Model, are represented in the Table 4.1.

Three generations of leptons and quarks exist within Standard Model, having physical properties identical with respect to the several quantum numbers, but differentiating in their masses. For each generation exist a pair of quarks and lepton, the left-handed quarks form weak isospin doublets with positive fractional charge $Q = +\frac{2}{3}$ with weak isospin $I_3 = +\frac{1}{2}$ while the the negative charged quarks $Q = -\frac{1}{3}$ have a negative weak isospin $I_3 = -\frac{1}{2}$. The $I_3 = -\frac{1}{2}$ isospin of the bottom quark implies the existence of an additional quark, the top quark, as the third-generation weak isospin partner of the bottom quark. Furthermore, the existence of such third generation quark doublet, in presence of the three lepton generations, ensures the necessary cancellations in diagrams

1^{ST} GEN	2^{ND} GEN	3^{RD} GEN	I_3	Y	$Q = I_3 + Y/2$	Mass
QUARKS						
$\begin{pmatrix} u \\ d \end{pmatrix}_L$	$\begin{pmatrix} c \\ s \end{pmatrix}_L$	$\begin{pmatrix} t \\ b \end{pmatrix}_L$	$+\frac{1}{2}$ $-\frac{1}{2}$	$+\frac{1}{3}$ $-\frac{1}{3}$	$+\frac{2}{3}$ $-\frac{1}{3}$	$u = 1.5 - 3.3 MeV/c^2$ $d = 3.5 - 6.0 MeV/c^2$
u_R	c_R	t_R	0	$+\frac{4}{3}$	$+\frac{2}{3}$	$c = 1.25 \pm 0.025 GeV/c^2$ $s = 95 \pm 5 MeV/c^2$
d_R	s_R	b_R	0	$-\frac{2}{3}$	$-\frac{1}{3}$	$t = 173.21 \pm 0.51 \pm 0.71 GeV/c^2$ $b = 4.66 \pm 0.03 GeV/c^2$
LEPTONS						
$\begin{pmatrix} \nu_e \\ e \end{pmatrix}_L$	$\begin{pmatrix} \nu_\mu \\ \mu \end{pmatrix}_L$	$\begin{pmatrix} \nu_\tau \\ \tau \end{pmatrix}_L$	$+\frac{1}{2}$ $-\frac{1}{2}$	-1 -1	0 -1	$e = 510.9989 KeV/c^2$ $\mu = 105.658 MeV/c^2$
e_R	μ_R	τ_R	0	-1	-1	$\tau = 1776.82 \pm 0.16 MeV/c^2$ $\nu < 2eV/c^2$

Table 4.1: Leptons and quarks - the building blocks of the matter (according to the Standard Model). Weak isopin (I_3), hypercharge (Y) and electric charge assignments are respectively shown in the fourth, fifth and sixth columns. The last column lists the masses of the fermions according to [37].

contributing to triangle anomalies. Measurements of the Z^0 width at the LEP and SLC colliders rule out the existence of a 4^{th} generation neutrino with mass $M_\nu \lesssim M_{Z^0}/2$ [38]. Unless the 4^{th} generation neutrino is very massive, no additional generations are allowed in the context of the Standard Model. The top quark is therefore the heaviest fermion in the Standard Model. The discovery of top quark has been made possible by the technological progress in high energy physics in the past 30 years. It all started with the development of the first proton-antiproton colliders at CERN, and then at Fermilab, culminating with the discovery of top quark in 1995. At present various properties of top quark including its mass, production cross section and various couplings are being measured at LHC at TeV scale. The discovery of Higgs boson, which was announced by CMS and ATLAS collaboration on July 4^{th} , 2012 completed the particle and field content of the minimal Standard Model.

4.2 Top Quark Production

Top quarks can be produced in proton-proton collisions at the LHC in two ways. First, the top quark can be produced through the electroweak interaction as a single top quark or anti-top quark. Secondly, the top quark can be produced in pairs of top and anti-top quarks through the strong interaction. The latter is the more dominant production mechanism and is the main focus of this thesis.

With a life time of the order of 10^{-25} s [39], a timescale which is about 20 times shorter than typical strong interaction's timescale, it is the only quark in Standard Model which can decay through the weak interaction. These properties makes the top quark very interesting to study as it is the only quark which can be directly accessed in experiments, as free quark.

4.2.1 Top Quark Production via the Strong Interaction

The production mechanisms of top quark pairs are shown in figure 4.1. The predominant production mechanism for top quarks in p-p collisions at LHC is from gluon fusion ($\approx 90\%$) with some additional contribution from ($\approx 10\%$) $q\bar{q}$ annihilation. This is in contrast to Top production at the Tevatron which was $\approx 85\%$ $q\bar{q}$ annihilation and $\approx 15\%$ gluon fusion.

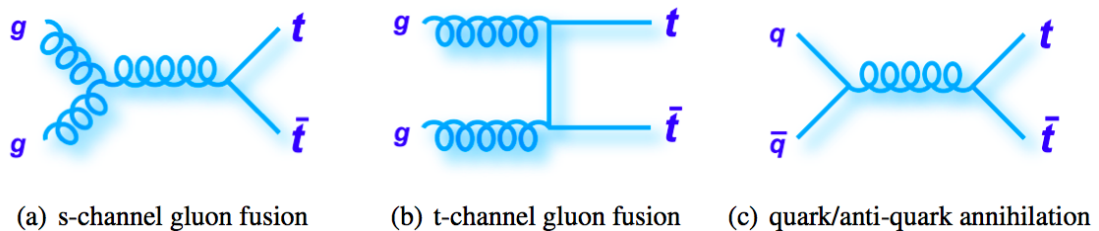


Figure 4.1: The $t\bar{t}$ pair production mechanisms.

One of the important characteristics of $t\bar{t}$ production mechanism is the cross section, which is the effective area that governs the probability of an absorption or scattering an event to occur. In terms of particle physics, this observable is interpreted as the likelihood of a certain interaction between particles. The top quark pair cross section is known theoretically as complete next-to-next-to-leading order calculations are available [40, 41] with next-to-next-to-leading log corrections applied, which means that the cross section is theoretically known up to $O(\alpha_s^4)$ with a precision of $^{+7.0\%}_{-7.8\%}$ at $\sqrt{s} = 7$ TeV and $^{+6.8\%}_{-7.6\%}$ at 8 TeV.

The precise measurement of the $t\bar{t}$ pair production cross section is important for two main reasons. First, this measurement provides a crucial benchmark for the QCD perturbative calculations. Secondly, the $t\bar{t}$ pair production process could be enhanced or suppressed by new physics processes producing top quark pairs. Hence, the cross section could be sensitive to the presence of new phenomena.

The production cross section of $t\bar{t}$ pairs has been measured both in $p\bar{p}$ and pp collisions

at Tevatron and LHC, respectively. Table 4.2 shows the latest result from the Tevatron ElectroWeak Working Group combining results from the $D\bar{\theta}$ and CDF collaborations. The most precise results from the LHC are given as well. So far all measurements of this quantity agree well with the theoretical predictions.

Collider	\sqrt{s} (TeV)	$\sigma_{t\bar{t}}^{obs}$ (pb)	$\sigma_{t\bar{t}}^{NNLO+NNLL}$ (pb)
Tevatron	1.96 ($p\bar{p}$)	7.65 ± 0.42	$7.164_{-0.475}^{+0.391}$
Large Hadron Collider	7 (pp)	162.0 ± 6.7	$172.0_{-13.4}^{+12.1}$
Large Hadron Collider	8 (pp)	227.0 ± 15.2	$245.8_{-18.7}^{+16.6}$

Table 4.2: Most precise measurements of the $t\bar{t}$ pair production cross section at the Tevatron [42] and at the LHC [43, 44] compared with the NNLO+NNLL theoretical calculations [40, 41]. The measurement assume a top quark mass of 172.5 GeV

4.2.2 Top Quark Production via Weak Interaction

Single top quarks are produced through electroweak interaction involving W_{tb} vertex. There are three production modes which are distinguished by the virtuality of the W boson and their corresponding Feynman diagrams can be seen in figure 4.2. The single top production modes are classified as follows:

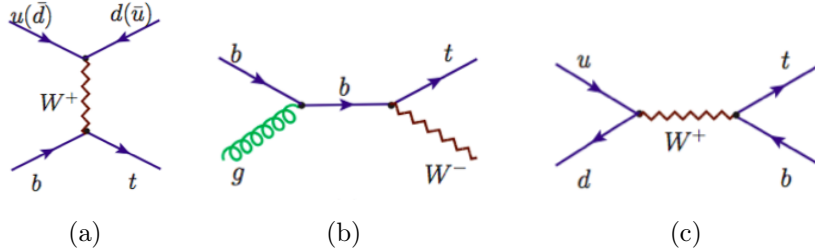


Figure 4.2: Feynman diagrams of single top quark production: (a) t-channel, (b) associated production (c) s-channel. By interchanging anti-quarks and quarks, the diagrams for single anti-top quark production can be obtained.

- **t-channel** - a virtual W boson strikes a b -quark inside the proton. In Wg fusion, gluon splits into a $b\bar{b}$, as a result b -quark get originated. Production in the t-channel is the dominant source of single top quarks at the LHC, the theoretical cross section for this channel is $\sigma_t = 64.6_{-3.2}^{+3.4}$ pb [45].
- **tW-channel** - is also known as associated production. The top quark is produced in association with a real W boson. The initial b quark is a sea quark inside the proton. The associated production at LHC surpasses the s channel, the single top

production cross section for this channel was predicted to be $\sigma_{tW} = 10.6 \pm 0.8 \text{ pb}$ [46].

- **s-channel** - this production mode is of Drell-Yan type and it is also known as $t\bar{b}$ production. A W boson is produced by the fusion of two quarks belonging to an $SU(2)$ isospin doublet. Production in the s-channel is pretty small at the LHC, $\sigma_s = 4.2 \pm 0.2 \text{ pb}$ [47].

4.3 Top Quark Decay

Within the SM top quarks decays to a quark q and W boson, via the weak interaction, where $q = s, b, d$. The decay rate is proportional to CKM matrix element $|V_{tq}|^2$. The channel $t \rightarrow W+b$ and charged conjugate of this channel occurs almost 100% of the time, as $|V_{tb}| = 0.999100_{-0.000004}^{+0.000034}$ [48].

Decay Mode	BR at Born level	BR
$W^+ \rightarrow e^+ \nu_e$	1/9	$(10.75 \pm 0.13)\%$
$W^+ \rightarrow \mu^+ \nu_\mu$	1/9	$(10.75 \pm 0.15)\%$
$W^+ \rightarrow \tau^+ \nu_\tau$	1/9	$(11.25 \pm 0.120)\%$
$W^+ \rightarrow u\bar{d}, c\bar{s}$	$231/9 = 6/9$	$(67.60 \pm 0.27)\%$

Table 4.3: At born level, branching ratios for all decay modes of the W^+ Boson. The BR values for the decays modes of the W^- are the same [49].

It is the W boson which dictates the classification of $t\bar{t}$ decay channels according to it's decay modes. The W boson's decay modes are shown in table 4.3 together with their corresponding branching ratios (BR). At Born level, all leptonic W decay modes have same probability, but each of the two hadronic modes is three times more likely due to the colour factor of three. As shown in figure 4.3, the $t\bar{t}$ decays are classified into following final states:

- **Dilepton** - both W bosons from the $t\bar{t}$ process decay leptonically (electron-electron, muon-muon or electron-muon) and the corresponding neutrinos. This channel has the smallest background, as it contains two leptons in it's final state.
- **lepton+jets** - is also known as semileptonic channel. In this case, one W boson decays leptonically into muon or electron, while the other one decays hadronically. This channel have a clear signature due to the presence of a lepton and provides the best combination of large statistics .

Top Pair Branching Fractions

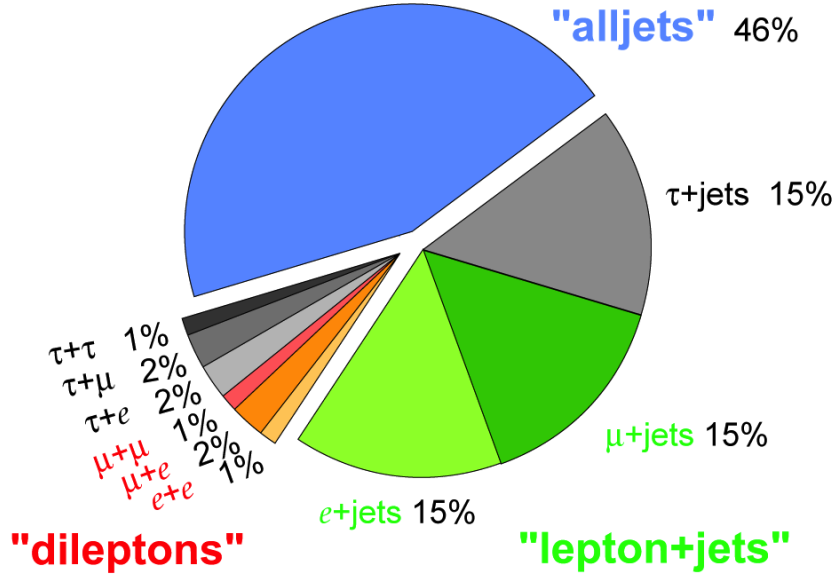


Figure 4.3: Decay channels of $t\bar{t}$ pairs and their corresponding BR, according to theoretical predictions at tree level.

- **all hadronic** - both W bosons from the $t\bar{t}$ process decay hadronically. Experimentally, the channel gets effected by large multijet background.

$t\bar{t}$ decays channels	$t\bar{t}$ decay mode	BR
ee	$t\bar{t} \rightarrow e^+ \nu_e e^- \bar{\nu}_e b\bar{b}$	$(1.14 \pm 0.02)\%$
$e\mu$	$t\bar{t} \rightarrow e^+ \nu_e \mu^- \bar{\nu}_\mu b\bar{b}$	$(1.14 \pm 0.02)\%$
$\mu\mu$	$t\bar{t} \rightarrow \mu^+ \nu_\mu \mu^- \bar{\nu}_\mu b\bar{b}$	$(2.28 \pm 0.04)\%$
$e + jets$	$t\bar{t} \rightarrow e^+ \nu_e q\bar{q}' b\bar{b}$	$(14.52 \pm 0.09)\%$
$\mu + jets$	$t\bar{t} \rightarrow \mu^+ \nu_\mu q\bar{q}' b\bar{b}$	$(14.52 \pm 0.09)\%$
$alljets$	$t\bar{t} \rightarrow q\bar{q}' q\bar{q}' b\bar{b}$	$(46.19 \pm 0.46)\%$
	τ final states	$(20.21 \pm 0.13)\%$

Table 4.4: $t\bar{t}$ Decay Channels and their BRs.

In this thesis dilepton channel is considered which has the smallest branching fraction in all $t\bar{t}$ decay channels. However, in the detector this channel has a distinctive and very clear signature, but the missing transverse energy coming from two undetected particles, called neutrinos dilute this channel. In addition, the background of this process from gluon-multijet production in the event is small, leading to a smaller effect of the

systematic uncertainty related to jets such as jet calibration on the measurement. In the di-lepton decay channel, each top quark decays into a W-boson and a bottom quark. The W-bosons in both decay branches, in turn, produce two leptons and two lepton neutrinos in the final state.

Depending on the final state of the events, the di-lepton decay channels can be classified into three subgroups, given by table 4.4. The e^+e^- and $\mu^+\mu^-$ decay mode in the $t\bar{t} \rightarrow bl^+\nu\bar{b}l^-\bar{\nu}$ event shares the same relative abundance value of around 1.8% while the BR of the $e^\pm\mu^\mp$ mode is around 3.6%.

4.4 Signature of $t\bar{t}$ in dilepton channel

The $t\bar{t}$ decay channel considered for the measurement presented in this thesis is the dilepton channel. The signature of dilepton $t\bar{t}$ event can be described as follows:

- Two isolated muon originating from one of the W boson decay. The muon has a large transverse momentum.
- Two neutrinos originating from W boson. The neutrino is reconstructed as large missing transverse energy.
- Two b -jets, as a result of hadronisation of the b quarks.

A Feynman diagram of $t\bar{t}$ dilepton channel can be seen in figure 4.4.

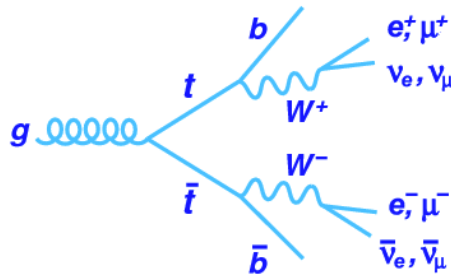


Figure 4.4: Example of Feynman diagram of $t\bar{t}$ decay in the dilepton channel at tree level.

4.5 Background Processes for $t\bar{t}$ Dileptonic Channel

The main sources of background arise from events in which we have misidentified leptons, fake leptons passing the selections, as W +jets or QCD , $t\bar{t}$ semileptonic events also

contribute and events with mismeasured MET (as Z +jets). Contributions from backgrounds with real leptons and \cancel{E}_T are irreducible, and are mainly dibosons or single top tW production. Following are background process which shall be considered in this analysis:

4.5.1 Drell Yan: $Z/\gamma^* \rightarrow l^+l^-$

It's final state consists of 2 high p_T , opposite charged and isolated leptons, but it doesn't have real \cancel{E}_T , as no neutrinos are present in the final state. Therefore, the main variable to reject it is the \cancel{E}_T , so a good control and understanding of its performance is essential as this background has one of the largest cross sections: 3503.71 pb . The presence of high p_T jets in the event also helps to reduce it, as it has less hadronic activity, this feature also helps to reduce the $Z/\gamma^* \rightarrow \tau^+\tau^-$, which has real \cancel{E}_T coming from the neutrinos produced in the tau decays.

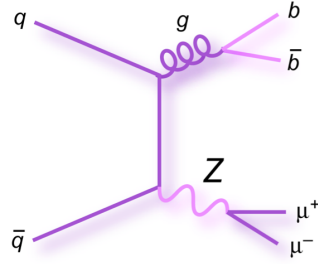


Figure 4.5: Example of a Feynman diagram for the Z +jets process

4.5.2 Dibosons: WW, WZ, ZZ

WW production, when both W -bosons decay leptonically also presents 2 isolated leptons and real \cancel{E}_T , the only difference from $t\bar{t}$ channel is the presence of high p_T jets coming from the hadronisation of the 2 b -quarks, so it can be used to reduce this background, together with the b -tagging requirement.

WZ and ZZ can present slightly different signatures depending on how both bosons decay, the $W \rightarrow l\nu$ branching ratio is about 10% per lepton flavour and 3% in the case of $Z \rightarrow l^+l^-$, so the main contributions will come from: $W^\pm Z \rightarrow q\bar{q}l^+l^-$, $W^\pm Z \rightarrow l^\pm\nu l^+l^-$, $ZZ \rightarrow l^+l^-l^+l^-$, $ZZ \rightarrow l^+l^-\nu\bar{\nu}$, $ZZ \rightarrow l^+l^-q\bar{q}$. In both cases the \cancel{E}_T requirement will help to reduce these backgrounds and also b -tagging. Anyway, the cross section value is small compared to the signal: 54.838 pb the WW decaying to 2 leptons, 33.21 pb the WZ decaying to 3 leptons and 17.654 pb the inclusive ZZ production.

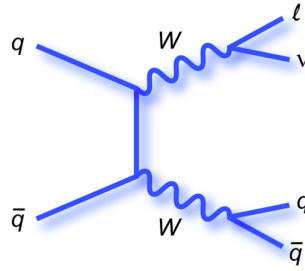


Figure 4.6: Example of a Feynman diagram for the WW process

4.5.3 Single Top

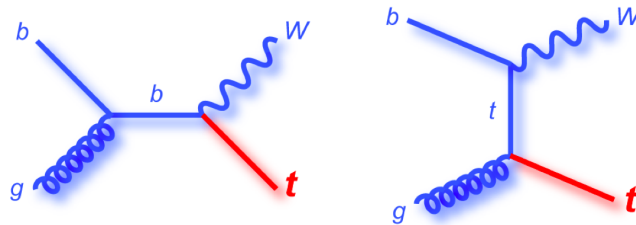


Figure 4.7: Example of a Feynman diagram of single top tW-channel production

It is one of the main remaining backgrounds after the application of full selection criteria. The tW channel is the one relevant and it has almost the same signature as the $t\bar{t}$ process, it presents 2 isolated leptons, \cancel{E}_T from the neutrinos and jets, although it has only one b-jet, so the b-tagging helps to reduce this background, specially if the presence of at least 2 b-tagged jets is required in the selection. The cross section is smaller than the signal about one order of magnitude: 11.1 pb.

4.5.4 W + jets

This background has only 1 isolated lepton, but due to its huge cross section (36257.2 pb), it can represent a dangerous background when one non-prompt lepton is passing the selection, so a good control on the identification and isolation must be performed to reduce the fake lepton contamination as much as possible. In order to select electrons and muons from W bosons from $t\bar{t}$ decays, events should have two oppositely charged, energetic, good identification and isolated leptons. To suppress the Z+jets contribution the $\mu^+\mu^-$ and e^+e^- events are required to have invariant mass reconstructed outside Z mass window, and also to have a significant \cancel{E}_T typical of signal due to presence of neutrinos in the final state. Further suppression of all backgrounds is achieved by

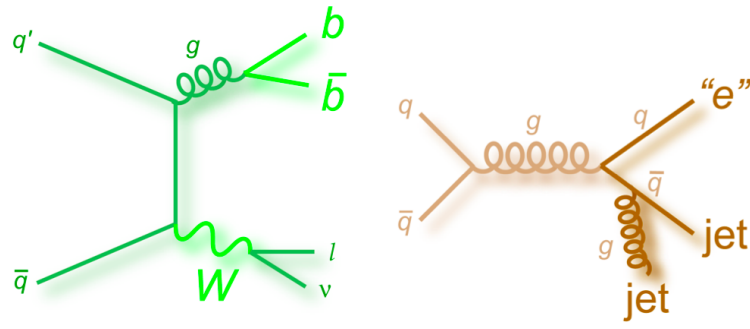


Figure 4.8: Example of a Feynman diagram for the W +jets and multijets production

requiring presence of energetic jets in an event, even more if they are required to be b -tagged.

Chapter 5

Event Reconstruction

To analyse an event, raw detector signals are interpreted in terms of energy and coordinates. Using this raw information the detected hits are reconstructed in terms of physics objects, such as muons, photons. This chapter will discuss the physics object's reconstruction, relevant to this analysis, namely the reconstruction of jets, b -jets, electrons, muons and missing transverse energy. The software used to reconstruct physics objects is the CMS Software (CMSSW) Framework. More details on reconstruction of these and other objects at the CMS experiment can be found in [50].

5.1 Particle flow

In order to reconstruct physics objects from the measured detector signals, several reconstruction steps have to be applied.

Within the procedure of reconstruction of tracks, various hits in different parts of the CMS tracker system are combined using a combinatorial track finder [51] which is based on a Kalman Filter [52]. The result of this iterative procedure is a collection of reconstructed tracks which is used further on e.g. to identify vertices.

For each event, a Primary Vertex (PV) corresponding to the pp interaction point is demanded, which is reconstructed from a minimum of four tracks within a longitudinal distance of $|z| < 24 \text{ cm}$ along the beam direction and a distance of $\rho < 2 \text{ cm}$ to the nominal interaction point (beam spot) in the transverse interaction plane. Because of the spread of the individual protons in the colliding bunches, beamspot and PV are not identical. In case of several reconstructed vertices, the one with the highest p_T^2 sum of all associated tracks is considered as PV. Secondary vertices are e.g. used to identify jets originating from b quarks.

Tracks not originating from the selected primary vertex or its associated secondary

vertices are considered as PU events and are discarded from the analysis.

Single particles are then reconstructed combining reconstructed tracks and vertices, energy deposits in calorimeters and signals in muon chambers. All objects used throughout this analysis are reconstructed using the Particle-Flow (PF) algorithm for event reconstruction [53]. The PF technique attempts to maximize the amount of detector information used for the object reconstruction and treats the event as a whole. The aim of the PF algorithm is the individual reconstruction of every stable particle, considering photons, electrons, muons, neutral and charged hadrons. These particles are called PF candidates. An illustration of the PF concept can be found in figure 5.1. In general, the PF algorithm consists of the following steps [54]:

- clustering of energy deposits in the calorimeters
- track reconstruction and extrapolation of the tracks to the calorimeters
- muon identification
- electron pre-identification
- linking of topologically connected elements
- particle identification and reconstruction

The CMS detector is especially suitable for the application of the PF technique due to its high performance silicon tracker, the magnetic field provides good separation power, the ECAL being highly granular and hermeticity of ECAL and HCAL. Moreover, the list of individual particles from the PF procedure is successively used to build jets, to calculate the missing transverse energy, in order to identify and reconstruct τ leptons from their decay particles and to identify b jets. It has been proven that especially the performance of jets, E_T^{miss} and the isolation of charged leptons can be significantly improved using the PF algorithm.

To avoid the overlap of jets and leptons, so-called Top Projections are used, i.e. loosely isolated PF electrons and muons are excluded from the jet clustering step. This follows the prescription of the PF2PAT algorithm described in [56].

5.2 Muons

In general, muons in CMS are reconstructed from tracks found in the inner tracker and/or in the muon system as detailed in [57]. Due to the unique signature in the muon system,

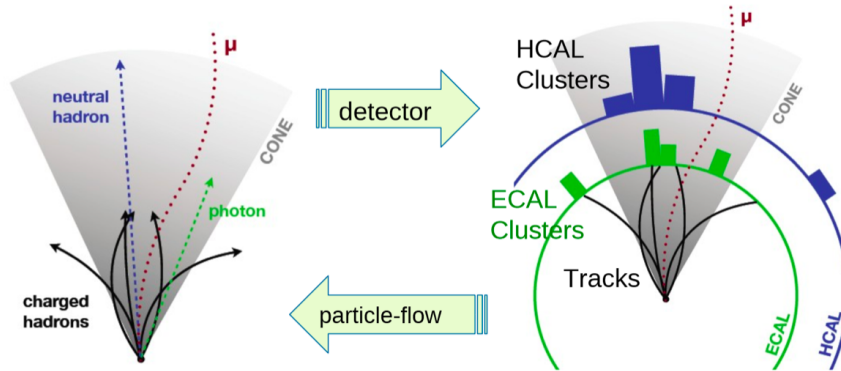


Figure 5.1: Illustration of the particle-flow concept to reconstruct every individual muon, electron, photon, charged and neutral hadron from a maximum of detector information[55].

the low interaction with the detector material and the superior resolution of the tracking system, the muon is one of the objects that can be reconstructed best in CMS.

5.2.1 Signal Muon Selection

In addition to the identification criteria embedded in the ParticleFlow algorithm, muon identification requirements outlined in table 5.1 are applied in the analysis to further purify the muon reconstruction. First requirement is that the muon is reconstructed using the particle flow algorithm[58, 59]. Further, for the reconstruction, the global muon (tracker and chamber) and tracker muon algorithms are being used[60]. Then the muon is required to have P_T greater than 20 GeV . In figure 2.8, the quarter part of CMS detector is given. The entrances of the barrel (muon chambers) can't detect muons very well. For this reason, the absolute pseudo-rapidity should be smaller than 2.4.

Isolated, prompt leptons as a result of W boson decays should be selected. Therefore, isolation requirements are set. A cone of $\Delta R = \sqrt{(\Delta\eta)^2 + (\Delta\phi)^2}$ equal to 0.4 is constructed around the muon track. The sum of the momenta inside this track, and the electromagnetic and hadronic calorimeter energy deposits are calculated, excluding the contribution of the muon itself. The ParticleFlow algorithm reconstructs all charged and neutral hadrons as well as photons. Hence the relative isolation can be described in terms of particles rather than energy deposits and tracks. The particle based relative isolation provides an improved isolation definition compared to the traditional relative isolation criterion. Nevertheless, this definition has been found very sensitive to pileup

effects. This pileup dependence was found especially in the neutral hadrons and photons since the charged hadrons allow matching to the primary vertex and are thus less affected. During 8 *TeV* operation, where the pileup was more pronounced compared to the 7 *TeV* running period, this has led to a redefinition of the particle based isolation corrected for the pileup effect by adding a subtraction term for the transverse momenta of the pileup particles.

$$I_{rel} = \frac{\sum p_T^{chargedhadrons} + \max[0, \sum p_T^{neutralhadrons} + \sum p_T^{photons} - 0.5 \sum p_T^{PU}]}{p_T^\mu} \quad (5.1)$$

If this scalar sum exceeds 20% relative to the value of the muons candidate momentum, the particle is rejected, as it is considered to be non isolated. The ratio of the scalar sum to the particle's momentum is called the "relative isolation" (reliso). Thus, the relative isolation has to be smaller than 0.20 in order for the muon to be isolated. To assure that the muon originates from the initial *pp* collision, the two-dimensional impact parameter d_B with respect to the beam spot is required to be smaller than 0.04 *cm*.

Criterion	$\sqrt{s} = 8\text{TeV}$
Particle Flow Muon ID	isPFMuon
Global or Tracker Muon	required
Transverse momentum	$> 20 \text{ GeV}$
$ \eta $	< 2.4
reliso	< 0.2 , cone 0.4

Table 5.1: Overview of the muon identification criteria used in the 8 *TeV* datasets[61].

5.3 Electrons

The basic reconstruction of electrons in CMS is based on the hits in the tracking system and the energy deposits in the ECAL as detailed in [62]. Consequently, the identification of electrons as in this case the distinction is more difficult than for muons as the distinction from other particles is more complicated. Furthermore, the lower mass of the electron leads to a sizeable amount of emitted photons through bremsstrahlung produced from interaction with the tracker material. This has to be considered within the reconstruction process to re-assign the radiated photons and take into account potential kinks in the reconstructed electron trajectory. Technically, this is done using a Gaussian Sum Filter algorithm [63]. To distinguish electrons from other particles, an MVA-based

pre-identification is applied within the PF procedure using shower shape, track quality and kinematic variables as well as a criteria for the momentum-energy matching between the tracker and the ECAL, which is dominated by bremsstrahlung effects.

5.3.1 Signal Electron Selection

Like muon, in addition to the identification criteria embedded in the ParticleFlow algorithm, electron identification requirements outlined in table 5.2 are applied to further purify the electron reconstruction. The transverse momentum should be higher than 20 GeV and the absolute pseudorapidity should be below 2.5 due to detector limitations. The distance from the reconstructed primary vertex should be smaller than 0.04 cm so that the electron is originating from this vertex. Since a photon can convert into two electrons and give a false signal, the conversion rejection must be set to true. Further, a minimum amount of hits in the inner tracker is set. In order to know if it is a good electron, multi variable triggers (MVA [64]) are being used. Similar as for the muon, the electron should be isolated to ensure that the electron is descending from a W boson decay.

To select isolated electrons, the particle based isolation can be used for electrons using the definition in eq. 5.1. The isolation is determined in a cone of radius 0.3 around the electron track. For the collisions at 8 TeV , where the pileup influence is increased, the particle based isolation definition can be extended just as in the muon case with a pileup subtraction term. In this case the so-called effective area correction term ρA_{eff} [65] is added to the equation since it provides better isolation performance. Thus, the relative electron isolation is defined as:

$$I_{rel} = \frac{\sum p_T^{chargedhadrons} + \max[0, \sum p_T^{neutralhadrons} + \sum p_T^{photons} - \rho A_{eff}]}{p_T^\mu} \quad (5.2)$$

where ρ is the energy density in event and A_{eff} is called effective area

5.4 Jets

Unlike muons and electrons, bottom and anti-bottom ($b\bar{b}$) quarks do not remain free particles long enough to travel through the tracker. As the $b\bar{b}$ quarks fly through the detector, due to color confinement, the separation of the $b\bar{b}$ pair produces other quark-antiquark pairs until all of the quarks have been rearranged into color-neutral hadrons. The hadrons then decay into lighter quarks and possibly leptons, thus forming jets of particles which are seen in the detector.

Criterion	$\sqrt{s} = 8\text{TeV}$
identification	GsfElectron
Transverse momentum	$> 20 \text{ GeV}$
$ \eta $	< 2.5
Transvers IP of the electron w.r.t primary vertex (cm)	0.04
GSF track # of hits	≥ 0
MVA	> 0.5
number of Hits	≥ 1
Conversion rejection	$> \text{applied}$
reliso	0.15, cone 0.3

Table 5.2: Overview of the electron identification criteria used in the 8 TeV datasets [66].

5.4.1 The anti- k_T algorithm

The jets are clustered from particle flow objects. To unambiguously assign the particles to jets, a jet algorithm is used. At the CMS experiment, the default algorithm is the so-called anti- k_T algorithm [67] with a radius parameter of $R = 0.5$. This algorithm effectively clusters particles around the highest p_T objects, until the maximally allowed distance is reached. For the clustering procedure the following equations are used:

$$d_{ij} = \min(p_{t,i}^{-2}, p_{t,j}^{-2}) \frac{(y_i - y_j)^2 + (\phi_i - \phi_j)^2}{R^2} \quad (5.3)$$

$$d_i = p_{t,i}^{-2} \quad (5.4)$$

Here, y denotes the rapidity of the object defined as:

$$y = \frac{1}{2} \ln\left(\frac{E + p_z}{E - p_z}\right) \quad (5.5)$$

As first step, all d_{ij} and d_i are searched for the minimum. If the minimal value is a d_{ij} , the corresponding two objects i and j are fused to a single object and the first step is repeated. If a d_i is the smallest value, the corresponding object is declared as final-state jet and is removed from further processing. When no more particles remain, the process is finished.

5.4.2 Jet Calibration

The four-momentum of the initial parton or gluon is reflected by the sum of the four-momenta of all jet constituents. However, the momentum of the reconstructed jets does not correspond to the true particle-level energy obtained from *gen jets*(generator level

jets) clustered from stable particles on generator level. The main reasons for this difference are the non-uniform and non-linear response of the calorimeter, energy losses from particles outside the jet area or undetected neutrinos or additional clustered particles e.g. from PU interactions. Hence, a calibration of the measured raw jet momenta is needed [68, 69].

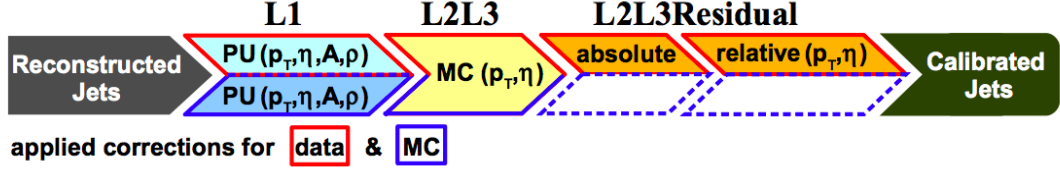


Figure 5.2: Illustration of the factorized approach of Jet Energy Calibration in CMS.

These Jet Energy Corrections (JECs) are centrally derived by the CMS JetMET Physics Analysis Group [70] using MC predictions as well as data from di-jet, Z +jet and γ +jet samples [71, 72]. CMS follows a factorized approach involving the following correction steps as illustrated in figure 5.2:

L1 (data&MC): p_T and η dependent correction for the contribution of underlying PU processes using the concept of jet areas [73, 74] with the median of the energy density (ρ) and the jet area (A)

L2L3 (data&MC): p_T and η dependent corrections to compensate for the non-linear and non-uniform response of the calorimeters, derived from MC predictions, corrected to generator jet level

L2L3 Residual (data only): correction for remaining differences of data with respect to MC predictions, derived from the MC prediction to data ratio

For this analysis, jets have been calibrated up to the absolute Jet Energy Scale (JES) of L3 in simulation and L2L3Residual in data using the official Summer13 V5 CMS JECs as detailed in [75]. Furthermore, the jet energy resolution is found to be slightly larger in data than in simulation.

5.4.3 Jet Selection

For the jet selection, again the standard requirements are set. For similar reasons as the leptons, the jets absolute pseudorapidity has to be below 2.4 (see table 5.4). Further, the transverse momentum should be higher than 30 GeV since the transverse momentum is not well reconstructed below this threshold. To reject fake jets from instrumental noise

or other particle signatures, common PF jet identification requirements are applied to the selected jets. These requirements are minimalistic and based on the composition of the reconstructed jet:

Criterion	$\sqrt{s} = 8\text{TeV}$
Transverse momentum	$> 30 \text{ GeV}$
$ \eta $	< 2.5
Jet Energy Corrections (JEC)	L1FastJet + L2L3 (+L2L3Residual for data)
JER smearing in MC	applied
Jet ID	
charged hadron energy fraction	> 0
neutral hadron energy fraction	< 0.99
electron energy fraction	< 0.99
photon energy fraction	< 0.99
multiplicity of charged particles	> 0
number of clustered PF candidates	> 1

Table 5.3: Jet selection criteria[76].

5.5 *b*-Jet Identification

The CMS collaboration is able to identify jets coming from a *b* quark. The collaboration has developed a variety of *b*-tagging algorithms based on the use of impact parameters of charged particle tracks, the properties of reconstructed decay vertices and/or the presence of a lepton. In order to discriminate between *b* (or *c*) and light flavor jets, a variety of reconstructed objects is used. There are algorithms that use only one observable, but there are also *b*-tagging algorithms that combine observables in order to have a higher discriminating power for each jet. The *b*-tagging algorithms use a discriminating value or working point. Based on the misidentification probability for light flavour jets the working points are defined as loose (L), medium (M), and tight (T)[77]. *B* hadrons are produced during fragmentation of *b* quarks and have a large lifetime of about 1.5ps [78]. Their decay length is about $450 \mu\text{m}$, resulting in a displaced vertex (see figure 5.3). This displaced or secondary vertex is observed by the CMS silicon tracker by looking at the intersection point of the tracks. By looking at displaced vertices, one can see if the jet is originating from a *b* quark. There are two main kinds of *b*-tagging algorithms. First category is where the identification is based on the use of track impact parameters, these impact parameters are defined as the distance between the primary vertex and the

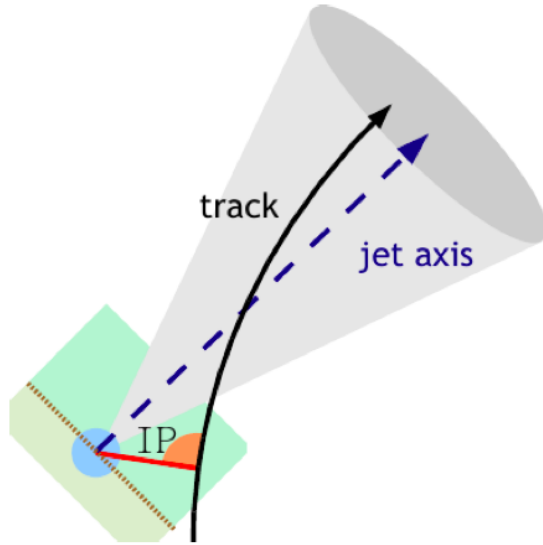


Figure 5.3: Impact parameter between primary vertex and track.

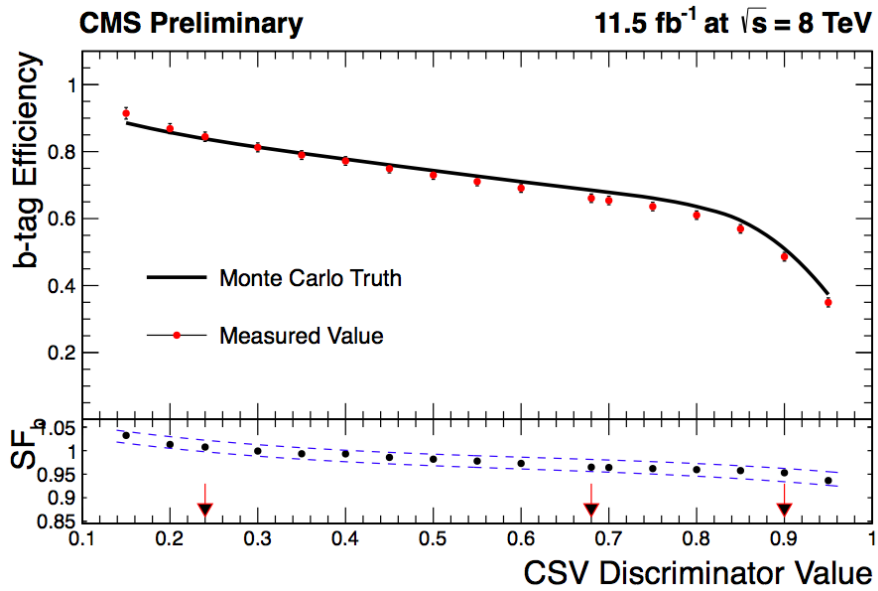


Figure 5.4: Efficiency of b-jet tagging CSV algorithm. the lower panel shows scale factors SF_b [80].

linearised track in the point of minimal distance between the track and the jet axis, as shown in figure 5.3 [79]. Another category is the one with b -tagging algorithms based on the use of a secondary vertex. More information about b -tagging can be found in [77].

The b -tagging algorithm used in this analysis is the Combined Secondary Vertex (CSV) in the medium operating point, the base of this algorithm is the use of secondary vertices with a track based lifetime information. With a value of the discriminant >0.244 , the threshold on the discriminant value chosen in this analysis corresponds to an efficiency of about 80-85% for each b jet in di-lepton $t\bar{t}$ signal events and a 10% mistagging rate of light-flavour or gluon jets being identified as b jets, as estimated from simulation. The b -tagging efficiency is estimated from $t\bar{t}$ events in data, as described in [80]. In figure 5.4, the efficiency of b -tagging for the CSV b -tagging algorithm is given.

5.6 Neutrinos

Neutrinos do not interact at all in the CMS detector. Although the energy of the neutrino is never detected, the total energy in the event is still conserved. The missing energy in any CMS event is attributed to neutrinos. In theory the sum of all the momentum four-vectors in an event would be zero due to energy conservation. However, it is not possible to reconstruct all the energy in the z direction. Recall, the incoming partons contain a fraction of the proton's momentum. The initial longitudinal momentum is unknown; therefore, only the transverse energy, or the energy in the plane perpendicular to the beam line, is considered. Since the masses of the detector particles are much less than the center of mass energy, the masses can be assumed to be 0. The sum of the transverse momentum vectors in an event should be zero since the original momentum in the transverse plane is assumed to be zero (i.e. The incoming partons can actually have a transverse component of momentum, but it is in general small compared to the longitudinal component). The missing transverse energy is then the modulus of the sum of the known transverse momenta in the event (i.e. It is important to note that if there is more than one neutrino in the event it is impossible to distinguish between the two. The \vec{E}_T^{miss} in that event is the vectorial sum of the transverse energies of the neutrinos.). The missing transverse energy vector, defined in equation 5.7, is referred to as \vec{E}_T^{miss} [81].

$$\vec{p}_T^{total} = 0 = \sum \vec{p}_T^{reco} + \sum \vec{E}_T^{miss} \quad (5.6)$$

$$\vec{E}_T^{miss} = - \sum \vec{p}_T^{reco} \quad (5.7)$$

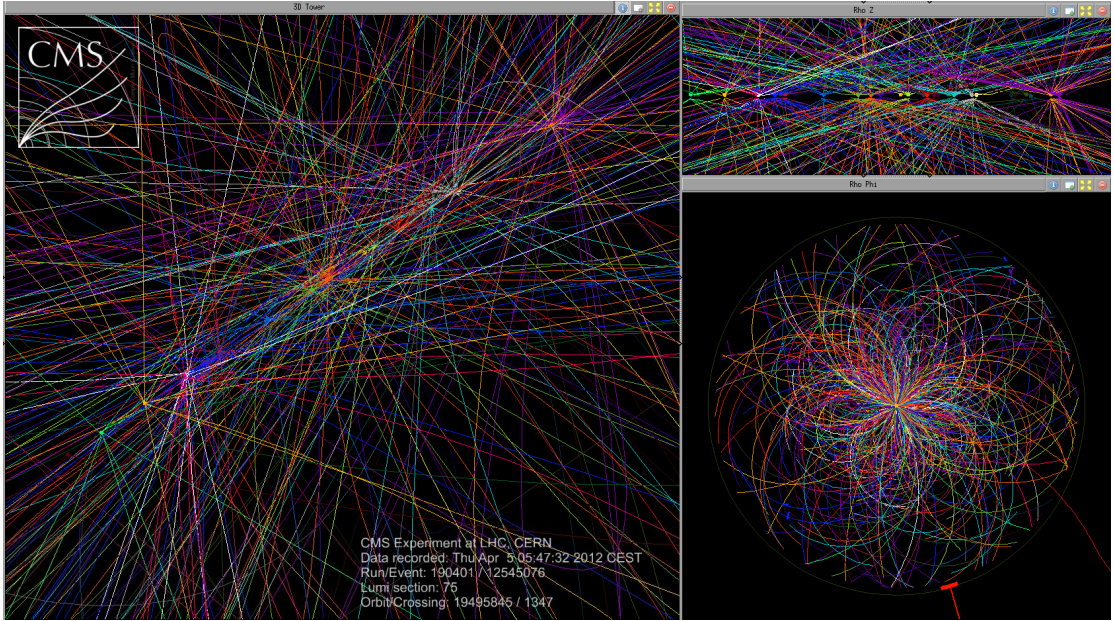


Figure 5.5: Event display of an event with 29 vertices [84].

5.7 Pile-up removal

For the analysis of top quarks, only the objects coming from the top quark event need to be considered while other objects from a different interaction, i.e. a different vertex can be ignored. The vertex with the highest p_T sum of all tracks coming from this vertex is considered the interesting vertex. All the tracks from other vertices and their corresponding energy deposits in the calorimeters are projected out of the event so that following reconstruction steps do not take them into account any more. This procedure is called Charged Hadron Subtraction (implemented using pfNoPileUp [83]) because only particles with an electric charge can be seen in the tracking system and thus be assigned to a vertex. figure 5.5 shows a full event with multiple vertices. After the Charged Hadron Subtraction, one can treat it like an event with only one primary vertex.

5.7.1 Top projections

One problem in the reconstruction is that there can be ambiguities. For example, a reconstructed muon could be a jet constituent or a high energy deposit in the electromagnetic calorimeter could be caused by an electron or by a photon. In order to resolve these ambiguities, the PF2PAT [83] algorithm is used. In this work, the particles are reconstructed following a fixed order. As the muons are the only particles which can be detected in the muon system, we first reconstruct all muons. However, we are only

interested in isolated leptons which come directly from the W boson (or an intermediate τ), while muons inside a jet (for example originating from a B hadron) are not used. Analogous to the pile-up removal all the detector information which is assigned to these isolated muons is then projected out of the event so that for example hits in the tracking system which were caused by the muon are no longer available for the reconstruction of other objects (pfNoMuon). The next objects to be reconstructed are the electrons.

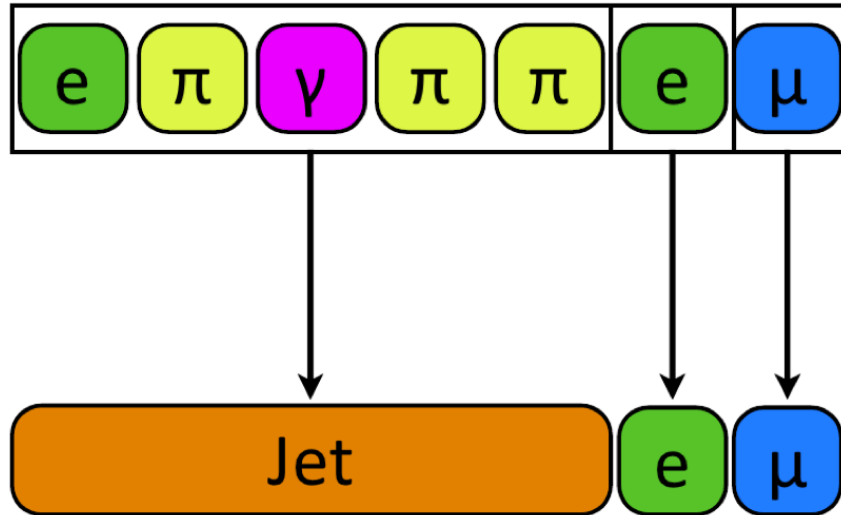


Figure 5.6: Reconstruction of particles in an event. From all seven reconstructed particles (top) the two leptons on the right are projected out as isolated leptons. The remaining five particles (left) then form a jet[83].

Again only isolated electrons are considered in the analysis and thus their entries from the tracking system and from the electromagnetic calorimeter are removed (pfNoElectron).

Only after the isolated muons and electrons have been removed, jets can be reconstructed. This is done using the Anti- K_T algorithm with a cone of 0.5 in η - ϕ space ($\Delta\eta^2 + \Delta\phi^2 < 0.52$).

Finally, the missing transverse energy in the event can be calculated from the vectorial sum of the momenta of all reconstructed objects.

The steps are visualized in figure 5.6. All particles in the event are in the top row. The two rightmost particles, a muon and an electron, are isolated. Thus they are projected out of the event, indicated with the arrows to the bottom, where a list of all objects in kept. The remaining particles in the top row, including the electron on the left, are not isolated. They are clustered into jets.

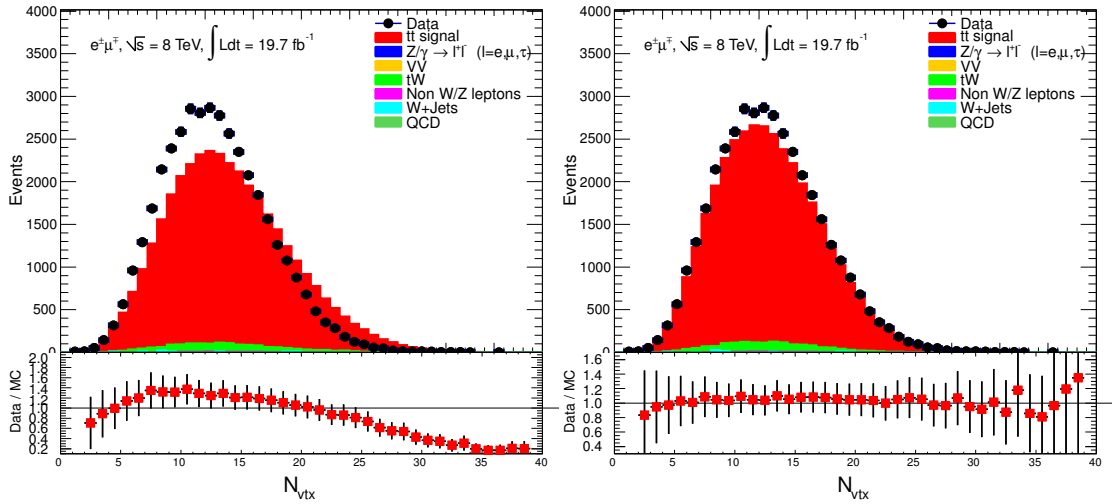


Figure 5.7: The distribution of the number of vertices in the $e\mu$ channel. Left without pile-up reweighting, right with pile-up reweighting.

5.8 Corrections Applied to the Simulated Events

There are subtle detector related effects that cannot be modeled perfectly. Therefore, studies are made in an independent way for each of these effects and corrections are provided in order to reproduce the data in simulation. The uncertainties introduced by applying the corrections on the simulation, are accounted for in the statistical method and are discussed in Chapter 7.

5.8.1 Pile-up Reweighting

For each single bunch crossing at the Large Hadron Collider, several interactions could take place. In time pile-up is defined as all particles descending from the same bunch crossing, but from a different proton proton interaction. While, out of time pile-up, is defined as the left over signal from a previous bunch crossing. The Monte Carlo samples are generated with simulated pile-up meant to roughly cover the conditions for the data taking period. Though, the pile-up in Monte Carlo is produced before the actual data taking begins, and therefore it is essential to reweight the pile-up. The pile-up calculation is done centrally by the pile-up studies group at CMS[85]. Information on the pile-up reweighting procedure can be found in [86]. In figure 5.7, the effect of pile up reweighting is shown. The distribution of the simulation without pile-up reweighting is broader than the data distribution. In other words, the simulation expects more vertices in the tail of the distribution than reality.

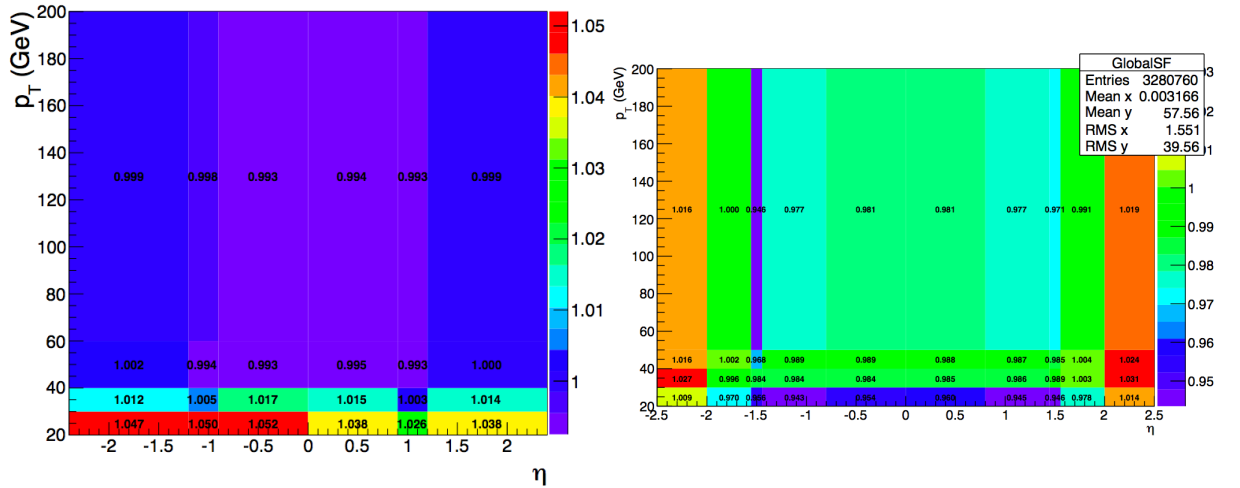


Figure 5.8: Global SF as a function of (η, p_T) of the lepton, for muons (left) and electrons (right)

5.8.2 Lepton Isolation, Identification and Trigger Reweighting

In order to correct for the High Level trigger modeling, scale factors are applied. Information about the lepton identification and isolation efficiency reweighting calculation can be found in [87]. The resulting scale factors are listed in table 5.4 and can be seen in figure 5.8. These are obtained for each channel of the analysis based on samples repro-

Channel	SF_{Trig}	$SF_{Iso,ID}$	$SF_{Trig,Iso,ID}$
ee	0.995 ± 0.011	0.975 ± 0.006	0.970 ± 0.013
$e\mu$	0.954 ± 0.010	0.986 ± 0.004	0.941 ± 0.010
$\mu\mu$	0.959 ± 0.010	0.999 ± 0.006	0.958 ± 0.012

Table 5.4: The lepton identification and isolation efficiency scale factors taken from [87].

cessed in CMSSW53X. The trigger scale factors are obtained with data corresponding to 19.1 fb^{-1} .

5.8.3 B-tag Efficiency Reweighting

For each jet in the event, there is an efficiency of b -tagging. The performance of this b -tagging in data and simulation has been studied, and the outcome is that the efficiencies are not the same. Thus, also here there is a mis modeling due to detector effects. The efficiency of b -tagging in Monte Carlo for each jet is rescaled in order to match the efficiency in data. These scale factors are provided by the b -tagging working group of the CMS collaboration [104], and are function of the transverse momentum and the

pseudo rapidity. The efficiency of the Monte Carlo simulation has to be rescaled so that:

$$\epsilon_{true} = \epsilon_{MC} \times SF \quad (5.8)$$

where SF is the scale factor provided by the b -tagging working group. These scale factors are only provided for jets with a transverse momentum higher than 20 GeV and an absolute pseudorapidity below 2.4. For this reason, only jets fulfilling these requirements are considered.

First, the raw efficiency of b -tagging (and fake rates) in simulation is determined. This is done by taking the ratio of the number of b -tagged jets (jets that pass the discriminating threshold) over all jets coming from a b quark (or c , or light quarks):

$$\epsilon_{true} = \frac{b - tagged jets}{b - jets} \quad (5.9)$$

The raw efficiency is a function of the transverse momenta. The efficiencies are calculated for the signal and other backgrounds a same efficiency as $t\bar{t}$ is assumed. Further, it is assumed that the efficiencies measured in the $e\mu$ channel are assumed to the same for all channels. For the secondary vertex algorithm, the b -tagging efficiency should be 62% with a mistag rate of 1.5% for jets with a transverse momentum between 50 and 80 GeV . This trend can easily be seen for the b -jets, but is harder for the fake rates due to low statistics.

type	value
SF_b	0.984 ± 0.016
SF_c	0.984 ± 0.032
SF_l	1.08 ± 0.09

Table 5.5: Scale factors for CSVL tagger.

In practice, the true b -tag efficiency is obtained using the algorithm described in [105]. When the b -tag scale factor provided by the b -tagging working group at CMS[104], is greater than one, the efficiency in data is greater than the efficiency in Monte Carlo. To solve this, the simulation efficiency should be adapted such that the it matches the one from data. The percentage of extra jets that have to be tagged as b -jets in simulation is defined as

$$mistag\% = \frac{1 - SF}{1 - \frac{SF}{\epsilon_{MC}}} \quad (5.10)$$

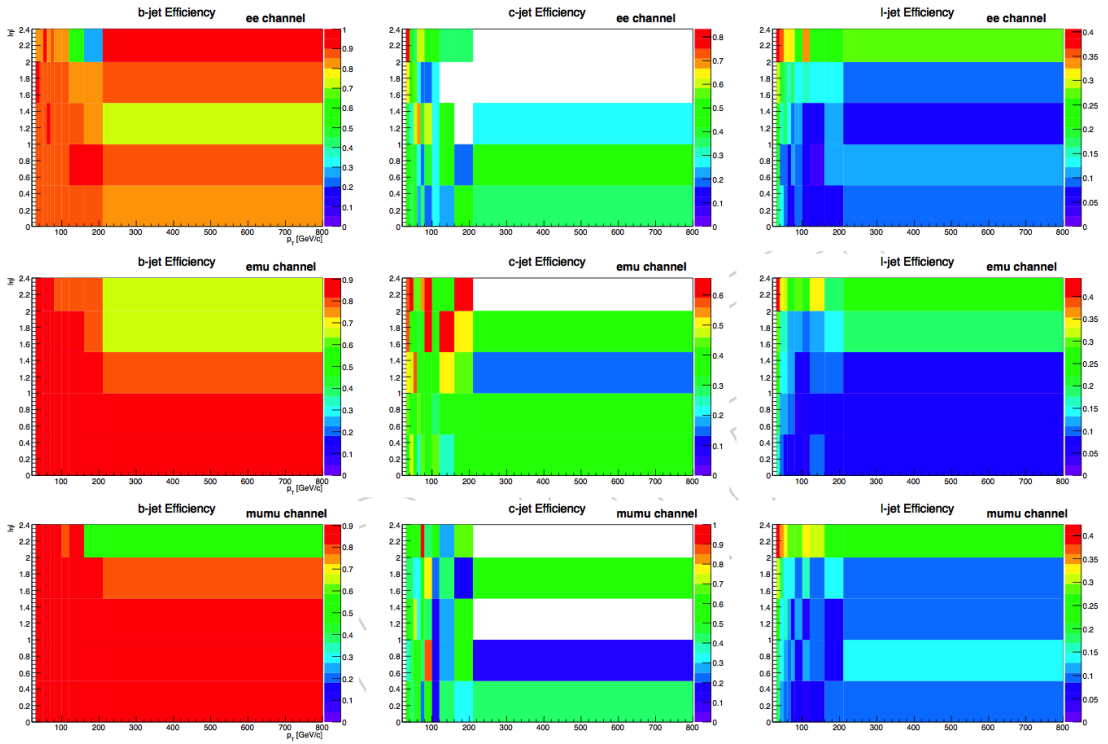


Figure 5.9: b-tagging efficiency of individual b -jets (left) and mistag rate for c -jets (middle) and l -jets (right) as function of jet p_T and η for e^+e^- (top), $\mu^\pm e^\mp$ (center) and $\mu^+\mu^-$ (bottom) channels, determined from the simulation.

Then the non b -tagged jets get randomly tagged according to this percentage. When the scale factor is smaller than one, less jets get b -tagged in data compared to simulation. B -tagged jets get randomly untagged according to the SF. For the CSVL tagger used in this analysis, the SF for the b -tagging efficiency per jet is found to be around 0.98 as shown in table 5.5. The resulting distributions can be found in figure 5.9.

Chapter 6

Data Samples and Event Selection

Dilepton $t\bar{t}$ events result in four types of objects that can be observed by our detector: electrons, muons, jets and \cancel{E}_T . To select such events, we require two leptons, two jets and a significant amount of \cancel{E}_T . The leptons and jets must be central and energetic and the lepton invariant mass must be inconsistent with that of the Z boson. Selected events must also pass requirements independent of these objects to verify that they come from clean collisions rather than noise or beam effects.

6.1 Collision Data Sample

Each event in CMS data is placed into at least one primary dataset based on the trigger path(s) that accepted it. The primary datasets are then processed further to create secondary datasets (also called "skims"). Because the most prominent signature of dilepton $t\bar{t}$ events is the pair of high p_T leptons, the secondary datasets used in this analysis are dilepton skims of the electron and muon primary datasets. The only requirement for these skims is a pair of leptons with $p_T > 10 \text{ GeV}/c$ for each of them. The data samples used in this analysis are listed in table 6.1. They were recorded during 2012 and correspond to a total integrated luminosity of 19.7 fb^{-1} . In order to locate all $t\bar{t}$ events, we process both muon and electron datasets. To avoid overlap in the $e^\pm\mu^\mp$ channel, we take events from the muon dataset only if they fire a muon trigger and events from the electron dataset only if they fire an electron trigger and do not fire any muon triggers. This algorithm ensures that there is no double-counting and does not miss the rare $e^\pm\mu^\mp$ events which do not fire a muon trigger.

CMS data is divided into "runs" which are further subdivided into luminosity sections. A run is simply a continuous period of data-taking. A luminosity section is a fixed time interval of approximately 23s and corresponds to the smallest time period for

Dataset	Luminosity (pb^{-1})
Double Muon	
/DoubleMuParked/Run2012A-22Jan2013-v1/AOD	889.362
/DoubleMuParked/Run2012B-22Jan2013-v1/AOD	4.426
/DoubleMuParked/Run2012C-22Jan2013-v1/AOD	7.114
/DoubleMuParked/Run2012D-22Jan2013-v1/AOD	7.318
Double Lepton	
/MuEG/Run2012A-22Jan2013-v1/AOD	889.362
/MuEG/Run2012B-22Jan2013-v1/AOD	4.429
/MuEG/Run2012C-22Jan2013-v1/AOD	7.152
/MuEG/Run2012D-22Jan2013-v1/AOD	7.309
Double Electron	
/DoubleElectronParked/Run2012A-22Jan2013-v1/AOD	889.362
/DoubleElectronParked/Run2012B-22Jan2013-v1/AOD	4.429
/DoubleElectronParked/Run2012C-22Jan2013-v1/AOD	7.152
/DoubleElectronParked/Run2012D-22Jan2013-v1/AOD	6.921

Table 6.1: All data samples used in the analysis.

which the status of the detector is recorded. Not all data is suitable for analysis because it may have been taken with parts of the detector off or not working properly. Thus, all of the recorded datasets are filtered by removing bad runs and luminosity sections to select only good quality data.

6.2 Monte Carlo Signal and Background Modeling

Simulation samples are used to verify that we understand the data and to measure the top quark mass by comparing data to simulated templates corresponding to different top quark masses. The samples used in the analysis are $t\bar{t}$ and its most significant backgrounds: Drell-Yan and single top produced in the tW channel. Most of the samples used were generated with the MadGraph event generator [88]. MadGraph draws all Feynman diagrams for a given hard process, computes the matrix element of the process and uses this information to produce parton-level events. To generate Drell-Yan events with higher jet multiplicities, we used the Alpgen event generator which calculates the matrix element numerically (without making explicit use of Feynman diagrams) and can handle a large number of partons in the final state [89]. A third generator, Powheg, was used to assess differences in event generation and calculate the systematic uncertainties

[90]. The parton-level events are processed through the pythia Monte-Carlo generator

Dataset	No of Evt's	Xsec(pb)	$L(fb^{-1})$
Signal			
TTJets_FullLeptMGDecays_8TeV-madgraph-tauola	12119013	24.6	49.264
Non W/Z			
TTJets_SemiLeptMGDecays_8TeV-madgraph-tauola	24963676	103	256.843
TTJets_HadronicMGDecays_8TeV-madgraph	10537444	106.9	98.573
Single Top			
T_tW-channel-DR_TuneZ2star_8TeV-powheg-tauola	497658	11.1	44.834
Tbar_tW-channel-DR_TuneZ2star_8TeV-powheg-tauola	493460	11.1	44.457
VV			
WWJetsTo2L2Nu_TuneZ2star_8TeV-madgraph-tauola	1933235	5.8	333.316
WZ_TuneZ2star_8TeV_pythia6_tauola	10000283	33.2	301.123
ZZ_TuneZ2star_8TeV_pythia6_tauola	9799908	17.6	555.110
Z/γ			
DYJetsToLL_M-10To50filter_8TeV-madgraph	7132223	860.5	8.288
DYJetsToLL_M-50_TuneZ2Star_8TeV-madgraph-tarball	30459503	3503.7	8.694
WJets			
WJetsToLNU_TuneZ2Star_8TeV-madgraph-tarball	57709905	36257.2	1.592
QCD			
QCD_Pt_20_30_EMEnriched_TuneZ2star_8TeV_pythia6	35040695	29148.6	1.202
QCD_Pt_30_80_EMEnriched_TuneZ2star_8TeV_pythia6	33088888	4615893.0	0.007
QCD_Pt_80_170_EMEnriched_TuneZ2star_8TeV_pythia6	34542763	193294.9	0.188
QCD_Pt_20_MuEnrichedPt_15_TuneZ2star_8TeV_pythia6	21484602	134680.0	0.159
QCD_Pt_20_30_BCtoE_TuneZ2star_8TeV_pythia6	1740229	167388.0	0.010
QCD_Pt_30_80_BCtoE_TuneZ2star_8TeV_pythia6	2048152	167040.0	0.012
QCD_Pt_80_170_BCtoE_TuneZ2star_8TeV_pythia6	1945525	12981.9	0.2

Table 6.2: All data samples used in the analysis.

which performs the hadronization and showering of final state partons [91]. Because pythia's showering algorithm works in the limit of soft, collinear partons whereas the event generators are only reliable far from the soft and collinear limits, the showering sometimes results in extra jets. To avoid these, we use the MLM parton-jet matching algorithm which rejects events with showers that do not match partons from the matrix element calculation [92]. Tau particles decaying to hadrons result in jets that differ from other hadronic jets so hadronically decaying taus are handled separately by tauola [93]. The herwig Monte-Carlo is used to compute the systematic uncertainty due to hadronization and showering [94]. The final step of producing the signal and background samples is to simulate the CMS detector. This is accomplished using geant4 which simulates the passage of particles through matter [95]. After this point, the events from simulation and from data are treated in the same way: they are reconstructed with

the CMS Software Framework and the Physics Analysis Toolkit [96]. The signal and background samples are shown in Table 6.2.

6.3 Event cleaning

Only clean collision events can be used for data analysis. There are three different filters applied on the data to achieve this.

6.3.1 Beam Scraping

Prior to any requirements specific to $t\bar{t}$ events, we apply selections intended to eliminate events that result from the beam scraping against the beam pipe. Such events produce many tracks originating far from the nominal collision point. Therefore, we require at least 25% of all tracks in events with 10 or more tracks to be "high purity" tracks. "High purity" tracks are selected based on the χ^2 of the track, the track's impact parameters and the number of tracker layers with hits. The exact selection criteria is described in [97]. This requirement ensures the presence of high quality tracks near the interaction point.

6.3.2 Primary Vertex

We also require all valid primary vertices of the event to be less than 24 cm away from the nominal interaction point longitudinally and less than 2 cm away radially. Furthermore, each valid primary vertex must be associated with at least 4 tracks and the z position of the vertex used for the reconstruction of the $t\bar{t}$ system must be within 1 cm of any lepton used in the analysis.

6.3.3 HCAL Noise

Events are also rejected if they are found to have anomalous HCAL noise coming from HPDs or read-out boxes (RBXs) each of which contains four HPDs. The noise in the HPDs can originate from either the thermal emission of electrons which ionise a molecule in the HPD causing a small cascade or from an HPD discharge due to mis-alignment with the magnetic field. RBX noise is characterised by a high multiplicity of hits in all four HPDs. The best means of rejecting the noise using only HCAL is the pulse shape variable. HCAL reads out ten 25 ns time slices for each event. The pulse shape variable is the ratio of the energy in the two peak time slices to the energy in all ten. To reject the noise, we use a combination of the pulse shape variable, timing with respect to the

rest of the event, the hit multiplicity and lack of coincidence with ECAL. The details of this combination are described in [98].

6.4 Trigger

The distinguishing characteristic of dilepton $t\bar{t}$ events is the presence of two electrons, two muons or an electron and a muon. Thus, we can achieve a high trigger efficiency by using a combination of muon and electron triggers. The decay channels described in this thesis all contain at least two isolated leptons, which is represented in the triggers. For each channel the trigger is generally chosen such that it is unprescaled and its threshold is well below the cuts applied in further selection steps. During the data taking period the triggers are subject to change, i.e. their thresholds need to increase with an increasing instantaneous luminosity to limit the total output rate. Also triggers might not be fully optimised in the beginning, thus there can be several versions of a trigger with the same thresholds. A list of the triggers used is given as:

Double Muon:

*HLT_Mu17_Mu8_v**

OR

*HLT_Mu17_TkMu8_v**

Double Electron:

HLT_Ele17_CaloIdT_CaloIsoVL_TrkIdVL_TrkIsoVL_

*Ele8_CaloIdT_CaloIsoVL_TrkIdVL_TrkIsoVL_v**

Double Lepton:

*HLT_Mu17_Ele8_CaloIdT_CaloIsoVL_TrkIdVL_TrkIsoVL_v**

OR

*HLT_Mu8_Ele17_CaloIdT_CaloIsoVL_TrkIdVL_TrkIsoVL_v**

where the "*" is a wildcard for the different versions. The combined efficiency of these triggers for events that pass other analysis selections is more than 99%. CMS has a dedicated muon trigger subsystem which is located outside of the calorimeters and is rarely affected by particles other than muons. This makes muons easy to identify so the only changes needed to keep the muon trigger rate from growing were small increases in the p_T threshold. The highest single muon trigger p_T cut was at $17 \text{ GeV}/c$ which is well below the $20 \text{ GeV}/c$ cut used in our analysis and thus has no noticeable impact on our efficiency.

For the $e\mu$ channel, the trigger requires a muon with a transverse momentum of at least 8 GeV and an electron with a transverse momentum of at least 17 GeV or vice versa. On top of that the electron needs to fulfil loose identification criteria in the electromagnetic calorimeter.

In the ee channel, the trigger requires two electrons with transverse momenta greater 17 GeV and 8 GeV respectively. Also electron identification criteria is applied, as well as electrons are required to be loosely isolated in the calorimeter. A second trigger with the same momentum thresholds but different isolation and identification criteria is used to maximise the efficiency.

6.5 Event Selection

The events passing a dilepton triggers mentioned above, such as muon-plus-electron trigger, or a combination of single electron/muon triggers in the ee , $e\mu$, or $\mu\mu$ channels, respectively are selected. All three channels require at least two high p_T charged leptons, two high p_T jets, and topological requirements explained in the next sections.

6.5.1 Signal Signatures and Backgrounds

Muon-Electron Channel

The final state of $e\mu$ channel requires the presence of an isolated muon and electron of high transverse momenta, two b -jets with high p_T and due to the presence two neutrinos missing transverse energy. The main background whose signature is identical to that of signal process is $Z \rightarrow \tau\tau$ production along with two jets. One τ lepton decays into electron, the other to a muon. In addition to Z -boson we have di-boson production background as well, i.e. WW , WZ , and ZZ production along with two or more jets. The production signature of the two W bosons is identical to the signal as it's charged leptons have higher transverse momenta than the leptons coming from $Z \rightarrow \tau\tau$ decays. The ZZ and WZ production have smaller cross sections and the event yields are negligible as compared to the top quark dilepton production. instrumental fakes are another source of background, as they can originate from multijet production with a badly reconstructed jet which fakes a muon or an electron arising from W boson or semi-leptonic decay.

Dielectron Channel

The di-electron channel requires the presence of two high transverse momenta, isolated electrons, and rest of the constituents are same as $e\mu$ channel. In this channel the main

source of background is coming from Z plus two jets production, where Z decays into two electrons. the Invariant di-electron mass and missing transverse energy are selection variables which are very effective in suppressing this background, as no neutrinos are present in $Z \rightarrow ee$ final state. Event misreconstruction results in the observation missing transverse in this channel. Z production with physical missing transverse energy comes from the process $Z \rightarrow \tau\tau \rightarrow ee$ plus neutrinos. Also diboson production with two electrons in its final state makes it a background process to be considered in this case. In addition, instrumental background is also there, where one or two electrons can be faked by badly reconstructed jets of multijet production.

Dimuon Channel

The di-muon channel contains two high p_T muons in the final state. Since as compared to high p_T electrons these muons have a worse momentum resolution, so in this channel we have worst missing transverse energy resolution as well, due to which it is difficult to reject the main $Z \rightarrow \mu\mu$ plus jets background. In addition, diboson production, fake muon events and $Z \rightarrow \tau\tau \rightarrow \mu\mu$ plus neutrinos are other background processes to be considered. Muons with a fake isolation are referred as Fake muons, which come from semi-leptonic B -meson decays inside a b -jet. According to the identification criteria described previously, the number of misidentified muons, e.g. caused by punch through particles, are negligible.

6.5.2 Dilepton Selection

The selections criteria for $t\bar{t}$ dilepton channel is developed for the measurement of various top quark properties such as cross section and mass. Selections details can be seen in [99], [100] and [101] for the $e\mu$, ee and $\mu\mu$ channels respectively.

Common Selection

Common lepton identification criteria is used for all three dilepton channels as discussed in Sections 5.2 and 5.3. Also for data quality, primary vertex and jets, selection criteria is same for all channels:

- **Data Quality:** Data is only considered acceptable for analysis when the detector is fully operational. Luminosity blocks removed which are marked as bad.

- **Primary Vertex:** As discussed in section 6.3.2.
- Events with invariant mass $M_{ll} < 20 \text{ GeV}$ are removed for all dileptonic channels, with essentially no loss to the signal collected. Due to this requirement, we manage to suppress low-mass Z/γ^* Drell-Yan processes, as well as heavy-flavour resonance decays.
- **Jets:** Requirement is to have two or more jets with $p_T > 30 \text{ GeV}$ and $|\eta| < 2.5$.
- **b -jets:** The selection also requires one jet which is tagged as b -jet in an event. The b jets are identified by using algorithm called "Combined Secondary Vertex" (CSV) algorithm.

Channel specific selection criteria is described in next sections:

Muon-Electron Selection

Following selection criteria need to be fulfilled by the events in the $e\mu$ final state.

- **Muon:** The $e\mu$ final state should contain, one muon which should be isolated, which should have a timing cut against cosmic muons. The pseudorapidity and transverse momentum should be $|\eta| < 2.4$ and $p_T(\mu) > 20 \text{ GeV}$ respectively.
- **Electron:** One isolated electron having a transverse momentum and pseudorapidity of this electron is required to $p_T(e) > 20 \text{ GeV}$ and $|\eta| < 2.5$, respectively. The second loose electron in the event is vetoed, also this electron should not have a common track with a muon.
- Both leptons i.e Electron and muon should have opposite charges, in each event.
- Since in $e^\pm\mu^\mp$ mode, the background contamination is already small. So no missing transverse energy cut is applied.

Dimuon and Dielectron Selection

The dielectron selection criteria are:

- **Di-Muons:** Events requires, two muons of $p_T > 20 \text{ GeV}$, which should be isolated are required to be in region $|\eta| < 2.4$. Pair of muons should have opposite signed charges.

- **Di-Electrons:** The two opposite sign charged isolated electrons, of transverse momenta and pseudorapidities of $p_T > 20 \text{ GeV}$ and $|\eta| < 2.5$, respectively.
- **Invariant Dilepton Mass:** For the e^+e^- and $\mu^+\mu^-$ channels, the dilepton system's invariant mass is required to be outside $\pm 15 \text{ GeV}$ window, which is centered at the mass of the Z boson, to veto contributions from Z production. This requirement rejects almost 92% of Z/γ^* events, with the loss of approximately 24% of $t\bar{t}$ signal.
- **Missing Transverse Energy:** Neither the dominant background processes, Drell-Yan $Z/\gamma^* \rightarrow e^+e^-$, nor the difficult-to-model background from isolated lepton candidates produced in QCD multijet events, contain a natural source of large \cancel{E}_T . So the missing transverse energy criteria is to pass $\cancel{E}_T > 40 \text{ GeV}$ cut at the lost of 15 % of $t\bar{t}$ signal events.

6.5.3 Data MonteCarlo Comparison

This section presents the data to MC comparison distributions. Figures 6.1 show number of vertices on log scale both before and after pile-up reweighting, figure 6.2 show the p_T for electrons and muons of highest and second highest p_T . Figure 6.3 shows the dilepton invariant mass after the selection on jet multiplicity and MET. The jet multiplicity and the b -tagged jet multiplicity are shown in figure 6.4. Trigger and lepton scale factors discussed previously are applied to the simulated signal and backgrounds; however, all plots are normalised to the number of data events.

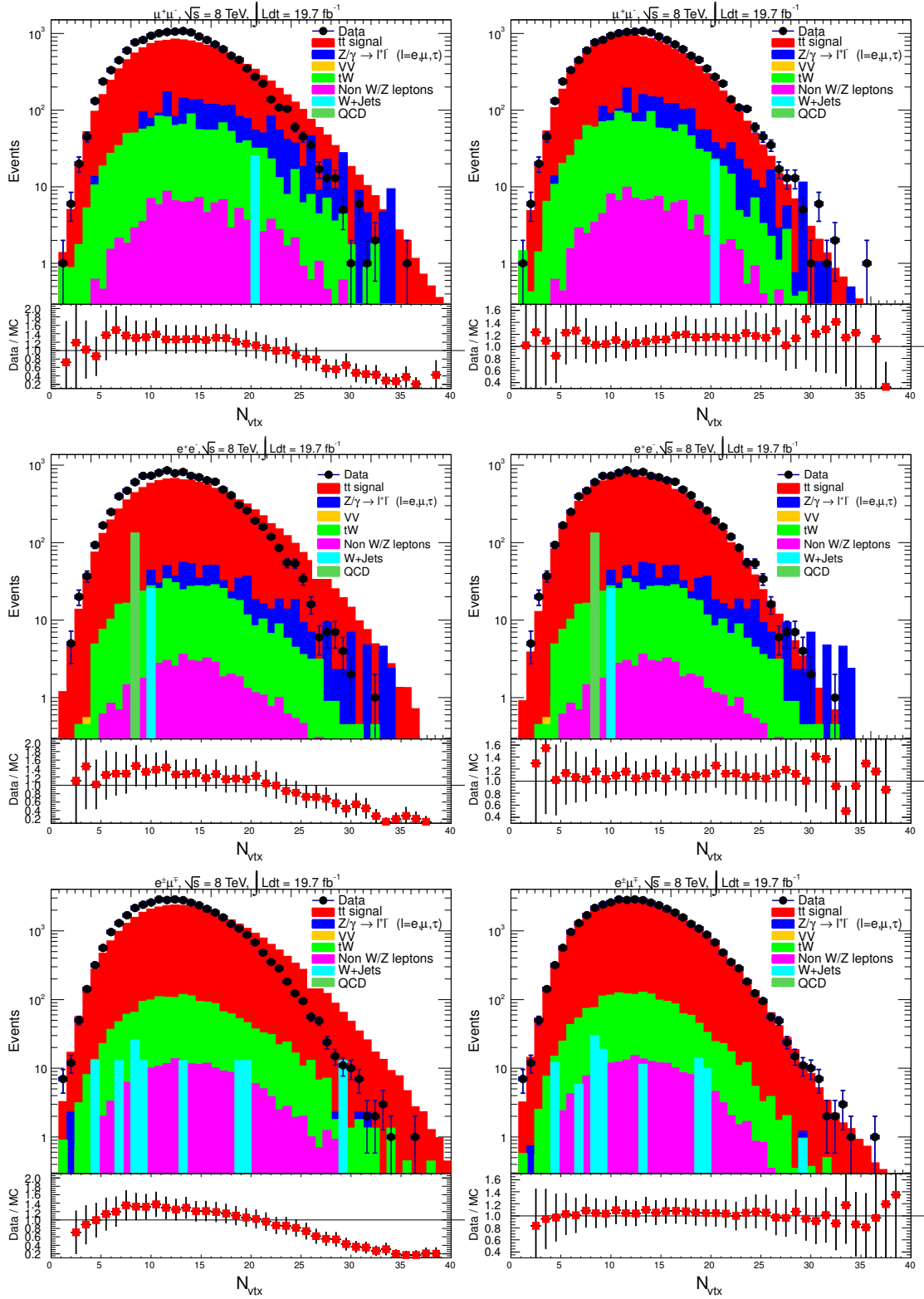


Figure 6.1: Distribution of the number of primary vertices in the $\mu^+\mu^-$, e^+e^- and $e^\pm\mu^\mp$ channels before and after pile-up reweighting. The plot is created after the selection of one isolated muon and one isolated electron with only an invariant mass requirement of 20 GeV.

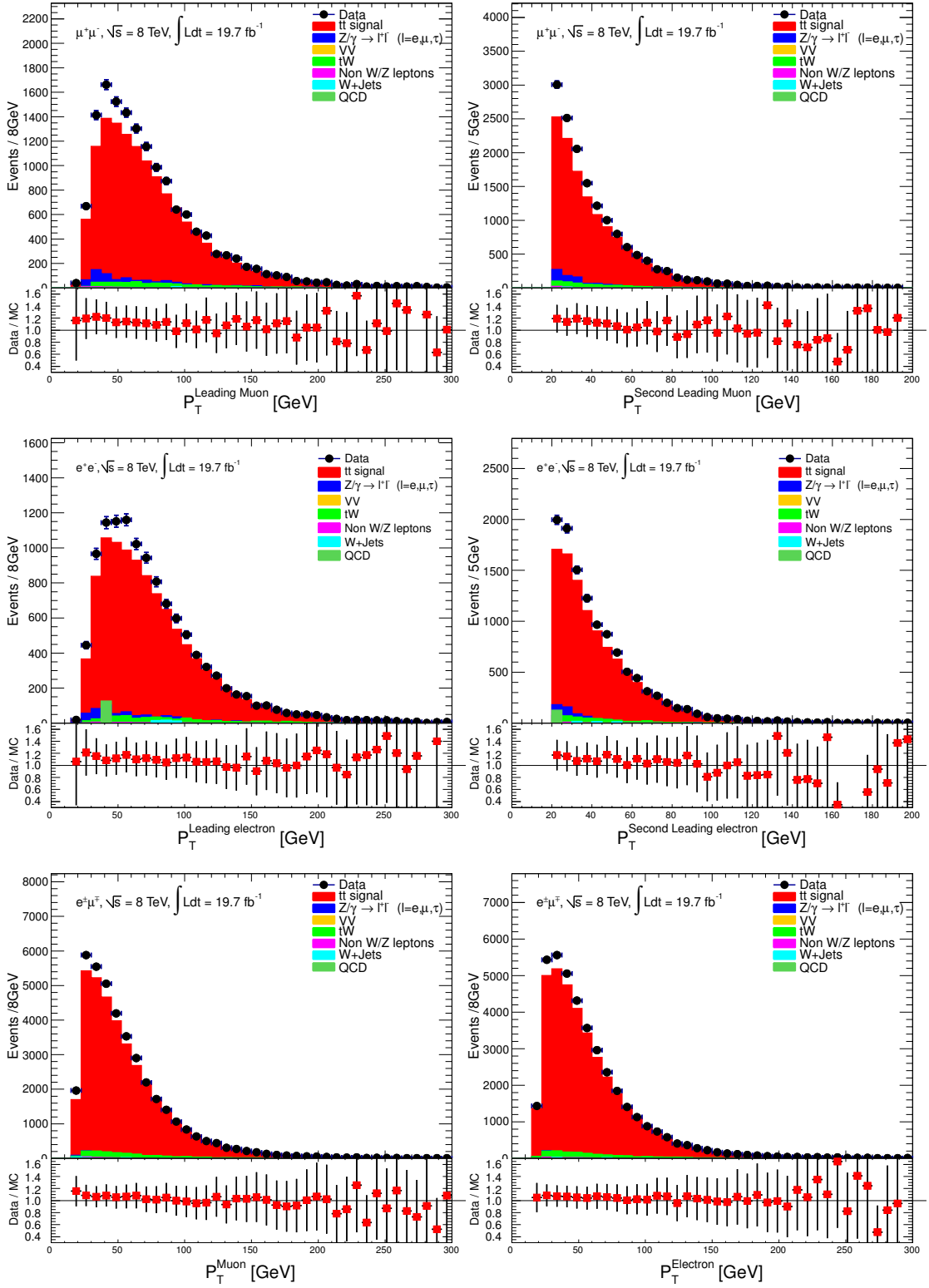


Figure 6.2: Transverse momentum p_T distributions of isolated leading lepton (left figures) and second leading (right figures) candidates for the $\mu^+\mu^-$, e^+e^- and $e^\pm\mu^\mp$ samples. For the $\mu^+\mu^-$ and e^+e^- channels, the events with $76 < m_{ll} < 106 \text{ GeV}$ and $\cancel{E}_T < 40 \text{ GeV}$ are rejected. The simulated samples are normalised to an integrated luminosity of 19.7 fb^{-1} . Scale factors for trigger selection are used.

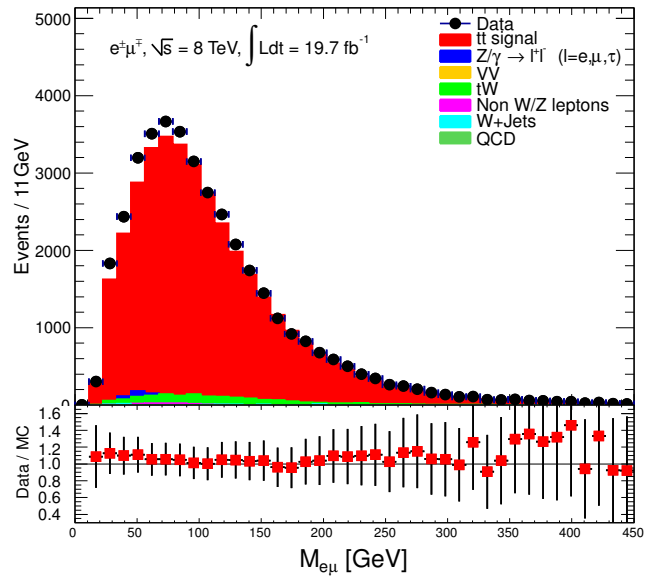
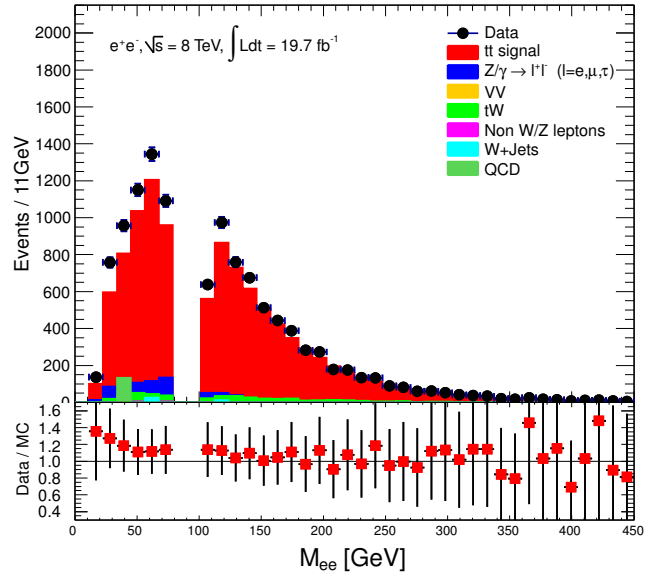
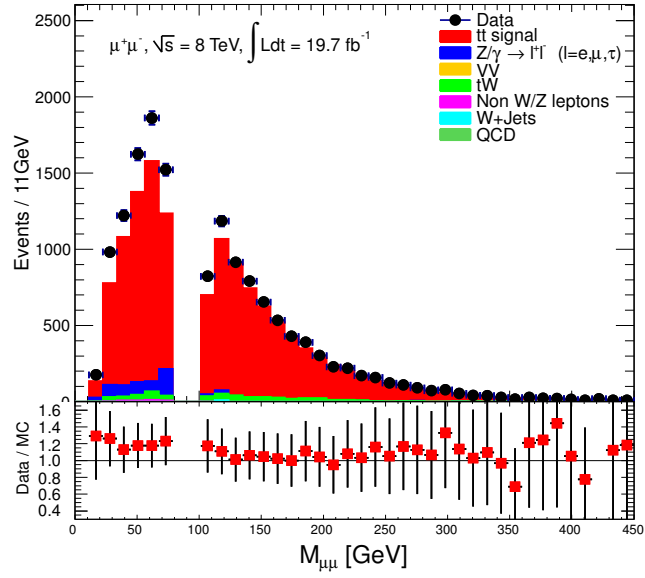


Figure 6.3: Dilepton mass for $\mu^+\mu^-$, e^+e^- and $e^\pm\mu^\mp$ channels. The Z+jets sample (blue area), for the $\mu^+\mu^-$ and e^+e^- channel, after⁹²all selection cuts, including $\cancel{E}_T > 40 \text{ GeV}$. For $e^\pm\mu^\mp$ channel no \cancel{E}_T cut is applied.

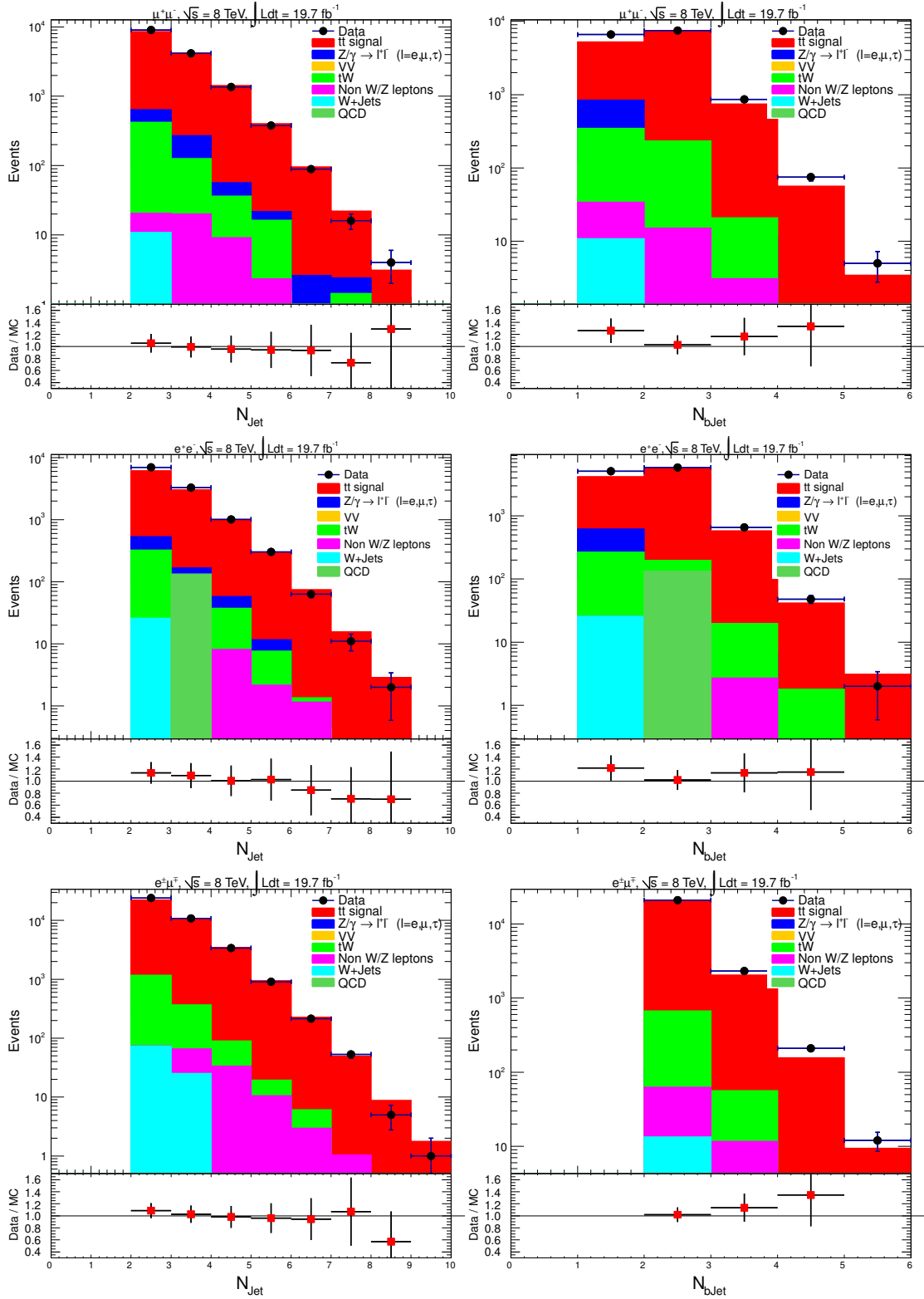


Figure 6.4: Number of b -tagged jets (CSVL) for the $\mu^+\mu^-$, e^+e^- and $e^+\mu^+$ isolated dilepton dijet samples after requiring at least one b -tagged jet. For the $\mu^+\mu^-$ and e^+e^- channels, the events with $76 < m_{ll} < 106 \text{ GeV}$ or $\cancel{E}_T < 40 \text{ GeV}$ are rejected. The simulated samples are normalised to an integrated luminosity of 19.7 fb^{-1} . Scale factors for trigger, lepton selection and b -tagging are used.

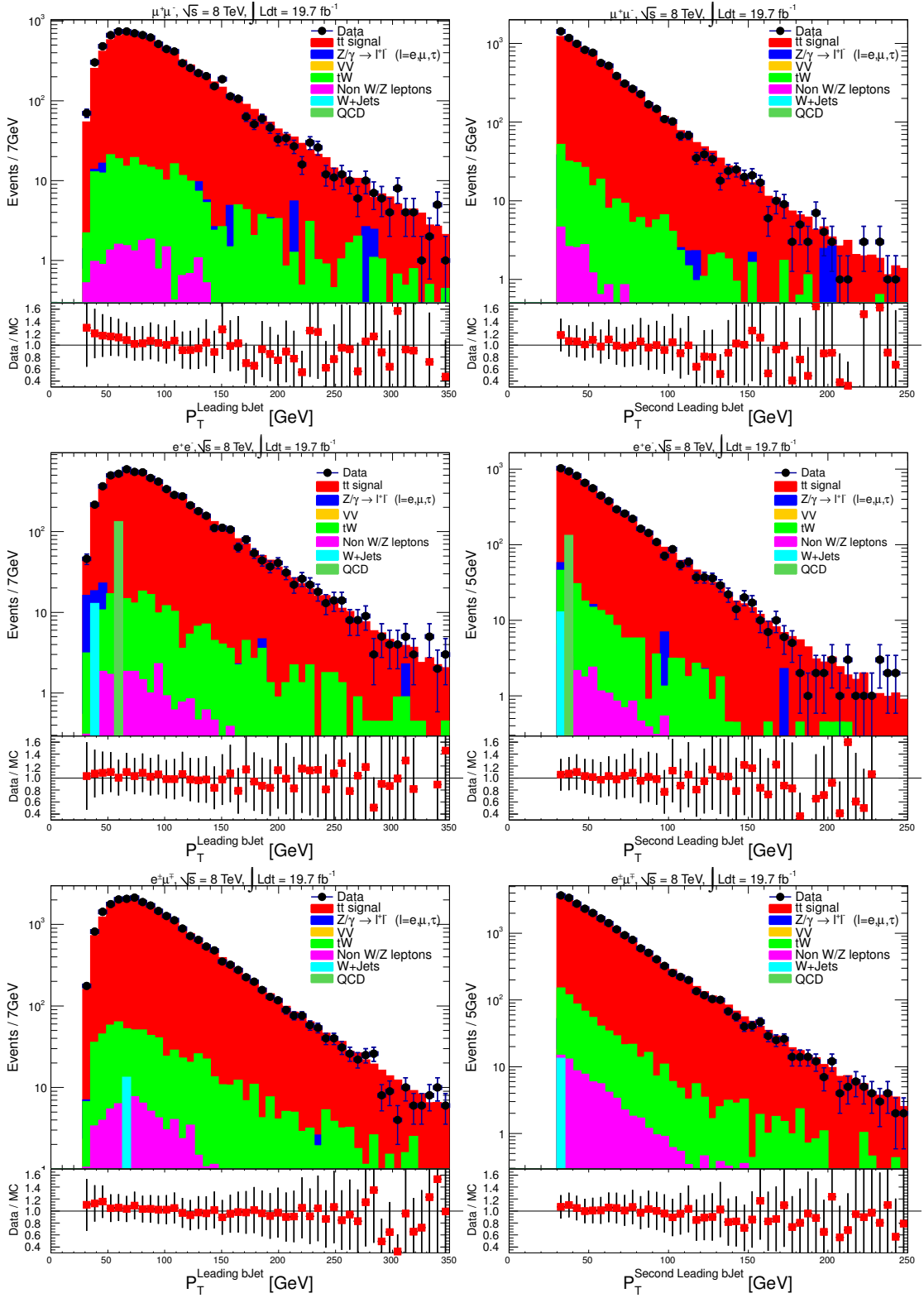


Figure 6.5: Transverse momentum p_T of b -jets for the $\mu^+\mu^-$, e^+e^- and $e^\pm\mu^\mp$ isolated dilepton dijet samples. For the $\mu^+\mu^-$ and e^+e^- channels, the events with $76 < m_{ll} < 106$ GeV and $\cancel{E}_T < 40$ GeV are rejected. The simulated samples are normalised to an integrated luminosity of 19.7 fb^{-1} . Scale factors for trigger and lepton selection are used.

6.5.4 Event Yield and Selection Summary

After the complete event selection the original goal to end with a highly signal dominated dataset has been reached successfully. The signal fraction is 92.8 % in the $e\mu$, 90.6 % in the $\mu\mu$ and 90.4 % in the ee channel. The cuts used to achieve this high purity are summarised in table 6.3 and the resulting event yields after several different selection steps can be found in table 6.4.

Channel	ee	$e\mu$	$\mu\mu$
Trigger	$p_T^{e1(e2)} > 17(8) \text{ GeV}$ isolation & id	$p_T^{l1(l2)} > 17(8) \text{ GeV}$ electron id	$p_T^{\mu1(\mu2)} > 17(8) \text{ GeV}$ or $p_T^{\mu1(\mu2)} > 8(17) \text{ GeV}$
Cleaning	no HCAL noise, no beam scraping, good primary vertex		
Lepton selection	quality cuts conv. rejection $I_{rel}^{PF}(\Delta R=0.3 < 0.2)$ $p_T > 20 \text{ GeV}$ $ \eta < 2.5$	one muon one electron	quality cuts global muon $I_{rel}^{PF}(\Delta R=0.4 < 0.15)$ $p_T > 20 \text{ GeV}$ $ \eta < 2.4$
Dilepton inv mass	$m_{ee} > 20 \text{ GeV}$ $ m_z - m_{ee} > 15 \text{ GeV}$	$m_{e\mu} > 20 \text{ GeV}$	$m_{\mu\mu} > 20 \text{ GeV}$ $ m_z - m_{\mu\mu} > 15 \text{ GeV}$
Jets	2 particle flow jets, anti- k_T with $R = 0.5$, loose jet id $p_T > 30 \text{ GeV}$, $ \eta < 2.4$		
Neutrinos	$\cancel{E}_T > 30 \text{ GeV}$	no cut	$\cancel{E}_T > 30 \text{ GeV}$
b tag	one b tagged jet, CSVL tagger with 10% misidentification rate		

Table 6.3: Summary of all cuts applied.

$\mu^+\mu^-$ sample	Total Events	Trigger	2 leptons	2 jets	\cancel{E}_T	b -tag
MC Signal	481463.59	31574.36	24437.69	17531.85	13740.48	12878.64
Non W/Z	4029462.10	171.32	116.95	94.20	67.21	55.40
tW	438382.95	3196.02	2467.07	865.64	685.67	613.57
VV	1118943.22	28010.25	6978.54	936.02	447.43	162.21
Z/γ^*	86184985.30	8838185.36	772306.96	28050.21	3223.01	1108.06
W +Jets	715827571.63	297.69	124.04	62.02	24.81	12.40
QCD	107278930078	3104.87	2111.31	248.39	0	0
Total MC	108087010887	8904539.88	808542.56	47788.33	18188.61	14830.29
Data	102393963	8671119	824589	48853	18542	14964
$\mu^\pm e^\mp$ sample	Total Events	Trigger	2 leptons	2 jets	\cancel{E}_T	b -tag
MC Signal	482268.19	54579.52	-	39244.01	-	36817.66
Non W/Z	4509499.71	327.31	-	269.99	-	225.19
tW	439115.55	5568.66	-	1929.97	-	1700.39
VV	1120813.13	13421.48	-	1155.51	-	406.46
Z/γ^*	86329012.47	39117.91	-	1800.50	-	630.38
W +Jets	717023819.66	1838.84	-	198.79	-	111.82
QCD	140168929992.43	2736.86	-	0	-	0
Total MC	140978834521.14	117590.58	-	44598.77	-	39891.9
Data	56453239	114659	-	43862	-	39193
e^+e^- sample	Total Events	Trigger	2 leptons	2 jets	\cancel{E}_T	b -tag
MC Signal	482390.09	24804.23	19184.39	13759.90	10790.24	10110
Non W/Z	4511560.12	127.26	102.11	85.64	62.44	54.29
tW	439226.55	2483.95	1934.86	695.43	544.73	480.89
VV	121096.45	21021.05	5050	710.65	4153.08	123.93
Z/γ^*	86298109.66	6582905.75	565108.65	21139.32	2361.16	763.07
W +Jets	717205069.36	1516.19	1081.22	99.42	62.14	37.28
QCD	107485371530	370.81	370.81	132.78	132.78	132.78
Total MC	108295032510	6633215.40	592820.56	36375.41	14285.29	11696.36
Data	96087783	6365742	591358	37595	14527	11589

Table 6.4: Event selection yields in the different channels after each selection cut. The expected number of events in simulation corresponds to the luminosity of the data, and correction factors have been applied.

Chapter 7

Background Determination and Systematic Uncertainties

7.1 Drell-Yan

The most important background in the ee and $\mu\mu$ channels is the contribution by Drell-Yan events. Therefore this analysis does not purely rely on the simulation for this process. Instead, the normalization is determined from the data by scaling the DY contribution to the measured Z mass peak [102, 103].

For this method to work, the events which were cut out by the dilepton invariant mass cut ($|m_Z - m_{ll}| > 15 \text{ GeV}$) are used. The further requirements of two jets and missing transverse energy are also applied to these events. Then the number of Drell-Yan events in the $|m_Z - m_{ll}| \leq 15 \text{ GeV}$ region is determined in data and the simulation. The simulation is then scaled to the data such that the number of events inside the Z mass peak is the same for data and simulation.

To calculate the number of observed DY events outside the Z veto $N_{out}^{l^+l^-,obs}$, the following formula is used (for $ll = ee$ or $\mu\mu$):

$$N_{out}^{l^+l^-,obs} = R_{out/in}^{l^+l^-,MC} (N_{in}^{l^+l^-} - \frac{1}{2} N_{in}^{e\mu} k_{ll}) \quad (7.1)$$

The ratio $R_{out/in}^{l^+l^-,MC}$ of events outside the Z mass region $N_{DY,MC}^{out}$ over the number of events inside the Z peak $N_{DY,MC}^{in}$ is taken from the DY simulation:

$$R_{out/in}^{l^+l^-,MC} = \frac{N_{DY,MC}^{l^+l^-,out}}{N_{DY,MC}^{l^+l^-,in}} \quad (7.2)$$

To account for the non- DY events in the number of measured events inside the DY peak region $N_{in}^{l^+l^-}$, the number of events from other processes has to be subtracted. This in number, $N_{in}^{e\mu}$, is determined in the $e\mu$ channel which does not contain DY events. Due

to the higher combinatorics for the $e\mu$ channel, a factor of $\frac{1}{2}$ has to be applied here. In addition, the differences between the selection efficiencies in the ee and $\mu\mu$ channels need to be taken into account. This is done using the k_{ll} factors:

$$k_{ee} = \sqrt{\frac{N_{in,loose}^{e^+e^-}}{N_{in,loose}^{\mu^+\mu^-}}} \quad (7.3)$$

$$k_{\mu\mu} = \sqrt{\frac{N_{in,loose}^{\mu^+\mu^-}}{N_{in,loose}^{e^+e^-}}} \quad (7.4)$$

These factors are determined with a looser selection, i.e. without the missing energy cut applied to keep a larger amount of events. This is justified because the selection efficiency for muons and electrons should not depend on the missing energy in the event. On the other hand the k_{ll} factors need to be calculated from events as close to the final selection as possible, therefore removing further cuts introduces larger uncertainties.

Channel	$\mu^+\mu^-$	e^+e^-
DY MC	1108.25	767.35
Estimate from data	1615.31	1057.06
$R_{out/in}$	0.16 ± 0.005	0.14 ± 0.008
c_{DY}	1.46 ± 0.07	1.38 ± 0.06

Table 7.1: Data-driven Drell-Yan background estimation in the $\mu\mu$ and ee channels after the missing transverse energy cut.

The final scaling factor c_{DY} for the simulation can be calculated by dividing the contributions from data by the ones from simulation:

$$c_{DY} = \frac{DY_{data}}{DY_{MC}} \quad (7.5)$$

The resulting values can be found in table 7.1.

7.1.1 Scale factors at different selection steps

The agreement between data and simulation looks good and the scale factor is consistent with 1 before the missing energy cut. Table 7.2 shows the scale factors determined at the later steps.

One can still see increasing scale factors when tightening the cuts. This is probably caused by mismeasured leptons in DY events which migrate out of the Z peak. Note that these events must have initial and/or final state radiation to survive the jet cuts as

Channel $\mu^+\mu^-$	DY_{MC}	DY_{DD}	SF_{DY}	$R_{out/in}$
$\geq 2\text{Jets}$	28032.38	27190.69	0.97 ± 0.008	0.12 ± 0.0008
$\geq 2\text{Jets}+0\text{bjet}$	18430.27	15869.09	0.86 ± 0.009	0.12 ± 0.0001
$\geq 2\text{Jets}+1\text{bjet}$	9602.11	10378.14	1.08 ± 0.02	0.11 ± 0.0001
$\geq 2\text{Jets}+2\text{bjets}$	1367.28	1849.82	1.35 ± 0.05	0.11 ± 0.003
$\geq 2\text{Jets}+E_T$	3221.30	3846.15	1.19 ± 0.03	0.16 ± 0.003
$\geq 2\text{Jets}+E_T+0\text{bjet}$	2113.05	2231.00	1.06 ± 0.03	0.16 ± 0.004
$\geq 2\text{Jets}+E_T+1\text{bjet}$	1108.25	1615.31	1.46 ± 0.07	0.16 ± 0.005
$\geq 2\text{Jets}+E_T+2\text{bjets}$	174.00	288.56	1.66 ± 0.16	0.15 ± 0.012
Channel e^+e^-	DY_{MC}	DY_{DD}	SF_{DY}	$R_{out/in}$
$\geq 2\text{Jets}$	20910.86	20773.14	0.99 ± 0.10	0.12 ± 0.001
$\geq 2\text{Jets}+0\text{bjet}$	13835.49	12295.15	0.89 ± 0.01	0.12 ± 0.002
$\geq 2\text{Jets}+1\text{bjet}$	7085.37	7771.49	1.10 ± 0.02	0.11 ± 0.002
$\geq 2\text{Jets}+2\text{bjets}$	1070.531	1375.18	1.28 ± 0.05	0.11 ± 0.005
$\geq 2\text{Jets}+E_T$	2369.42	2734.19	1.15 ± 0.03	0.15 ± 0.005
$\geq 2\text{Jets}+E_T+0\text{bjet}$	1062.06	1708.39	1.07 ± 0.04	0.16 ± 0.006
$\geq 2\text{Jets}+E_T+1\text{bjet}$	767.35	1057.06	1.38 ± 0.06	0.14 ± 0.008
$\geq 2\text{Jets}+E_T+2\text{bjets}$	149.107	241.49	1.62 ± 0.17	0.16 ± 0.02

Table 7.2: Drell-Yan scale factors after different selection steps, both for ee and $\mu\mu$ channels.

well as missing energy, i.e. already a mismeasured transverse momentum balance, this imbalance might be caused by a mismeasured lepton. It seems that this effect is a bit larger in the data than in the simulation, and the ee channel is slightly more affected than the $\mu\mu$ channel. However the scale factors determined after the E_T^{miss} cut, after b tagging and after the kinematic reconstruction are all compatible within their uncertainties. It was chosen to apply the scale factor determined after the E_T^{miss} cut, i.e. when it first becomes different from 1, and take the differences in the further steps into account for the uncertainty.

7.2 Systematic uncertainties

The $t\bar{t}$ cross section ($\sigma_{t\bar{t}}$) measurement is affected by several systematic uncertainties, listed below.

7.2.1 Luminosity

The luminosity value used in this analysis is originating from the absolute calibration of the luminosity measured at the CMS experiment. A value of $\pm 2.6\%$ is taken as flat rate uncertainty [104].

7.2.2 Pile-up

As discussed in Section 5.8.1, the LHC can attain higher instantaneous luminosities by increasing the proton density of the colliding bunches. However, this also increases the number of interactions in a single bunch crossing which causes extra particles in the event. This phenomenon is referred to as "pile-up" and it can be studied by measuring the number of primary vertices in each event. To estimate the impact from pile-up on the signal selection efficiency, the simulated pile-up distribution is varied $\pm 5\%$ with respect the nominal value, and the cross section is recalculated. The systematic uncertainty due to pile-up is measured to be $\pm 0.5 \text{ GeV}/c^2$ for all channels.

7.2.3 Trigger

The trigger efficiency is measured by using those triggers which are only weakly correlated to dilepton triggers, as described in Ref.[105]. A dependence on pseudorapidity of the muon and electron of a few percent is observed and SFs are derived. Uncertainties in the inclusive cross section of 0.7% in the $\mu^+\mu^-$ channel, 0.4% in the e^+e^- and 0.2% in the $e^\pm\mu^\mp$ channel.

7.2.4 Lepton

The isolation and identification efficiencies for leptons (electrons or muons) are estimated by using "tag-and-probe" method with Z -boson event samples as a function of p_T and pseudorapidity [105], and are found to be above 95% (90%). The muon efficiency is well described in the simulation, i.e. with residual scale factors being very close to unity. Uncertainties in the inclusive cross section of around 1% are found for all three channels.

7.2.5 Jet Energy Resolution

The jet energy resolution in the simulation is increased by factors of 1.079, 1.099, 1.121, 1.208, 1.254, 1.395, 1.056 in the eta ranges (0.0, 0.5, 1.1, 1.7, 2.3, 5.0) according the prescription given by the Jet/MET group.

The error on the inclusive cross section amounts to $\mu^+\mu^-$: 2.3%, e^+e^- : 2.3%, $e^\pm\mu^\mp$: 2.3% for the individual dilepton channels.

7.2.6 Backgrounds

A large source of systematic uncertainty is the contribution from background events to the final sample. The background determination has been described in Section 7.1. The uncertainty due to background normalization is determined by variation of the backgrounds. In e^+e^- and $\mu^+\mu^-$ channels, background from Z +jets processes is by far dominant, and its normalization is varied by $\pm 30\%$. The effect on the inclusive cross section is of the order of 3.4% in $\mu^+\mu^-$, 2.9% in e^+e^- channel and 0.8% in the $e^\pm\mu^\mp$ channel.

The contribution from backgrounds originating from diboson, and single-top tW production are estimated from the simulation. Each source is varied up and down by $\pm 30\%$. The resulting uncertainty on the total cross section measurement is about 1.9% in $\mu^+\mu^-$, 2.4% in e^+e^- , and 1.9% in the $e^\pm\mu^\mp$ channel.

7.2.7 Top Quark Mass

For the uncertainty due to top quark mass, which in the default sample is 172.5 GeV , two samples with a top quark mass of 161.5 GeV and 184.5 GeV are used to estimate the impact of the top mass uncertainty on the signal selection efficiency. The averaged differences of the up and down variations to the default, scaled by 1/12, are used to estimate the systematic uncertainty measurement.

7.2.8 Hard Scattering Q^2 Scale

The uncertainty due to the choice of Q^2 on generator level is studied by increasing and decreasing it by a factor of 4 w.r.t default value. The impact on the selection efficiency is small. The systematic uncertainty is estimated by taking averaged differences of up and down variations to the default.

7.2.9 Matching Scale

The effect of additional jet production in MADGRAPH is studied by varying the threshold between jet production on matrix-element level and through parton showering (matching scale). The systematic uncertainty is estimated individually by taking the averaged differences of the up and down variations to the default.

7.2.10 ISR and FSR

The uncertainty due to initial and final state radiation on signal efficiency is covered by the uncertainty on the Q^2 and matching scales.

7.2.11 Summary

The breakdown of systematic uncertainties for the absolute inclusive cross section measurement is shown in table 7.3. The quadratic sum of all the sources of uncertainty yields the total uncertainty of approximately 6%.

source	$\mu^+\mu^-$	e^+e^-	$e^\pm\mu^\mp$
Trigger efficiency	0.7	0.4	0.2
Pile-up	0.5	0.5	0.5
Lepton	1.1	1.0	1.0
Jet energy resolution	2.3	2.3	2.3
Backgrounds (Z +jets $\rightarrow \mu\mu/ee$)	3.4	2.9	0.8
Backgrounds (other)	1.9	2.4	1.9
Q^2 Scale	3.9	2.6	2.1
ME/PS Matching	0.4	0.2	0.2
Top quark mass	1.0	1.0	0.8
Luminosity	2.6	2.6	2.6
Total	6.8	6.0	4.8

Table 7.3: Summary of the systematic uncertainties for the measurement of the inclusive $t\bar{t}$ cross section. The contribution from non- Z +jets backgrounds is referred to as background (other).

Chapter 8

Cross-section

In particle physics, the cross section is the probability of a given interaction to occur. The number of events produced in a process is luminosity times cross section. The Cross sections are very useful in determining the relative rates of interactions and for tests of the Standard Model, since any significant disagreement from the theoretical Standard Model cross section points to new physics sources, or can point to new physics by providing a measurement of couplings to other particles. Thus, the measurement of cross sections is important in testing the Standard Model. Cross section measurements are also necessary for determining the background contribution of a process to new physics sources.

The $t\bar{t}$ dilepton channel presents a clean final state, therefore a simple counting experiment is used to compute cross section. Events observed in the data that pass specific selections are compared with expected background estimates and the excess is attributed to the $t\bar{t}$ dilepton production. The $t\bar{t}$ production cross section is measured by using the following expression:

$$\sigma_{t\bar{t}} = \frac{N - B}{A.L} \quad (8.1)$$

where N is the number of events observed in data, B is the number of events in background processes, total acceptance including geometric acceptance and the efficiency of event selection is given as A and integrated luminosity used to normalize the sample is L .

The $t\bar{t}$ signal yields reported in Section 6.5.3 are corrected with a scale factor, that is computed as the product of the individual scale factors that has been discussed previously and that account for the differences in lepton efficiencies, branching ratio and pile-up effect. The combination of all these contributions yields the following scale factors per channel:

- $\mu^+\mu^-$ final state $\rightarrow SF_{all}^{\mu\mu} = 0.939 \pm 0.152$

- e^+e^- final state $\rightarrow SF_{all}^{ee} = 0.923 \pm 0.149$
- $e^\pm\mu^\mp$ final state $\rightarrow SF_{all}^{e\mu} = 0.915 \pm 0.149$

A comparison summary between events observed in data to that of the expected number of signal and background is given in table 8.1. As can be observed, a good agreement is present between expectation and events in data in all three channels. The expected signal events are corrected as described above. A summary of the $t\bar{t}$ signal production

Source	e^+e^-	$\mu^+\mu^-$	$\mu^\pm e^\mp$
Dilepton $t\bar{t}$	10110	12878.64	36817.66
Non W/Z	54.29	55.40	225.19
tW	480.89	613.57	1700.39
VV	123.93	162.21	406.46
Z/γ^*	763.07	1108.06	630.38
W +Jets	37.28	12.40	111.82
QCD	132.78	0	0
Total MC	11696.36	14830.29	39891.9
Data	11589	14964	39193

Table 8.1: Expected signal and background contributions compared to the number of events observed in data passing full signal selection with at least one b-tagged jet required.

Channel	e^+e^-	$\mu^+\mu^-$	$e^\pm\mu^\mp$
Events in data	11589	14964	39193
All backgrounds	1774.70	1794.13	3201.91
Total acceptance	0.20 ± 0.02	0.27 ± 0.03	0.72 ± 0.07
Cross section [pb]	244.36 ± 2.47	238.51 ± 2.13	253.77 ± 1.34

Table 8.2: Summary of $t\bar{t}$ signal production cross section measured in separate event selection channels. The number of events observed in data, the total background expectations, the total signal acceptance (includes geometric detector acceptance and event selection efficiency) with systematic uncertainties, and the cross section measurements are shown separately. The uncertainties on the cross section include statistical only.

cross section measured in separate event selection channels is shown in table 8.2. The number of events observed in data, the total background expectations, the total signal acceptance (includes geometric detector acceptance and event selection efficiency) with systematic uncertainties, and the cross section measurements are shown separately. The uncertainties on the cross section include statistical only.

8.1 Combination of results

The cross sections values for the three $\mu^+\mu^-$, e^+e^- and $\mu^\pm e^\mp$ channels are combined based on the statistical error of the measurement. Since the three results are statistically independent, the combination proceeds by computing the error weighted mean for each cross section measurement.

The combined cross section is thus given by:

$$\sigma = \frac{\sum \frac{\sigma_i}{\delta\sigma_i^2}}{\sum \frac{1}{\delta\sigma_i^2}} \quad (8.2)$$

where σ_i are the cross section results in the different decay channels with $i = \mu^+\mu^-$, e^+e^- and $\mu^\pm e^\mp$, and $\delta\sigma_i$ are their corresponding uncertainties. The statistical uncertainty on the combined cross section is:

$$\delta\sigma = 1/\sqrt{\sum \frac{1}{\delta\sigma_i^2}} \quad (8.3)$$

The total systematic uncertainties of all three channels are combined by using equation 8.3.

8.2 Conclusion

The work discussed in this part of the thesis presents a $t\bar{t}$ cross section measurement for all three final states ($\mu^+\mu^-$, $e^\pm\mu^\mp$, e^+e^-), in which each event contained two leptons having opposite signs, two high P_T jets and transverse missing energy, and by using the b -tagging, required at least on b -jet. So the production cross section from $t\bar{t}$ dileptonic final state, corresponding to top mass of 172.5 GeV , is

$$\sigma_{t\bar{t}} = 248.53 \pm 1.03(\text{stat.}) \pm 8.20(\text{syst.}) \text{ pb}$$

which is in agreement with standard model predictions.

The LHC is scheduled to resume collisions in 2015 at a center of mass energy of 13 TeV and will then be increased to the design c.m.s energy of 14 TeV [108]. The inclusive cross section for top pairs will increase at this center of mass energy. The expected NNLO inclusive cross section for top pair production for 14 TeV is $953.6_{-33.9}^{+22.7+16.2}_{-17.8} \text{ pb}$ [109].

Bibliography

- [1] LHC Study Group, "The Large Hadron Collider: conceptual design", Technical Report CERN-AC-95-05 LHC, CERN, Geneva, (Oct, 1995).
- [2] ALICE Collaboration, "Heavy ion collisions at the LHC: The Alice experiment", arXiv:hep-ph/9612221.
- [3] ALICE Collaboration, "ALICE technical design report: Detector for high momentum PID", CERN-LHCC-98-19, (1998).
- [4] ATLAS Collaboration, "ATLAS: Detector and physics performance technical design report. Volume 1", CERN-LHCC-99-14, ATLAS-TDR-14, (1999).
- [5] ATLAS Collaboration, "ATLAS: Detector and physics performance technical design report. Volume 2", CERN-LHCC-99-15, ATLAS-TDR-15, (1999).
- [6] CMS Collaboration, "CMS Physics: Technical Design Report Volume 1: Detector Performance and Software", Technical Design Report CERN-LHCC-2006-001, CMS-TDR-008-1, Geneva, (2006).
- [7] CMS Collaboration, "CMS technical design report, volume II: Physics performance", J.Phys. G34 (2007) 995D1579. doi:10.1088/0954-3899/34/6/S01.
- [8] LHCb Collaboration, "LHCb technical design report: Reoptimized detector design and performance", CERN-LHCC-2003-030, (2003).
- [9] C. Lefvre, "The CERN accelerator complex - Complexe des accelerateurs du CERN", (Dec, 2008). <http://cdsweb.cern.ch/record/1260465>.
- [10] M. Lamont, "Status of the LHC", J.Phys.Conf.Ser. 455 (2013) 012001. doi:10.1088/1742-6596/455/1/012001.
- [11] CMS Collaboration, "CMS 3D Image for Inclusion in Presentations". <https://cms-docdb.cern.ch/cgi-bin/DocDB/ShowDocument?docid=2716>.

- [12] P. M. Nadolsky, H.-L. Lai, Q.-H. Cao et al., "Implications of CTEQ global analysis for collider observables", *Phys. Rev. D* 78 (2008) 013004, arXiv:0802.0007. doi:10.1103/PhysRevD.78.013004.
- [13] J. Alwall, M. Herquet, F. Maltoni et al., "MadGraph 5: going beyond", *JHEP* 06 (2011) 128, arXiv:1106.0522. doi:10.1007/JHEP06(2011)128.
- [14] P. Artoisenet, R. Frederix, O. Mattelaer et al., "Automatic spin-entangled decays of heavy resonances in Monte Carlo simulations", *JHEP* 03 (2013) 015, arXiv:1212.3460. doi:10.1007/JHEP03(2013)015.
- [15] T. Sjostrand, S. Mrenna, and P. Z. Skands, "pythia 6.4 Physics and Manual", *JHEP* 05 (2006) 026, arXiv:hep-ph/0603175. doi:10.1088/1126-6708/2006/05/026.
- [16] CMS Collaboration, "Measurement of the Underlying Event Activity at the LHC with $\sqrt{s} = 7 \text{ TeV}$ and Comparison with $\sqrt{s} = 0.9 \text{ TeV}$ ", *JHEP* 1109 (2011) 109, arXiv:1107.0330. doi:10.1007/JHEP09(2011)109.
- [17] LHC, "LHC Programme Coordination web pages", 2012.
- [18] P. Nason, "A New method for combining NLO QCD with shower Monte Carlo algorithms", *JHEP* 0411 (2004) 040, arXiv:hep-ph/0409146. doi:10.1088/1126-6708/2004/11/040.
- [19] CMS Collaboration, "Alignment of the CMS Silicon Tracker during Commissioning with Cosmic Rays", *JINST* 5 (2010) T03009, arXiv:0910.2505. doi:10.1088/1748-0221/5/03/T03009.
- [20] CMS Collaboration, "Public CMS Data Quality Information", 2013.
- [21] CMS Collaboration, "Muon Project", CERN/LHCC 94-138, 15 December 1997.
- [22] Prozessvisualisierungs- und Steuerungssystem (PVSS), www.pvss.com.
- [23] CMS Collaboration. The CMS muon project: Technical Design Report. Technical Design Report CMS. CERN, Geneva, 1997.
- [24] Stuart A. Boyer, SCADA: Supervisory Control and Data Acquisition, ISA, The Instrumentation, Systems and Automation Society (2004).
- [25] F. Wagner et al., Modeling Software with Finite State Machines: A Practical Approach (2006).

- [26] <http://www.etm.at>
- [27] Bunkowski, K. et al. Radiation tests of cms rpc muon trigger electronic components. Nucl. Instrum. Meth., A538:708D717, 2005.
- [28] CAEN S.p.A. Costruzioni Apparecchiature Elettroniche Nucleari,. http://www.caen.it/nuclear/easy_info.php.
- [29] OPC Foundation. <http://www.opcfoundation.org>.
- [30] Aielli, G. et al. RPC operation at high temperature. Nuclear Instruments and Methods in Physics Research A, 508:44D49, August 2003.
- [31] Adolphi, R. et al. The CMS experiment at the CERN LHC. JINST, 0803:S08004, 2008.
- [32] B. Franek and C. Gaspar. SMI++: Object oriented framework for designing and implementing distributed control systems. Presented at 2004 IEEE Nuclear Science Symposium and Medical Imaging Conference (NSS / MIC), Rome, Italy, 16-22 Oct 2004.
- [33] Colaleo, A. et al. First measurements of the performance of the Barrel RPC system in CMS. Nuclear Instruments and Methods in Physics Research Section A: Accelerators, Spectrometers, Detectors and Associated Equipment, 609(2-3):114 D 121, 2009.
- [34] Tevatron Electroweak Working Group Collaboration, "Combination of CDF and $D\bar{D}$ results on the mass of the top quark using up to $8.7 fb^{-1}$ at the Tevatron", arXiv:1305.3929.
- [35] CDF Collaboration, "Observation of Top Quark Production in $P\bar{p}$ -P Collisions", Phys.Rev.Lett. 74 (1995) 2626D2631, doi:10.1103/PhysRevLett.74.2626, arXiv:9503002.
- [36] $D\bar{D}$ Collaboration, "Observation of the Top Quark ", Phys.Rev.Lett. 74 (1995) 2632D2637, doi:10.1103/PhysRevLett.74.2632, arXiv:9503003.
- [37] C. Amsler et al. Review of particle physics. Phys. Lett., B667:1, 2008.
- [38] L. Montanet et al. Review of particle properties. Phys. Rev. D, 50:1433, 1994.

- [39] *DØ* Collaboration, "A Direct Measurement of the Total Decay Width of the Top Quark", arXiv:1308.4050.
- [40] M. Czakon et al., "The total top quark pair production cross-section at hadron colliders through $O(\alpha_S^4)$ ", arXiv:1303.6254.
- [41] M. Czakon et al., "Constraints on the gluon PDF from top quark pair production at hadron colliders", arXiv:1303.7215.
- [42] Tevatron Electroweak Working Group, "Combination of the $t\bar{t}$ production cross section measurements from the Tevatron Collider", *DØ* Note 6363 and CDF Note 10926 (2012).
- [43] CMS Collaboration, "Measurement of the $t\bar{t}$ production cross section in the dilepton channel in pp collisions at $\sqrt{s} = 7 \text{ TeV}$ ", JHEP 11 (2012) 67, doi:10.1007/JHEP11(2012)067, arXiv:1208.2671.
- [44] CMS Collaboration, "Top pair cross section in dileptons", CMS Physics Analysis Summary CMS-PAS-TOP-12-007, (2012).
- [45] J. M. Campbell, R. Frederix, F. Maltoni et al.: Next-to-Leading Order Predictions for t-Channel Single-Top Production at Hadron Colliders. Phys. Rev. Lett., 102(182003), 2009. arXiv:0903.0005. doi:10.1103/PhysRevLett.102.182003.
- [46] J. M. Campbell and F. Tramontano: Next-to-leading order corrections to Wt production and decay. Nuclear Physics B, 726(109), 2005. arXiv:0506289.
- [47] J. M. Campbell, R. K. Ellis, and F. Tramontano: Single top production and decay at next-to-leading order. Physics Review D, 70(094012), 2004. arXiv:hep-ph/0408158.
- [48] Yao, W. et al.: Review of Particle Physics. Journal of Physics G, 33, 2006.
- [49] Collaboration, P. D. G.: Particle Physics Group, volume 37. Journal of Physics G, 2010.
- [50] CMS Physics Technical Design Report: Detector performance and software. No. v.1 in CMS Technical design report. CERN, 2006.
- [51] P. Lenzi, C. Genta, and B. Mangano, "Track reconstruction of real cosmic muon events with CMS tracker detector", J. Phys. Conf. Ser. 119 (2008) 032030. doi:10.1088/1742-6596/119/3/032030.

- [52] R. Fruhwirth, "Application of Kalman filtering to track and vertex fitting", Nucl. Instrum. Meth. A 262 (1987) 444-450. doi:10.1016/0168-9002(87)90887-4. Cited on page 58.
- [53] CMS Collaboration, "Particle Flow Event Reconstruction in CMS and Performance for Jets, Taus, and MET", CMS Physics Analysis Summary PFT-09-001, CERN, (2009).
- [54] CMS Collaboration, "CMS public Software Guide - Description of the Particle Flow Algorithm". https://twiki.cern.ch/twiki/bin/view/CMSPublic/SWGGuideParticleFlow#Description_of_the_Algorithm. [Online, accessed 30 March 2014].
- [55] F. Beaudette, "Performance of the Particle Flow Algorithm in CMS". <http://indico.cern.ch/event/73513/session/45/contribution/825/material/slides/0.pdf>, 22.07.1010. Presentation at ICHEP - 35th International Conference on High Energy Physics, Paris. July 2010. [Online, accessed 31 March 2014].
- [56] CMS Collaboration, "CMS public Software Guide - Description of the Particle Flow Implementation in the Physics Analysis Toolkit". <https://twiki.cern.ch/twiki/bin/view/CMSPublic/SWGGuidePF2PAT>. [Online, accessed 30 March 2014].
- [57] CMS Collaboration, "Performance of CMS muon reconstruction in pp collision events at $\sqrt{s} = 7 TeV$ ", JINST 7 (2012) P10002, arXiv:1206.4071. doi:10.1088/1748-0221/7/10/P10002.
- [58] The CMS Collaboration, Particle flow event reconstruction, <https://twiki.cern.ch/twiki/bin/view/CMSPublic/WorkBookAnalysisOverview>, 2005.
- [59] The CMS Collaboration, Commissioning of the Particle-Flow Reconstruction in Minimum-Bias and Jet Events from pp Collisions at 7 TeV, PFT-10-002, 2010.
- [60] The CMS Collaboration, Muon Local Reconstruction Offline Guide, <https://twiki.cern.ch/twiki/bin/view/CMSPublic/SWGGuideMuonSystemReco>.
- [61] <https://twiki.cern.ch/twiki/bin/view/CMS/TopMUO>
- [62] S. Baffioni, C. Charlot, F. Ferri et al., "Electron reconstruction in CMS", Technical Report CMS-NOTE-2006-040, CERN, Geneva, (Feb, 2006).

- [63] W. Adam, R. Fruhwirth, A. Strandlie et al., "Reconstruction of Electrons with the Gaussian-Sum Filter in the CMS Tracker at the LHC", J. Phys. G: Nucl. Part. Phys. 31 (2005) N9. doi:10.1088/0954-3899/31/9/N01.
- [64] A. Hoecker, TMVA: Toolkit for multivariate data analysis, arXiv0703039.
- [65] CMS Collaboration, "Effective Areas for the particle-based isolation for electrons".
- [66] <https://twiki.cern.ch/twiki/bin/view/CMS/TopEGM#Electron>
- [67] M. Cacciari, G. P. Salam, and G. Soyez, "The anti- k_t jet clustering algorithm", JHEP 04 (2008) 063, arXiv:0802.1189. doi:10.1088/1126-6708/2008/04/063.
- [68] CMS Collaboration, "Jets at CMS and the determination of their energy scale". <http://cms.web.cern.ch/news/jets-cms-and-determination-their-energy-scale>. CMS public website. [Online, accessed 31 March 2014].
- [69] CMS Collaboration, "Plans for Jet Energy Corrections at CMS", CMS Physics Analysis Summary JME-07-002, CERN, 2008. Geneva, (Jul, 2008).
- [70] CMS Jet Energy Resolution and Corrections Group, "Jet Energy Corrections in CMS". <https://twiki.cern.ch/twiki/bin/viewauth/CMS/JetEnergyScale>. [CMS internal, Online, accessed 01 April 2014].
- [71] CMS Collaboration, "Jet Energy Corrections determination at 7 TeV", CMS Physics Analysis Summary JME-10-010, CERN, Geneva, (2010).
- [72] CMS Collaboration, "8 TeV Jet Energy Corrections and Uncertainties based on 19.8 fb^{-1} of data in CMS", CMS Detector Performance Note CMS-DP-2013-033, CERN, Geneva, (2013).
- [73] M. Cacciari, G. P. Salam, and G. Soyez, "The Catchment Area of Jets", JHEP 0804:005 (2007). doi:10.1088/1126-6708/2008/04/005.
- [74] M. Cacciari and G. P. Salam, "Pileup subtraction using jet areas", Phys. Lett. B 659 (2007) 119–126. doi:10.1016/j.physletb.2007.09.077.
- [75] CMS Jet Energy Resolution and Corrections Group, "Recommended Jet Energy Corrections and Uncertainties For Data and MC". <https://twiki.cern.ch/twiki/bin/viewauth/CMS/JECDataMC>. [CMS internal, Online, accessed 01 April 2014].

- [76] <https://twiki.cern.ch/twiki/bin/viewauth/CMS/TopJME>
- [77] The CMS Collaboration, *b*-tag and vertexing physics object group, <https://twiki.cern.ch/twiki/bin/viewauth/CMS/BtagPOG>, 2013.
- [78] B-jet production cross section at cdf, <http://gov.docdat.com/docs/10133/index-10479.html>.
- [79] Quantum Diaries, <http://www.quantumdiaries.org>.
- [80] The CMS Collaboration, Results on *b*-tagging identification in 8 *TeV* *pp* collisions, CMS DP -2013/005, 2013.
- [81] CMS Collaboration, "Measurement of the *b*-tagging efficiency using *t \bar{t}* events", CMS Physics Analysis Summary CMS-PAS-BTV-11-003 (2012).
- [82] The CMS Collaboration. CMS Physics Analysis Summary CMS-PAS-PFT-09-001, 2009.
- [83] C. Bernet, M. Bluj, M. Edelhoff et al., "An Introduction to PF2PAT". Slides from the PAT Tutorial on April 7, 2011 at CERN at <https://indico.cern.ch/getFile.py/access?contribId=18&resId=0&materialId=slides&confId=128291>. [online, CMS internal, accessed 2012-04-02].
- [84] The CMS Collaboration, M. C. Llatas, "New world record-first *pp* collisions at 8 *TeV*". Event visualisation from the press release, inverted colours <http://cms.web.cern.ch/news/new-world-record-first-pp-collisions-8-tev>.
- [85] The CMS Collaboration, Pile up studies, <https://twiki.cern.ch/twiki/bin/view/CMS/PileupInformation> 2013.
- [86] M. Hildreth, Pile up reweighing, <https://twiki.cern.ch/twiki/bin/viewauth/CMS/PileupJSONFileFormat> 2012.
- [87] The CMS Collaboration, Pardos and J. Kieseler, Dilepton trigger and lepton identification efficiencies for the top quark pair production cross section measurement at 8 *TeV* in the dilepton decay channel, CMS AN AN-12-389, 2012.
- [88] F. Maltoni and T. Stelzer, "MadEvent: Automatic event generation with MadGraph", JHEP 02 (2003) 027, arXiv:hep-ph/0208156.

- [89] M. L. Mangano, M. Moretti, F. Piccinini, R. Pittau, and A. D. Polosa, "ALPGEN, a generator for hard multiparton processes in hadronic collisions" ,JHEP 07 (2003) 001, arXiv:hep-ph/0206293.
- [90] S. Frixione, P. Nason, and C. Oleari, "Matching NLO QCD computations with parton shower simulations: the POWHEG method", JHEP 11 (2007) 070, arXiv:0709.2092 [hep-ph].
- [91] T. Sjostrand, S. Mrenna, and P. Skands, "PYTHIA 6.4 physics and manual", JHEP 05 (2006) 026, arXiv:hep-ph/0603175.
- [92] S. Hoche et al., "Matching parton showers and matrix elements," arXiv:hep-ph/0602031.
- [93] N. Davidson, G. Nanava, T. Przedzinski, E. Richter-Was, and Z. Was, "Universal interface of TAUOLA technical and physics documentation", arXiv:1002.0543 [hep-ph].
- [94] G. Corcella et al., "HERWIG 6.5 release note", arXiv:hep-ph/0210213.
- [95] J. Allison et al., "Geant4 developments and applications", IEEE Trans. Nucl.Sci. 53 (2006) 270.
- [96] G. Petrucciani et al., "PAT: the CMS Physics Analysis Toolkit", CR 2009-083.
- [97] CMS Collaboration, V. Khachatryan et al., "CMS Tracking Performance Results from early LHC Operation", Eur.Phys.J. C70 (2010) 1165D1192, arXiv:1007.1988 [physics.ins-det].
- [98] CMS Collaboration, S. Chatrchyan et al., "Identification and Filtering of Uncharacteristic Noise in the CMS Hadron Calorimeter", JINST 5 (2010) T03014, arXiv:0911.4881 [physics.ins-det].
- [99] M. Arthaud, M. Besancon, S. Chakrabarti, F. Deliot, E. Shabalina, and V. Sharyy, "Measurement of the $t\bar{t}$ Production Cross-section at $\sqrt{s} = 1.96 \text{ TeV}$ in Electron Muon Final States using p17 data set", *DØ-Note* 5360, March, 2007.
- [100] B. Martin, Y. Arnaud, G. Sajot, and E. Shabalina, "Measurement of the $t\bar{t}$ production cross section at $\sqrt{s} = 1.96 \text{ TeV}$ in the ee final state using p17 data set", *DØ-Note* 5386, April, 2007.

- [101] U. Bassler, J. Konrath, and C. Schwanenberger, "Measurement of the $t\bar{t}$ Production Cross-section at $\sqrt{s} = 1.96 \text{ TeV}$ in the Dimuon Final State Using p17 Data Set", *DØ-Note 5350*, February, 2007.
- [102] J. Andrea, A. Calderon, M. Cardaci et al., "Measurement of the top dilepton cross section using b-tagging at $\sqrt{s} = 7 \text{ TeV}$ with 882 pb^{-1} in pp collisions". CMS AN-11-334 [CMS internal, http://cms.cern.ch/iCMS/jsp/openfile.jsp?tp=draft&files=AN2011_334_v4.pdf].
- [103] The CMS Collaboration, S. Chatrchyan et al., "Measurement of the t t-bar production cross section and the top quark mass in the dilepton channel in pp collisions at $\sqrt{s} = 7 \text{ TeV}$ ", *JHEP* 07 (2011) 049, arXiv:1105.5661. doi:10.1007/JHEP07(2011)049.
- [104] The CMS Collaboration, "CMS Luminosity Based on Pixel Cluster Counting - Summer 2013 Update",. CMS PAS LUM-13-001 (2013).
- [105] J. Kieseler, C. Diez Pardos, "Dilepton trigger and lepton identification efficiencies for the top quark pair production cross section measurement at 8 TeV in the dilepton decay channel", CMS AN-12-389.
- [106] The CMS Collaboration, b-tag and vertexing physics object group, <https://twiki.cern.ch/twiki/bin/viewauth/CMS/BtagPOG>, 2013.
- [107] U. Heinz, Algorithm to adjust the b-tagging efficiency in simulated events, <https://twiki.cern.ch/twiki/bin/view/CMS/BTagSFUtil>, 2012.
- [108] CERN Press Office. "The first LHC protons run ends with new milestone", December 2012.
- [109] Czakon, M., Fiedler, P. and Mitov, A. The total top quark pair production cross-section at hadron colliders through $\mathcal{O}(\alpha_S^4)$. arXiv:hep-ph/1303.6254, 2013.